Durham E-Theses

The structure and electrical properties of tin oxide (Sn O(_2))

Morgan, D. F.

How to cite:

Morgan, D. F. (1966) *The structure and electrical properties of tin oxide (Sn O(_2))*, Durham theses, Durham University. Available at Durham E-Theses Online: http://etheses.dur.ac.uk/8573/

Use policy

The full-text may be used and/or reproduced, and given to third parties in any format or medium, without prior permission or charge, for personal research or study, educational, or not-for-profit purposes provided that:

- a full bibliographic reference is made to the original source
- a link is made to the metadata record in Durham E-Theses
- the full-text is not changed in any way

The full-text must not be sold in any format or medium without the formal permission of the copyright holders.

Please consult the full Durham E-Theses policy for further details.

Academic Support Office, The Palatine Centre, Durham University, Stockton Road, Durham, DH1 3LE
e-mail: e-theses.admin@durham.ac.uk Tel: +44 0191 334 6107
http://etheses.dur.ac.uk

"The Structure and Electrical Properties of Tin Oxide (SnO_2)"

by

D. F. Morgan, B.Sc. (Dunelm)

Presented in candidature for the degree of Doctor of Philosophy of the University of Durham.

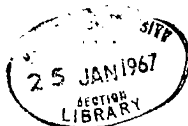

P.246

ACKNOWLEDGEMENTS

The author would like to express his thanks to:-

Professor D. A. Wright for his help and supervision, for reading the scripts, and for the use of the facilities of the Applied Physics department of Durham University.

The department workshop staff under the leadership of Mr. F. Spence and Mr. B. Blackburn for their invaluable assistance with the construction of apparatus.

Mrs. M. White of Seaford, Sussex, who typed this thesis.

All members of the Applied Physics department for their assistance, companionship and helpful discussions, especially S. F. Reddaway, M.A., who has been studying the optical properties of stannic oxide; J. Harding, M.Sc., who provided information for the indexing of the back reflection photographs; and J. Brailsford, B.Sc., and D. R. Mason, B.Sc., Ph.D. who made the preliminary measurements of electron paramagnetic resonance in SnO_2.

The University of Durham for the award of a studentship for the three years in which this work was performed.

D.F.M.

Figure 0.1

Antimony and Chromium Doped Crystals

A. Specimen 3 as cut, showing thermocouple holes.

B. Very lightly antimony doped crystal of habit 4.

C. Antimony doped crystal of habit 3.

D. Chromium doped crystal, as illustrated in figure 2.13a.

Figure 0.2

Stannic Oxide Plates

A. Undoped

B. Antimony doped

C. Chromium doped

D. Grown by hydrolysis of $SnCl_4$ (untwinned)

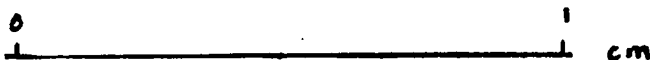

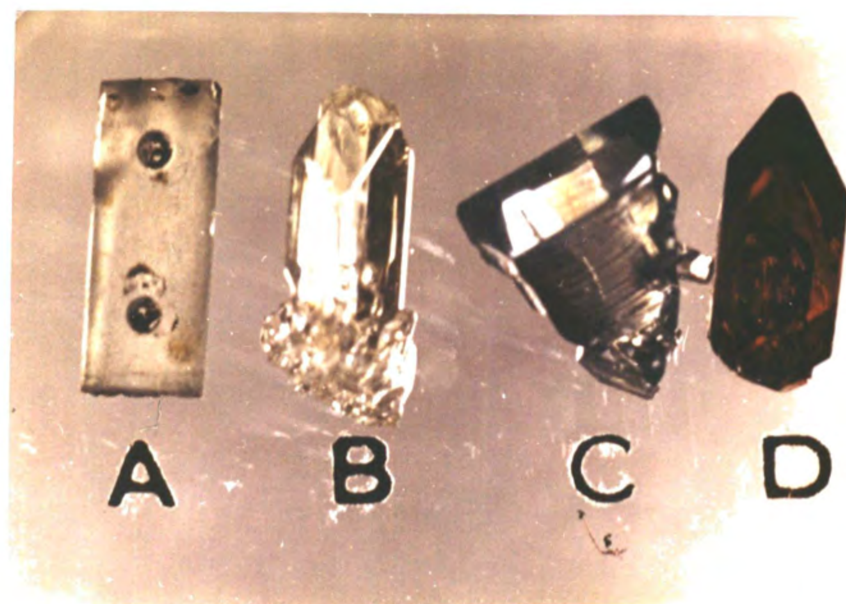
A
B
C
D

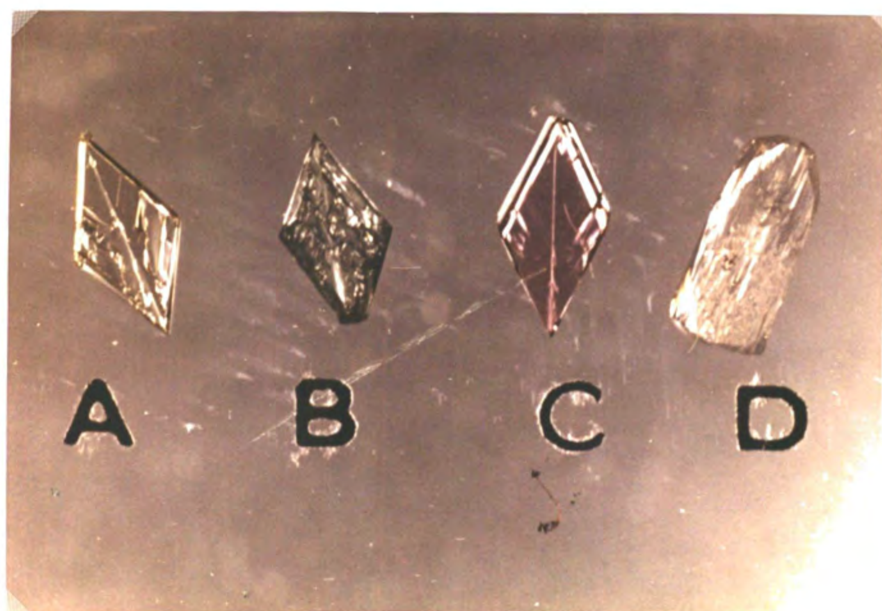
A
B
C
D

CONTENTS

	PAGE
ACKNOWLEDGEMENTS	ii
LIST OF FIGURES	ix
INTRODUCTION	xii

CHAPTER 1

THEORY

Section 1. BAND THEORY

(a) Formation of Energy Bands	1
(b) Metal Insulator or Semiconductor	1
(c) Fermi-Dirac Statistics	2
(d) Maxwell-Boltzmann Statistics	3
(e) Degeneracy	4
(f) Wave Properties of an Electron	4
(g) k-space	5
(h) Sommerfeld Model of a Metal	5
(i) Bloch Waves	6
(j) Bragg Reflection	6
(k) Brillouin Zones	7
(l) E - k Diagram	7
(m) Effective Mass	8
(n) Density of States and Inertial Effective Mass	8
(o) Holes	9
(p) Density of States	9
(q) Intrinsic Semiconductors	9
(r) Impurity Semiconductors	10
(s) Impurity Semiconductors with Compensation	12
(t) Impurity Level Spin Degeneracy	12
(u) Band Shape	13
(v) Weak Impurity Band	13
(w) Strong Impurity Band	13

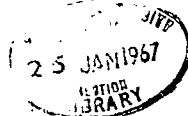

Section 2. THE BOLTZMANN EQUATION
(a) Form of the Equation 14
(b) Method of Solution 15
(c) Electrical Conductivity 16
(d) Mobility 18
(e) Electronic Thermal Conductivity 18
(f) Lattice Thermal Conductivity 19

Section 3. THERMOELECTRICITY
(a) Seebeck Effect 20
(b) Peltier Effect 21
(c) Thomson Effect 22
(d) Irreversible Effects 22
(e) Efficiency of a Thermoelectric Generator 22
(f) Figure of Merit 24

Section 4. HALL EFFECT
(a) Hall Coefficient 24
(b) Ratio of Hall Mobility to Drift Mobility 25

Section 5. ELECTRON SCATTERING MECHANISMS
(a) Introduction 27
(b) Phonons 27
(c) Acoustic Mode Lattice Scattering 28
(d) Optical Mode Lattice Scattering 29
(e) Ionised Impurity Scattering 31
(f) Neutral Impurity Scattering 33
(g) Dislocation Scattering 33
(h) Electron - Electron Scattering 33

Section 6. BONDING

(a) Introduction 34

(b) Ionic Bonding 34

(c) Covalent or Valence Bonding 34

(d) Directed Valency or Hybridisation 35

(e) Semiconducting Bond 35

(f) Nature of the Bond in Stannic Oxide 35

CHAPTER II

CRYSTAL GROWTH, HABIT AND STRUCTURE

Section 1. PHYSICAL CHEMISTRY OF THE TIN-OXYGEN SYSTEM

(a) General 37

(b) Decomposition of Stannic Oxide 38

Section 2. GROWTH FROM THE LIQUID PHASE

(a) Fluxed Melt 39

(b) Hydrothermal Synthesis 40

Section 3. GROWTH FROM THE VAPOUR PHASE

(a) Sublimation in a Closed System 41

(b) Hydrolysis of Stannic Chloride 42

(c) Vapour Phase Flame Fusion 43

(d) Helium Flow Method 43

Section 4. ARGON FLOW METHOD

(a) Growth of SnO_2 from Sn Vapour and O_2 44

(b) Effect of Different Carrier Gases 46

(c) Undoped Crystals - Quenching 46

(d) Antimony Doped Crystals 47

(e) Chromium Doped Crystals 47

(f) Indium Doping 48

(g) Gallium Doping 48

(h) Cerium Doping 48

Section 5. MASS SPECTROGRAPHIC ANALYSIS 48

Section 6. CRYSTAL HABIT
(a) Introduction 51
(b) Twinned Plates (Habit 1) 51
(c) [001] Prisms (Habit 2) 52
(d) [100] Prisms (Habit 3) 52
(e) Rods Twinned along the (001) Plane (Habit 4) 52

Section 7. CRYSTALOGRAPHIC DATA
(a) Introduction 53
(b) Powder Diffraction Photographs 53
(c) Back Reflection Laue Photographs 56
(d) Etch Pits 56

CHAPTER III

EXPERIMENTAL METHODS AND RESULTS

Section 1. INTRODUCTION 58

Section 2. ELECTRICAL CONDUCTIVITY AT HIGH TEMPERATURES
(a) Two-Probe Method 58
(b) Four-Probe Method 60
(c) Results on Undoped Crystals 62
(d) Chromium and Indium Doped Crystals 63

Section 3. SEEBECK COEFFICIENT
(a) Apparatus 63
(b) Method 64
(c) Results 65
(d) Irreproducibility of Specimen 4. 66

Section 4. HALL EFFECT

(a) Low Temperature Method 67

(b) High Temperature Method 68

(c) Variation of Mobility with Temperature 69

(d) Errors 70

Section 5. OTHER MEASUREMENTS

(a) Luminescence 71

(b) Photoconductivity 72

(c) Electron Paramagnetic Resonance 73

(d) Effect of High Fields 73

(e) Thermoelectric Probe 74

CHAPTER IV

DISCUSSION AND CONCLUSIONS

Section 1. PREVIOUS WORK ON STANNIC OXIDE

(a) Thin Films 75

(b) Polycrystalline Samples 76

(c) Natural Single Crystals 77

(d) Synthetic Single Crystals 77

(e) Summary of Mobility Measurements 78

Section 2. VARIATION OF MOBILITY WITH TEMPERATURE

(a) Above 300°K 78

(b) Below 300°K 81

(c) Brief Discussion of the Results of Marley and Dockerty 82

(d) Brief Discussion of the Results of Nagasawa, Shionoya and Makishima 82

Section 3. EFFECTIVE MASSES OF ELECTRONS AND HOLES

(a) Electron Effective Mass 83
(b) Conclusions 86
(c) Band Gap 87
(d) Hole Effective Mass 88
(e) Impurity Levels 89

Section 4. THERMOELECTRIC FIGURE OF MERIT

(a) $\alpha^2\sigma$ Product 90
(b) Thermal Conductivity (K) 90
(c) Figure of Merit $Z = \frac{\alpha^2\sigma}{K}$ 91
(d) Conclusions 91

Section 5. SUMMARY AND SUGGESTIONS FOR FURTHER WORK 91

References. 94

Appendix Reprint from British Journal of Applied Physics 99

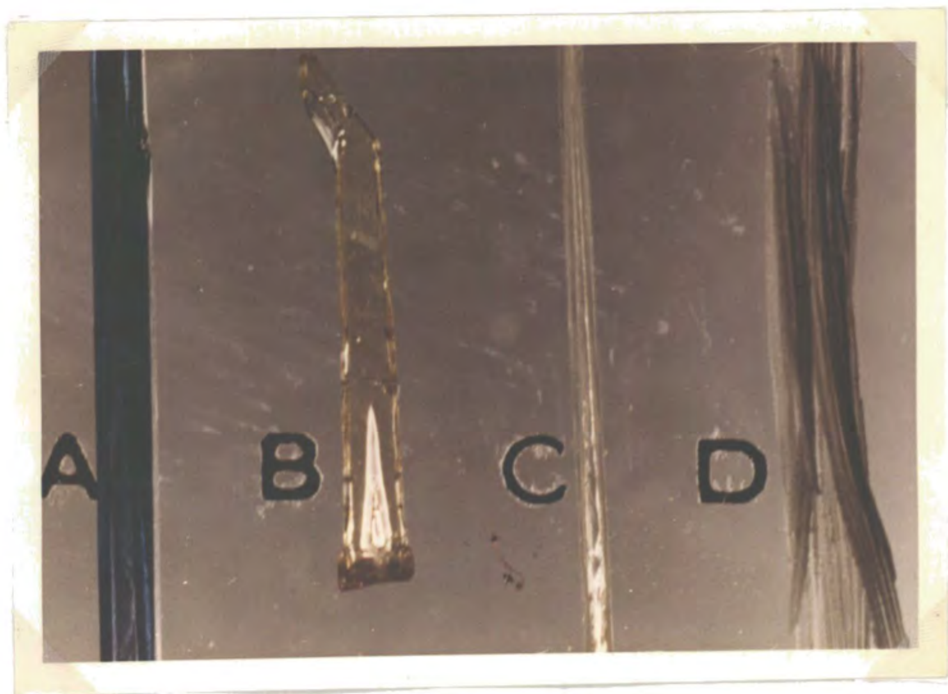

Figure 0.3

Doped and undoped rods

A. Highly antimony doped rod

B. Brown undoped rod

C. Colourless undoped rod

D. Whiskers from flame fusion growth

Scale as for figures 0.1 and 0.2

F I G U R E S

Introduction

0.1 Antimony and Chromium Doped Crystals

0.2 Stannic Oxide Plates

0.3 Doped and Undoped Rods

Chapter I

1.1 The Broadening of the Energy Levels of Sodium with atomic separation

1.2 Potential Well Model of a Free Electron Gas

1.3 E-k diagrams for (a) Sommerfeld waves and (b) Bloch waves

1.4 Band diagram for (a) an intrinsic semiconductor and (b) an impurity semiconductor

1.5 Variation of the Density at States with energy bad (a) a weak impurity metal and (b) a strong impurity metal

1.6 A simple thermoelectric circuit

1.7 Diagrammatic Thermoelement

1.8 Hall Effect in a Rectangular Bar

1.9 Frequency Spectrum of Phonons in a Polar solid containing two atoms per unit cell.

1.10 Electron sharing schemes for the covalent bond in Stannic Oxide for co-ordination numbers of (a) four and (b) six

Chapter II

2.1 Tin-oxygen system Phase Diagram

2.2 Vapour Pressure of Tin and its Oxides

2.3a Furnace arrangement for Argon Flow method of growing Stannic Oxide

b Temperature Profile of the Furnace

2.4a Transmission Spectra of Antimony Doped and Undoped SnO_2 Plates and

b Chromium Doped Plates

2.5 Position of growth of the Chief Crystal Habits

2.6 Various Crystal Habits

2.7 Habit 1 showing

a (301) Twinned Plate
b Trapezoidal Plate

2.8 Arrangement of Atoms along (301) Twin Plane

2.9a Typical c-axis rods

b C-axis rods shown End Voids

2.10 Habit 2

a c-axis rod showing End Faces

b c-axis rod showing Different End Faces

c Rhombohedral Crystal

2.11 Uncut Crystal used for Specimen 3

a Plan

b End View

2.12 Habit 3

a Rod Form

b Plate Form

2.13 (011) Twinned Crystals, Habit 4

a One Form

b Another Form

2.14 Arrangement of Atoms along (011) Twin Plane

215a Rutile Structure Unit Cell

b Arrangement at Atoms in $Sn O_2$ Crystal showing Two equivalent Tin Sites.

2.16 Powder Diffraction Photograph of $Sn O_2$

2.17 a and b Nelson-Riley Plots of Measurements taken from Powder Diffraction Photographs

2.18 Back Reflection Photographs in
a [001] Direction
b [100] Direction

2.19 Etch Pits on (110) Face of c-axis Crystal

2.20 Etch Pits on a-axis Crystal on
a (011) Face and
b (110) Face

Chapter III

3.1 High Temperature Four Probe Conductivity Measurements

a Photograph of Holder

b Circuit Diagram

3.2 Temperature Variation of Resistivity of Colourless Undoped Crystals

3.3 Temperature Variation of Resistivity of Brown Undoped Crystals

3.4 Seebeck Coefficient Apparatus

3.5 Seebeck Measuring Circuit

3.6 Hall Effect

a Specimen Holder

b Circuit

3.7 Temperature Variation of Seebeck Coefficient of Antimony Doped Crystals

3.8 Temperature Variation of Electrical Conductivity of Antimony Doped Crystals

3.9 Temperature Variation of Mobility of Antimony Doped Crystals

3.10 Spectral Distribution of Luminescence of Flame Fusion Whiskers of $Sn\ O_2$

3.11 Typical High Field Conductivity

3.12 Circuit for Thermoelectric Probe

Chapter IV

4.1 Temperature Variation of Mobility of $Sn\ O_2$ as Measured by Various Workers

4.2 Temperature Variation of Mobility of $Sn\ O_2$ Crystals as Measured by Marley and Dockerty

4.3 Low Temperature Coefficient of Mobility

4.4 Variation of Band Gap with Temperature, according to Summitt and Bornelli

4.5 Temperature Variation of

a $\alpha^2\sigma$ Product

b Thermal Conductivity (calculated)

c Figure of Merit (Z.).

I N T R O D U C T I O N

The primary purpose of studying stannic oxide was to assess its possibilities as a high temperature thermoelectric material. Stannic oxide is chemically stable at high temperatures (full details are reported in Chapter 2) and measurements on the thermal conductivity of ceramics indicate that this property is in the same order as other thermoelectric materials. A review of the literature that was available at the beginning of this work, and that which has since appeared, is made in Chapter 4. Although there had been many papers published on thin films, the only reports on the bulk material were of compressed powder samples and of natural crystals. The results of the former were complicated by possible grain boundary effects and those of the latter by the relatively high impurity concentrations in the crystals. In order to obtain as much information on stannic oxide, it was decided that single crystals should be grown. This was the initial problem of the research. Since the main interest was in thermoelectric applications, highly doped n- and p-type crystals were required. The measure of success in this field is reported in Chapter 2.

The second major problem was the measurement of the properties of the crystals at high temperatures. The methods used and the results obtained are reported in Chapter 3.

The first chapter of this thesis attempts to summarise the elements of band theory on which the conclusions of Chapter 4 are based. It tries to show the derivation of the equations used and to outline the theories and assumptions on which the final conclusions are based. This chapter also includes a short discussion on the nature of the chemical bond between the tin and oxygen atoms or ions in the stannic oxide crystal in relation to its semi-conducting properties.

CHAPTER 1:

Section 1: Band Theory

1a. Formation of Energy Bands

In an isolated atom, the energy levels of each electron orbital have discrete values. If, however, atoms are brought into very close proximity, as in a crystal lattice, the wave functions - which describe the probability of finding an electron in time and space in a particular orbital - of electrons in adjacent atoms can overlap. If this overlap is very strong, the levels broaden out into bands which cover a range of energies. Figure 1.1 shows the calculated broadening of the energy levels in sodium against the interatomic distance (r).

1b. Metal, Insulator or Semiconductor

If the constituent atoms of a lattice contribute the exact number of electrons needed to fill a set of energy states, i.e., to completely fill a band, there can be no current flow in this band. This situation can only occur at absolute zero temperature. At temperatures greater than $0^{o}K$, there will be a finite probability of electrons being excited thermally from this filled band to a higher empty band. This enables two types of conduction to occur. The few electrons in the unfilled band, known as the conduction band, are

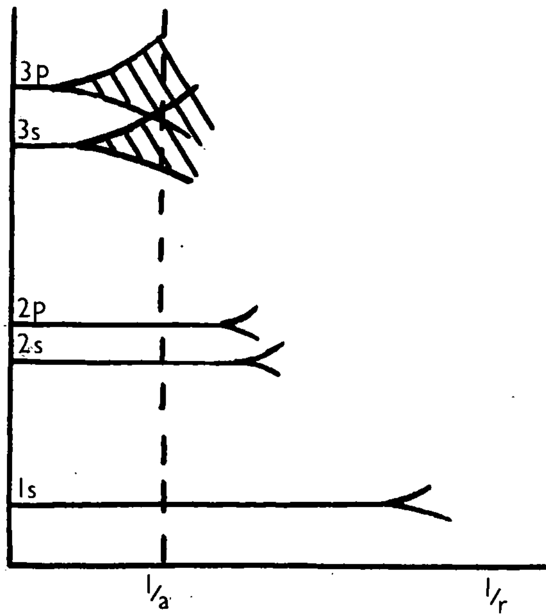

Figure 1.1: The broadening of the energy levels of sodium with change in atomic separation 'r'. 'a' is the actual separation of the atoms in metallic sodium.

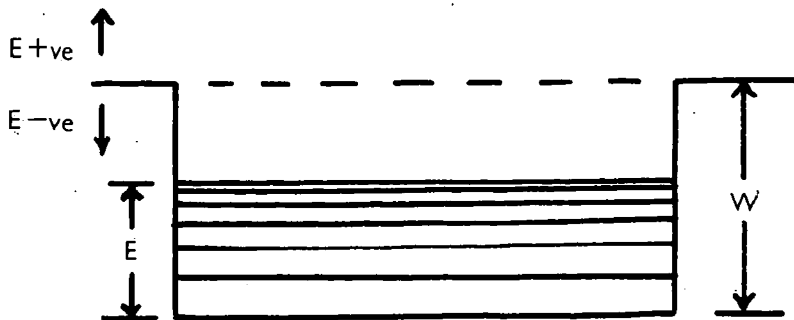

Figure 1.2: The potential well model of a free electron gas.

free to move in a field: and so are the holes, or absence of electrons, in the almost filled band, known as the valence band. The only difference between an insulator and a semiconductor, at a particular temperature, is the width of the forbidden gap between the two bands. The number of electrons in the conduction band, which in an intrinsic semiconductor equals the number of holes in the valence band, at a given temperature is inversely proportional to the exponential of half the width of the forbidden gap (see equation 1.20), which may itself vary with temperature.

If the crystal bonding were completely ionic (see sect.6) there would be no overlap of wave functions and no bands would be formed. In this case charge transport can only occur by the migration of ions, which will have a very low mobility. Ionic crystals are usually very good insulators.

If the atoms in a lattice only contribute enough electrons to half fill the energy states available in the band, then electrons will be free to move under the influence of an applied field even at absolute zero temperature. This can also occur if the conduction band in one direction in the crystal overlaps the valence band in another. This type of material is a metal.

1c. Fermi-Dirac Statistics

This type of statistics is based on the Pauli exclusion principle, which states that no more than two electrons, each of opposite spin, can occupy any one

energy level and on the principle that each electron is indistinguishable from another. An important result obtained from these statistics is that the probability $f(E)$ of a state of energy (E) being occupied at a particular temperature (T) is given by

$$f(E) = \left[\exp \frac{E-E_f}{kT} + 1\right]^{-1} \qquad (1.1)$$

where k is known as Boltzmann's constant and E_f is defined as the Fermi energy and is the particular value of the energy state in which the probability of occupation is ½.

In calculating expressions for the various properties of semiconductors, it is often necessary to evaluate integrals of the form

$$F_x(\eta_f) = \int_0^\infty \frac{\eta^x}{\exp(\eta-\eta_f)+1}\, d\eta \qquad (1.2)$$

where $\eta = \frac{E}{kT}$ and $\eta_f = \frac{E_f}{kT}$.

This function is known as the Fermi Dirac integral and its values for integral and half integral values of x are tabulated in references (1 - 5).

1d. Maxwell-Boltzmann Statistics

If each electron may be considered independent and there is no restriction on the number of electrons that may occupy a given energy level, classical statistics give the result that the probability ($f(E)$) of a particle having an energy E at temperature (T) is

$$f(E) = A \exp\left(-\frac{E}{kT}\right) \qquad (1.3)$$

where A is a constant.

The Fermi-Dirac distribution function approximates to the Maxwell-Boltzmann function when $E - E_F \gg kT$. It is much more convenient to use Maxwell-Boltzmann statistics when considering non-degenerate semiconductors.

1e. Degeneracy

If there are only a few electrons in the conduction band compared with the number of states available, the energy distribution of these electrons will not be significantly affected by the exclusion principle. In this condition the semiconductor is said to be non-degenerate and Maxwell-Boltzmann statistics may be used to simplify calculations. A useful criterion is that non-degenerate statistics may be applied if the reduced Fermi level (η_F) is less than - 1, as measured from the bottom of the conduction band.

If $\eta_F > 2$, the conditions near the bottom of the conduction band are similar to those in a metal. The lower energy levels are all filled according to the exclusion principle. Since most of the free electrons occur in a narrow band of energy in the region of the Fermi level, for most calculations they may all be considered to have the same energy, the Fermi energy (E_F).

For the intermediate region ($-1 < \eta_F < 2$) the full Fermi Dirac statistics must be used for calculations.

1f. Wave Properties of an Electron

The direct evidence of electron diffraction has shown that a beam of electrons of momentum ($\underset{\sim}{p}$) can be treated as a wave train of wavelength λ given by

$$\lambda = \frac{h}{\underset{\sim}{p}} \tag{1.4}$$

N.B. Equation 1.5 is strictly the time - independent Schrödinger equation. To obtain the more general time-dependent equation, the spacially defined Schrödinger ψ-function must be expanded into a space-time function (u), where

$$u = \psi \exp \frac{i \varepsilon t}{\hbar}$$

The wave equation may now be written

$$\nabla^2 u + \frac{2m}{\hbar^2}\left(\frac{\hbar}{i}\frac{\partial u}{\partial t} - Wu\right) = 0$$

where h is known as Planck's constant.

In general, the motion of electrons can be calculated by determining the appropriate wave equation, the form of which was proposed by Schrödinger,

$$\nabla^2\psi + \frac{2m}{\hbar^2}(\varepsilon - W)\psi = 0 \quad , \qquad (1.5)$$

where ψ is the appropriate wave function, ε the kinetic and W the potential energy, and $\hbar = \frac{h}{2\pi}$.

1g. k - Space

Quantum theory states that energy is not continuous, but is quantised: that is, only discrete values of energy, and thus momentum ($\underline{p}$) are permissible. The permitted values of $\underline{p}$ are given by the relation :

$$\underline{p} = \hbar \underline{k} \, , \qquad (1.6)$$

$$\text{where } k = \frac{2\pi n_x}{L} \quad n_x = 0, \pm 1, \pm 2 \text{ . etc.}$$

and L is the periodic length of the wave function parallel to one of the crystal axes.

The wave vector ($\underline{k}$) gives the direction of propagation of plane waves ($\psi = C \exp(i\, \underline{k}.\underline{r})$, where C is a constant).

1h. Sommerfeld Model of a Metal

The Sommerfeld, or free electron gas , model of electrons in a metal is considered as it was a first step towards explaining the behaviour of carriers in a solid. In this model, the electrons are considered in a potential well, the boundaries of which are the boundaries of the metal. The number of carriers is about the same as the number of atoms ($\sim 10^{23}$ cm^{-3}). Each electron has the same potential energy W and a kinetic energy ε as well (see figure 1.2).

1i. Bloch Waves

Bloch first considered the motion of an electron through a periodic lattice in 1928. He assumed a periodic potential that varied identically in each unit cell of the crystal. Thus if a translation vector is defined as

$$R_m = m_1\underline{a}_1 + m_2\underline{a}_2 + m_3\underline{a}_3 \qquad (1.7)$$

(where $\underline{a}_1, \underline{a}_2, \underline{a}_3$ are the three primitive vectors defining the edges of the crystal unit cell and m_1, m_2, m_3, are integers)

then Bloch showed that in order to satisfy the conditions of the periodicity, the solutions of the Schrödinger equation must be of the form:

$$\psi_k = U_k(r) \exp(i\, \underline{k}.\underline{r}) \qquad , \qquad (1.8)$$

where $U_k(r + R_m) = U_k(r)$: in general $U_k(r)$ will be different for each value of E.

Waves of this form will proceed unhindered through a perfect lattice.

1j. Bragg Reflection

The Bragg reflection law for a beam of wavelength λ striking a crystal, with a spacing of distance 'd' between planes of atoms, at an angle θ with the planes is

$$n\lambda = 2d \sin\theta \qquad (1.9)$$

If this law is applied to a wave packet of electrons propagating through a lattice, a wave with a value of $k = \frac{\pi n}{a}$ (where n is an integer) along one of the crystal axes, in which direction the lattice spacing is 'a', will not pass through, but will be reflected. This means that the energy that such an electron wave packet may have in a real crystal is not continuous but has allowed and forbidden values.

1k. Brillouin Zones

The k values for which Bragg reflection occurs are said to lie on the Brillouin zone boundaries in k space. So the crystal lattice determines the zone shapes. The zone boundaries correspond to discontinuities in the E - k curve.

Due to Bragg reflection, when only one dimension is considered there must always be a gap of forbidden energy between each allowed band. But since the value of the k at which Bragg reflection occurs differs for different directions in the crystal, it is possible for an allowed band in one direction to overlap a lower allowed band in another direction. When this occurs there is, in effect, no forbidden energy and the material will have metallic properties.

1l. E - k Diagrams

Figure 1.3(a) shows the parabolic shape of the E-k diagram for an electron on the Sommerfeld model. The total energy is given by

$$E = \mathcal{E} - W = \frac{p^2}{2m} - W = \frac{\hbar^2 k^2}{2m} - W \qquad (1.10)$$

Differentiating this expression with respect to k

$$\frac{\partial E}{\partial k} = \frac{\hbar^2 k}{m} = \frac{\hbar p}{m} = \hbar v \qquad (1.11)$$

Thus the electron velocity v is given by

$$v = \frac{1}{\hbar} \frac{\partial E}{\partial k} \qquad (1.12)$$

Also from equation (1.11) the electron mass is given by

$$m = \hbar^2 k \left(\frac{\partial E}{\partial k} \right)^{-1} \qquad (1.13)$$

If the value of m is constant, another expression for m, obtained by the second differential of equation (1.10)is

$$m = \hbar^2 \left(\frac{\partial^2 E}{\partial k^2} \right)^{-1} \qquad (1.14)$$

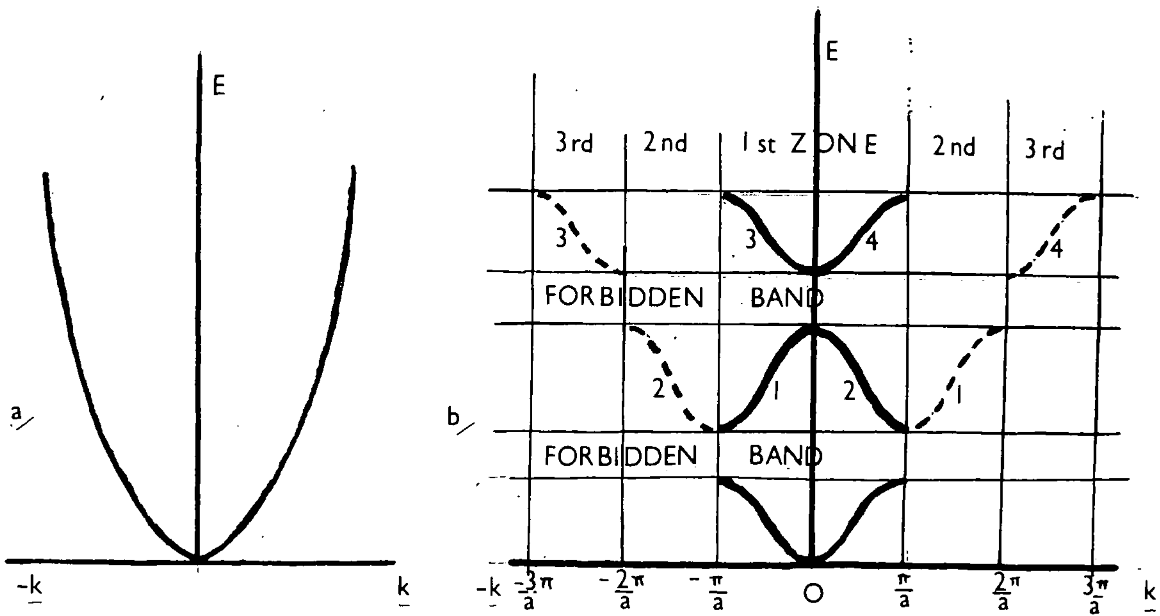

Figure 1.3: E-k curves in one direction for (a) Sommerfeld waves and (b) Bloch waves.

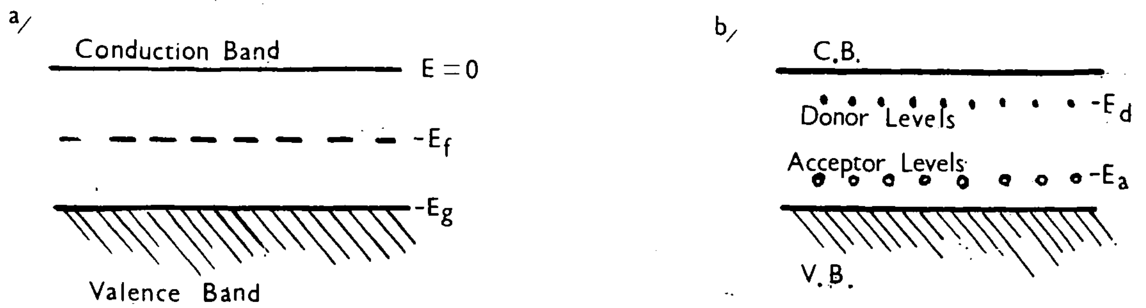

Figure 1.4: Band picture for (a) an intrinsic and (b) an impurity semiconductor.

On the Bloch theory E - k diagrams such as figure 1.3(b) are obtained. The gradient of the E - k curve ($\frac{\partial E}{\partial k}$) is always zero at the zone boundaries.

1m. Effective Mass

From figure 1.3(b), it can be seen that $\frac{\partial^2 E}{\partial k^2}$ is not constant, consequently for the Bloch theory we must replace the free space electron mass by an effective mass m^*, defined by the relationship

$$m^* = \hbar^2 k \left(\frac{\partial E}{\partial k} \right)^{-1} \qquad (1.15)$$

The effective mass may simply be regarded as the value of mass required to fit the Newtonian equations of motion that takes into account the effect of crystalline field.

1n. Density of States and Inertial Effective Mass

In real substances the energy surfaces are usually complicated and depend on the direction in the crystal lattice, and the effective mass should be considered as a tensor quantity.

Different properties involve the energy momentum curvatures in different ways and thus a different expression for the effective mass is required for expressions for mobility, density of states and high frequency dielectric constant. The two most commonly encountered are the 'Density of States' effective mass and the 'Inertial' effective mass.

The density of states effective mass is that obtained when the number of carriers in a band is related to the position of the Fermi level, and so is the value obtained when the Hall and Seebeck effect are compared.

The inertial effective mass is the quantity involved in the high frequency dielectric constant and is also the value obtained from cyclotron resonance experiments.

1o. Holes

From the variation of the gradient of the E - k curve in figure 1.3(b) it can be seen that the value of $\frac{\partial^2 E}{\partial k^2}$ becomes negative in the upper half of the allowed bands. Although it is mathematically correct to consider the electrons near the top of the band to have a negative effective mass, it is difficult to deduce the consequences. It is more convenient to introduce the concept of a hole, which in effect is the absence of an electron, that behaves as a positively charged carrier.

1p. Density of States

The quantum calculation of the density of states per unit volume in a solid gives the result that the number of states g(E), each of which may be occupied by two electrons, that exist between the energies E and $E + dE$ is given by the equation

$$g(E) = \frac{1}{4\pi^2} \left(\frac{2m^*}{\hbar^2}\right) E^{\frac{1}{2}} \qquad (1.16)$$

1q. Intrinsic Semiconductor

Figure 1.4(a) shows the simple band picture often used to represent an intrinsic semiconductor with a forbidden band gap of E_g. It is conventional to measure all energies relative to the bottom of the conduction band.

The total number of carriers in each band is given by the integral over all energies of the product of the number of states available and their probability of occupation. Thus

$$n_e = 2\int_0^{\infty} g(E)\, f(E)\, dE \quad \text{and} \quad n_h = 2\int_{-E_g}^{-\infty} g(E)\,[1 - f(E)]\,dE \qquad (1.17)$$

The actual width of the bands is unknown, but as the majority of the free carriers are close to the band edges, it is a valid approximation to perform the integrations between plus or minus infinity and the relevant band edge. The result of the integration, using Fermi-Dirac statistics for f(E), gives the result

$$n_e = N_c F_{\frac{1}{2}}(\eta_F) \quad \text{and} \quad n_h = N_v F_{\frac{1}{2}}\left(-\frac{E_F - E_g}{kT}\right) \quad (1.18)$$

where $N_c = \frac{1}{2\pi^2}\left(\frac{2m_e^* kT}{\hbar^2}\right)^{3/2}$ and

$$N_v = \frac{1}{2\pi^2}\left(\frac{2m_h^* kT}{\hbar^2}\right)^{3/2} \quad (1.19)$$

are known as the effective densities of states of the conduction and valence bands respectively.

For a non-degenerate semiconductor, Maxwell-Boltzmann statistics may be used. These give the simple result that

$$n_e = \frac{\pi^{1/2}}{2} N_c \exp \eta_F \quad \text{and} \quad n_h = \frac{\pi^{1/2}}{2} N_v \exp\left(-\frac{E_F - E_g}{kT}\right) \quad (1.20)$$

In an intrinsic semiconductor $n_e = n_h$, so the two expressions of 1.20 may be equated to obtain an expression for the Fermi energy E_F.

$$E_F = -\frac{E_g}{2} + \frac{3kT}{4} \log_e\left(\frac{m_h^*}{m_e^*}\right) \quad (1.21)$$

It may be seen that the product $n_e n_h$ is constant for a material at a given temperature, even if the semiconductor is extrinsic.

$$n_e n_h = N_c N_v \exp\left(-\frac{E_g}{kT}\right) \quad (1.22)$$

1r. Impurity Semiconductors

If an atom with one more valence electron than is necessary for bonding is incorporated into the lattice of a semiconductor, the extra electron will be only weakly bound and thus easily excited into the conduction band. This type of impurity is known as a donor. The donor states usually form an energy level slightly below

the conduction band. (see figure 1.4b).

Similarly, if an atom with one fewer valence electron than is necessary for bonding is incprporated in the lattice, an energy state will be formed just above the valence band, into which electrons from the valence band may easily be excited, leaving behind free holes. This type of impurity is known as an acceptor.

If only donor impurities are present, at low temperatures, the number of carriers in the conduction band will be given by

$$n_e = (\beta N_D N_c)^{1/2} \exp\left(-\frac{E_D}{2kT}\right) , \qquad (1.23)$$

where N_D is the density of donors and β the spin degeneracy (see sect. 1t) and the Fermi energy by

$$E_F = -\frac{E_D}{2} + \frac{1}{2} kT \ln\left(\frac{\beta N_D}{N_c}\right) . \qquad (1.24)$$

At higher temperatures the donor levels will become virtually completely ionised and the number of carriers may be considered constant and equal to the donor density (N_D). This region is known as the exhaustion region and the Fermi level in this region is given by

$$E_F = kT \ln\left(\frac{N_D}{N_c}\right) . \qquad (1.25)$$

In these regions where the properties of the semiconductor are dominated by the impurities, it is known as extrinsic. At high temperatures, the intrinsic properties of the material will become predominant.

When the properties of the material are dominated by the electron behaviour, which is usual when donor impurities are present, it is known as n-type. If the behaviour of the holes is dominant, it is known as

p-type. For p-type material, equations 1.23, 1.24, 1.25 hold if N_D is replaced by N_A, E_F by $-E_g-E_F$ and E_D by E_A

1s. Impurity Semiconductors with Compensation

If acceptors are present, as well as donor, in an n-type semiconductor the relations 1.23 and 1.24 will be altered. If the density of acceptors (N_A) becomes larger than the carrier density, then the Fermi level will be given by

$$E_F = -E_D + kT \ln \left[\frac{\beta (N_D - N_A)}{N_{C}} \right] . \quad (1.26)$$

So at temperatures lower than the exhaustion temperature, the Fermi level may be approximately equal to $-E_D$ or $-\frac{E_D}{2}$ depending on the degree of compensation.

1t. Impurity Level Spin Degeneracy

Landsberg (6) and Guggenheim (7) realised that each impurity atom will usually offer more than one state. The simplest example is a donor whose outermost electron is of purely s-orbital character. Since this is an unpaired electron it can be trapped in two ways, either spin up or spin down. Accordingly its probability of being occupied is given by the equation

$$N_{D\,occ} = \frac{N_D}{1 + \beta \exp \left[\frac{E_D - E_F}{kT} \right]} , \quad (1.27)$$

where $\beta = \frac{1}{2}$.

If the impurity atom is an acceptor which requires one electron to complete a set of paired bonds, then this electron must have the opposite spin to the one electron already in the outer orbital. In this case $\beta = 2$, i.e., the absence of an electron may be described in two ways.

1u. Band Shape

Section I1 showed that on the Sommerfeld model the shape of the E-k diagram was parabolic. On the Bloch models this parabolic shape is not maintained. However, if the band is broad (i.e., the number of energy states is large) and only states near the bottom or top of the band are considered, the band may be considered parabolic, i.e., the effective mass may be assumed to be a constant. However, this need not necessarily be so. More elaborate band structures are found in practice. The most important of these is the many-valley type of structure, in which the conduction band has a number of equivalent minima situated at points in k-space which are related to the crystal structure.

1v. Weak Impurity Band Conduction

If there are either donors and/or acceptors present as impurities in a crystal, at very low temperatures (not greater than a few degrees Kelvin) there could exist a situation where all the available electron supply is in the impurity band. Since the wave functions of the impurity atoms decay exponentially with distance, the mobility of electrons in the band will be strongly dependent on the density of the impurity atoms.

1w. Strong Impurity Band Conduction

If the impurity density is very large ($> 10^{20}\ cm^{-3}$) the overlap between the wave functions of the impurity atoms may be so strong that the impurity band must cover an appreciable range of energy. The centre of gravity of this distribution may occur within the conduction band. The presence of this impurity band would have a pronounced effect on the lower energy states of the conduction band,

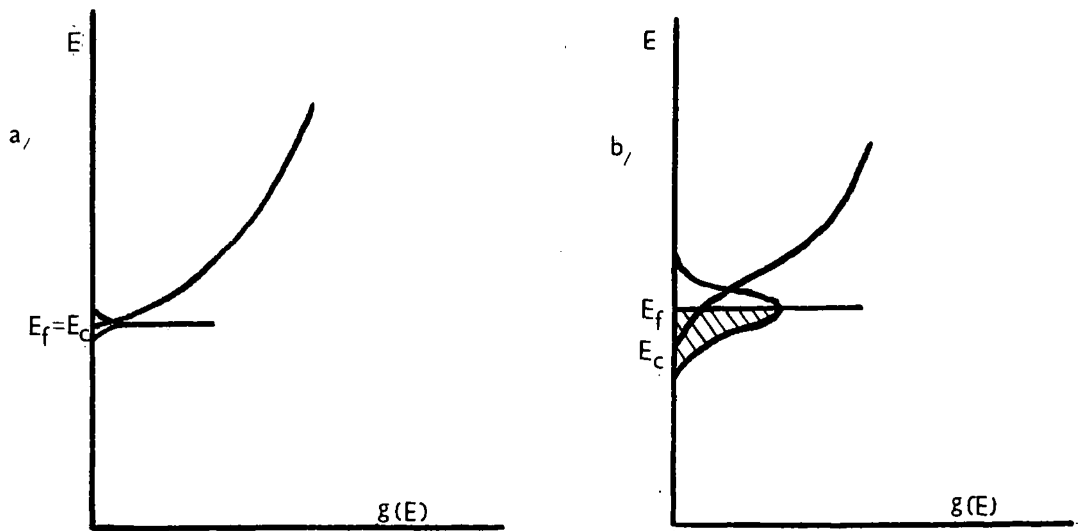

Figure 1.5: Variation of the density of states with energy for (a) a weak and (b) a strong impurity metal.

making the band non-parabolic. The effect of an impurity band on the density of states is shown in figure 1.5.

Section 2. The Boltzmann Equation

2a. Form of Equation

An electron system can be described by a distribution function f $(\underline{k},\underline{r})$ which is defined in such a way that the number of electrons in a volume element $d\underline{r}$ with a wave vector $\underline{k}$ in an element $d\underline{k}$ is

$$\frac{1}{4\pi^3} \quad f\,(\underline{k},\underline{r},t)\,d\underline{k}\;d\underline{r}\;dt \qquad (1.28)$$

Once the behaviour of this function $f(\underline{k},\underline{r},t)$ is known under conditions of electric and magnetic fields, it is possible to predict the various electronic properties of the material. The problem is to determine this function under steady state conditions. In the absence of external fields and thermal gradients, f $(\underline{k},\underline{r},t)$ becomes the Fermi-Dirac distribution function. If the perturbing fields are small, the condition that the solution represents a steady state situation is that

$$\frac{df}{dt} = 0 \qquad (1.29)$$

Two factors contribute to the variation of the distribution function with time, these are :-

(i) The acceleration of charge carriers by electric and magnetic fields, and the diffusion of charge carriers along temperature gradients or concentration gradients due to non-uniformities in composition

(ii) The collisions of electrons with imperfections in the lattice.

Equation 1.29 may be written

$$\left(\frac{\partial f}{\partial t}\right)_D + \left(\frac{\partial f}{\partial t}\right)_C = 0 \quad . \qquad (1.30)$$

The first term is the drift term, the second is the collision term. When the drift term is expressed in terms of the influence of potential and spatial gradients, the Boltzmann equation obtained is

$$e\left(\underline{\mathcal{E}} + \frac{1}{c}\,\underline{v} \wedge \underline{H}\right) \cdot \frac{1}{\hbar} \nabla_k f(\underline{k},\underline{r}) + \underline{v} \cdot \nabla_r f(\underline{k},\underline{r}) = \left(\frac{\partial f}{\partial t}\right)_C, \qquad (1.31)$$

where ∇_k and ∇_r are operators in k-space and co-ordinate space respectively, $\underline{\mathcal{E}}$ is the electric and H the magnetic field and c the velocity of light, that must be introduced if c.g.s. units are used.

2b. Method of Solution

It is not possible to obtain a complete solution to the full equation. The problem can be simplified if the collision integral can be expressed in terms of a relaxation time $\tau(\underline{k})$, where $\tau(\underline{k})$ is of the form

$$\tau(\underline{k}) = M(T)\, E^{s}(\underline{k}), \qquad (1.32)$$

where M(T) is a function of temperature only, and s is a constant, known as the scattering parameter, the value of which depends on the type of scattering.

Then if $f(\underline{k},\underline{r},t)$ is the distribution function at an instant of time, the approach to equilibrium arising from collisions is

$$\left(\frac{\partial f}{\partial t}\right)_c = -\left(\frac{f - f_o}{\tau}\right) . \qquad (1.33)$$

The general procedure for determining the distribution function is to expand f $(\underline{k},\underline{r},t)$ about the equilibrium distribution f_o $(\underline{k})$.

$$f(\underline{k},\underline{r}) = f_o(\underline{k}) - \underline{v} \cdot \underline{\Phi}(\underline{k},\underline{r}) \frac{\partial f_o}{\partial E} , \qquad (1.34)$$

where $\Phi(\underline{k},\underline{r})$ is expressed as a series of powers of the applied fields.

When no magnetic forces act on the electrons, combining equations 1.31, 1.33 and 1.34 gives

$$\frac{e}{\hbar}\,\underline{\mathcal{E}}.\nabla_k f + \underline{v}.\nabla_r f = -\frac{f-f_o}{\tau} = \frac{\underline{v}.\,\underline{\Phi}(\underline{k},\underline{r},)}{\tau}\left(\frac{\partial f_o}{\partial E}\right) \quad (1.35)$$

If the relationship

$$\nabla_r f_o = \frac{\partial f_o}{\partial T}\nabla_r T = \frac{\partial f_o}{\partial E}\left[T\nabla_r\left(\frac{E_F}{T}\right) + \left(\frac{E}{T}\right)\nabla_r T\right] \quad (1.36)$$

is used with equations 1.34 and 1.35, the following expression can be obtained:

$$\tau\left[e\underline{\mathcal{E}} - T\,\nabla_r\left(\frac{E_F}{T}\right) - \left(\frac{E}{T}\right)\nabla_r T\right] = \underline{\Phi}(\underline{k},\underline{r}) \quad (1.37)$$

From this formal solution it is possible to derive appropriate expressions for the electrical and thermal conductivities and for the thermo-electric effects.

2c. Electrical Conductivity

Under isothermal conditions the current density(J) in a conductor is the product of the velocity ($\underline{v}$) and charge of each carrier integrated over all the carriers.

i.e.,

$$J = \frac{e}{4\pi^3}\int \underline{v}\; f\; d\underline{k} = \frac{e}{4\pi^3}\int \tau\underline{v}.(\underline{v}.\underline{E})\left(\frac{\partial f_o}{\partial E}\right)d\underline{k} \quad (1.38)$$

The conductivity tensor ($\underline{\sigma}$) is defined by

$$\underline{J} = \underline{\sigma}\,\underline{E} \quad (1.39)$$

so

$$\sigma = -\frac{e^2}{4\pi^3}\int(\underline{v}\,\underline{v})\;\tau\left(\frac{\partial f_o}{\partial E}\right)d\underline{k} \quad (1.40)$$

It is convenient to express this integration over k-space as the combination of an integration over surfaces of constant energy, and an integration over energy

i.e.,

$$d\underline{k} = 8\pi^3\rho\, dS\, dE \quad (1.41)$$

where $\rho = (8\pi^3 \nabla_k E)^{-1}$

(the surface density of states in k-space).

So expression 1.40 for the conductivity tensor becomes

$$\sigma = -2e^2 \int \tau(k) \; (\underline{vv})\rho \, d\,S \int \left(\frac{\partial f_0}{\partial E}\right) d\,E \qquad (1.42)$$

If the electron gas is highly degenerate, this may be written as

$$\sigma = 2e^2 \int' \tau(k) \; (\underline{v}\;\underline{v})\rho \, dS \qquad (1.43)$$

where $\int'$ denotes an integration over the constant energy surface in k-space corresponding to the Fermi energy E_F.

In the special case of a spherical energy surface and an isotropic relaxation time, the conductivity tensor is a multiple of the unit tensor. The diagonal components are

$$\sigma = 2e^2 \; \tau\,(E_F)\,\left(\frac{v^2}{3}\right) N\,(E_F)\,. \qquad (1.44)$$

It can be shown that

$$E_F = \frac{\pi^2 \hbar^2}{2m^*} \left(\frac{3n}{\pi}\right)^{2/3} \qquad (1.45)$$

If this expression is used, together with equation 1.16 and the relationship $v = \frac{2E_F}{m^*}$, the following well-known result is obtained:

$$\sigma = \frac{n\,e^2\,\tau(E_F)}{m^*} \qquad (1.46)$$

The modification of this result for a semiconductor is discussed in section 4.

From equations 1.34, 1.37 and 1.38 an expression for the current flow may be obtained.

$$J = K_1 \left[e^2 \underline{E} - e \; T \nabla_r \left(\frac{E_F}{T}\right)\right] - K_2\left[\left(\frac{e}{T}\right) \nabla_r T\right], \qquad (1.47)$$

$$\text{where } K_n = \frac{1}{4\pi^3}\int \tau\,(\underline{v}\,\underline{v})\,E^{n-1}\frac{\partial f_0}{\partial E}\,d\,\underline{k} \quad (1.48)$$

which for spherical energy surfaces simplifies to

$$K_n = \frac{4}{3m^*}\int N(E)\,\tau\,E^n\frac{\partial f_0}{\partial E}\,d\,E \quad (1.49)$$

2d. Mobility

The mobility (μ) of a carrier is defined by the relationship

$$\bar{\underline{v}} = \mu\,\underline{\mathcal{E}} \quad (1.50)$$

The conductivity is related to the mobility by the expression

$$\sigma = n\,e\,\mu \quad (1.51)$$

Thus from equations 1.46 and 1.51

$$\mu = \frac{e\,\tau}{m^*} \quad (1.52)$$

When more than one type of scattering is present, each of which leads to a different relaxation time, the total relaxation time is given by

$$\tau\,(E)^{-1} = \sum_i \tau_i(E)^{-1} \quad (1.53)$$

So if all $\tau(E)$ have the same energy dependence the mobilities may be added similarly,

$$\mu^{-1} = \sum_i \mu_i^{-1} \quad (1.54)$$

This equation is often used when the energy dependences of the important scattering mechanisms are different. This is a reasonable procedure if approximate results are required.

2e. Electronic Thermal Conductivity

The electronic contribution to thermal current per unit area is given by

$$\underline{Q} = \frac{1}{4\pi^3}\int E\,\underline{w}\,f\,d\,\underline{k} \quad (1.55)$$

and the electronic component of the specific thermal conductivity is defined by the relationship

$$\kappa_e = \frac{-Q}{\nabla_r T} \qquad (1.56)$$

From equations 1.34, 1.37 and 1.55 an expression for Q is obtained .

$$Q = K_2 \left[e\mathcal{E} - T\nabla_r\left(\frac{E_F}{T}\right)\right] - K_3\left[\left(\frac{1}{T}\right)\nabla_r T\right] \qquad (1.57)$$

From this equation, and equation 1.47 a relationship between σ and κ_e may be deduced.

$$\frac{\kappa_e}{\sigma T} = \frac{K_1 K_3 - K_2^2}{e^2 K_1^2} = L \qquad (1.58)$$

L is known as the Lorentz number. If Maxwell-Boltzmann statistics are applied

$$L = (s + \tfrac{1}{2}) \left(\frac{k}{e}\right)^2 \qquad (1.59)$$

and if the electron gas is fully degenerate

$$L = \frac{\pi^2}{3} \left(\frac{k}{e}\right)^2 \qquad (1.60)$$

2f. Lattice Thermal Conductivity

The lattice component of thermal conductivity of a crystal was shown by Liebfried and Schlömann (8) to be of the form

$$\kappa_L = \kappa_o f\left(\frac{\theta_D}{T}\right) \qquad (1.61)$$

Different workers have produced different expressions for the constant κ_o. The variable $f\left(\frac{\theta_D}{T}\right)$ has been shown to be unity when $\frac{\theta_D}{T} = 1$, and for $T > \theta_D$:

$$f\left(\frac{\theta_D}{T}\right) = \frac{\theta_D}{T} \qquad (1.62)$$

and $T < \theta_D$:

$$f\left(\frac{\theta_D}{T}\right) = \left(\frac{T}{\theta_D}\right)^3 \exp\left(\frac{\theta_D}{bT}\right) , \qquad (1.63)$$

where b is a constant.

Thus at high temperatures the lattice component of thermal conductivity is expected to vary as T^{-1}.

The total thermal conductivity of a material at a particular temperature may be found by simply adding the separate components.

$$K = K_e + K_L \qquad (1.64)$$

Section 3: Thermoelectric Effects

3a. Seebeck Effect

A simple thermoelectric circuit is shown in figure 1.6. It is found that for zero current when $T_h = T_c$ that $V_o = 0$. The voltage(V_{ab}) generated in the rest of the circuit is found to be a function of the materials in the couple and of the temperature difference of the junctions. V_{ab} is known as the Seebeck voltage. The Seebeck coefficient (α_{ab}) is defined by

$$d\,V_{ab} = \alpha_{ab} d\,T \qquad (1.65)$$

The sign of the Seebeck coefficient is given by the sign of the voltage of the cold junction with respect to the hot junction.

By definition of the Seebeck voltage, equation 1.47 gives when J = 0,

$$E = \frac{1}{e}\left\{\nabla_r E_f + \left[\frac{K_2}{K_1 T} - \frac{E_f}{T}\right] \nabla_r T\right\} \qquad (1.66)$$

From this expression, and from the definition of the Seebeck coefficient (equation 1.65), the absolute thermoelectric power of a material is defined by the relationship

$$\alpha = \frac{K_2 - E_f K_1}{e\ K_1 T} \qquad (1.67)$$

In practice it is difficult to measure the absolute

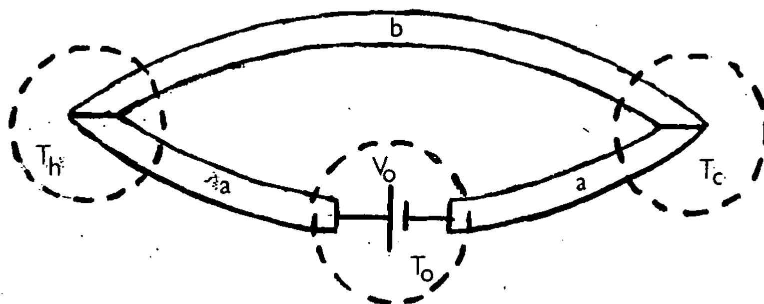

Figure 1.6: A simple thermoelectric circuit composed of two materials a and b.

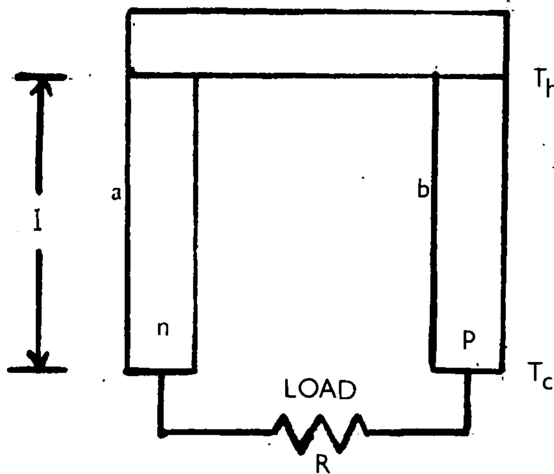

Figure 1.7: Diagrammatic thermoelement.

value of α, but once it has been determined for one material, this material can be used as a reference material. If platinum (Pt) is used as a reference material, the absolute value of the Seebeck coefficient of stannic oxide (SnO_2) will be given by the simple relationship

$$\alpha_{SnO_2} = \alpha_{observed} - \alpha_{Pt} \quad (1.68)$$

The absolute value of the Seebeck coefficient has been measured for tin, copper, silver and lead by Bonelius et al (references 9 - 11). Measurements of the absolute value of the Seebeck coefficient of platinum have been reported by Cusack and Kendall (12) and Nyström (13).

If Fermi-Dirac statistics are assumed, expression 1.67 may be written as

$$\alpha = \pm \frac{k}{e} \left[\frac{(s+5/2)\, F_{s+3/2}(\eta_F)}{(s+3/2)\, F_{s+1/2}(\eta_F)} - \eta_F \right], \quad (1.69)$$

where s is the scattering parameter defined by equation 1.32.

For Maxwell-Boltzmann statistics the same expression reduces to

$$\alpha = \pm \frac{k}{e} \left[(s + \tfrac{5}{2}) - \eta_F \right]. \quad (1.70)$$

3b. Peltier Effect

Again considering figure 1.6, if a current I_{ab} is allowed to flow in the circuit, heat will be absorbed from the surroundings at one junction and emitted at the other. The Peltier coefficient Π_{ab} is defined by the rate of absorption of heat (dq)

$$dq = - \Pi_{ab} I_{ab} \quad (1.71)$$

The Peltier coefficient is related directly to the Seebeck effect by the relationship

$$\Pi = \frac{\alpha}{T} \quad (1.72)$$

3c. Thomsom Effect

If a current flows along a conductor in which a temperature gradient exists, heat must be exchanged with the surroundings if the original temperature distribution is to be maintained. The Thomson coefficient τ is defined by

$$dq = \tau \, d \, I \frac{\partial T}{\partial x} \quad . \qquad (1.73)$$

The Thomson coefficient is related to the Seebeck coefficient by the relationship

$$\alpha = \int_0^T \frac{\tau}{T} \, d \, T \quad . \qquad (1.74)$$

It is this relationship that enables the absolute value of α to be measured (see references 9 - 11).

3d. Irreversible Effects

For a complete treatment of the thermoelectric effects that could occur in a circuit as shown in figure 1.6, the effect of Joule heating, which is proportional to the square of the current flowing, and of the thermal conductivity, which is proportional to the temperature gradient along the conductors, must be considered. The thermodynamics of the full situation have been worked out by Onsager (14) and Domenicali (15). The main results are identical with those of Thomson (16) which are quoted in the previous sections.

3e. Efficiency of a Thermoelectric Generator

Figure 1.7 shows diagrammatically the arrangement for a simple thermoelectric generator connected across a load resistance R. The efficiency (ϕ) of such a device will be given by

$$\phi = \frac{I^2 R}{Q_h + Q_c - \frac{1}{2} I^2 r} \quad , \qquad (1.75)$$

where I^2R is the external work done by the device, Q_c is the Peltier heat transferred to the cold junction by conduction, $\frac{1}{2}I^2r$ is the amount of Joule heat transferred back to the hot junction and r is the internal resistance of the thermoelement.

From the Peltier effect relationships

$$Q_h = \alpha I T_h \quad (1.76)$$

By the definitions of thermal and electrical conductivity

$$Q_c = (K_a A_a + K_b A_b) \frac{T_h - T_c}{l'} \quad (1.77)$$

and
$$r = \left(\frac{l'}{\sigma_a A_a} + \frac{l'}{\sigma_b A_b} \right) . \quad (1.78)$$

here A_a and A_b are the cross sectional areas of the elements a and b and l' is the length of the elements.

The current flowing in the circuit will be given by

$$I = \frac{\alpha (T_h - T_c)}{R+r} \quad (1.79)$$

If these expressions are substituted into equation 1.75 it can be deduced that for maximum efficiency the following relationship must exist

$$\frac{K_b \sigma_b}{K_a \sigma_a} = \left(\frac{A_a}{A_b} \right)^2 \quad (1.80)$$

and
$$\frac{R}{r} = M = \left[1 + \tfrac{1}{2} Z' (T_h + T_c) \right]^{-2} , \quad (1.81)$$

where
$$Z' = \alpha_{ab}^2 \left[\left(\frac{\sigma_a}{K_a} \right)^{1/2} + \left(\frac{\sigma_b}{K_b} \right)^{1/2} \right]^{-2} \quad (1.82)$$

The expression for the maximum efficiency is then

$$\phi_{max} = \left(\frac{T_h - T_c}{T_h} \right) \left(\frac{M - 1}{M + T_c/T_h} \right) , \quad (1.83)$$

Z is known as the figure of merit of the thermo-element. It is the only factor in the equations that is dependent on the materials.

3f. Figure of Merit

From the relationship 1.82, the figure of merit of a single material is usually written as

$$Z = \frac{\alpha^2 \sigma}{K} . \tag{1.84}$$

If we now substitute for the individual parameter in Z the relationships given in equations 1.51, 1.18, 1.69, 1.58 and 1.64, the product of ZT for an n-type semi-conductor may be written

$$ZT = \frac{A\,(\delta - \eta_F)^2 \quad F_{1/2}(\eta_F)}{1 + \gamma A \quad F_{1/2}(\eta_F)} , \tag{1.85}$$

where $A = \left(\frac{k}{e}\right)^2 N_c \quad T\left(\frac{\mu}{K_L}\right)$, $\delta = \frac{(s+5/2)\ F_{s+3/2}(\eta_F)}{(s+3/2)\ F_{s+1/2}(\eta_F)}$

and $\gamma = L\left(\frac{e}{k}\right)^2$.

Remembering that $N_c \propto m^{*3/2}$, it is seen that for a good thermoelectric material, the quantity

$$A \propto \frac{m^{*3/2}\mu}{K_L} \tag{1.86}$$

should be as large as possible.

Section 4: Hall Effect

4a. Hall Coefficient

If a current (I_x) flows along a bar of conductor in a magnetic field (H_z) as shown in figure 1.8, the deflection of the carriers by the magnetic field will give rise to a voltage (V_y) across the specimen.

The force in the y-direction (F_y) on an electron moving with velocity V_x in the x-direction will be given by

$$F_y = \frac{1}{c}\, e v_x\, H_z \tag{1.87}$$

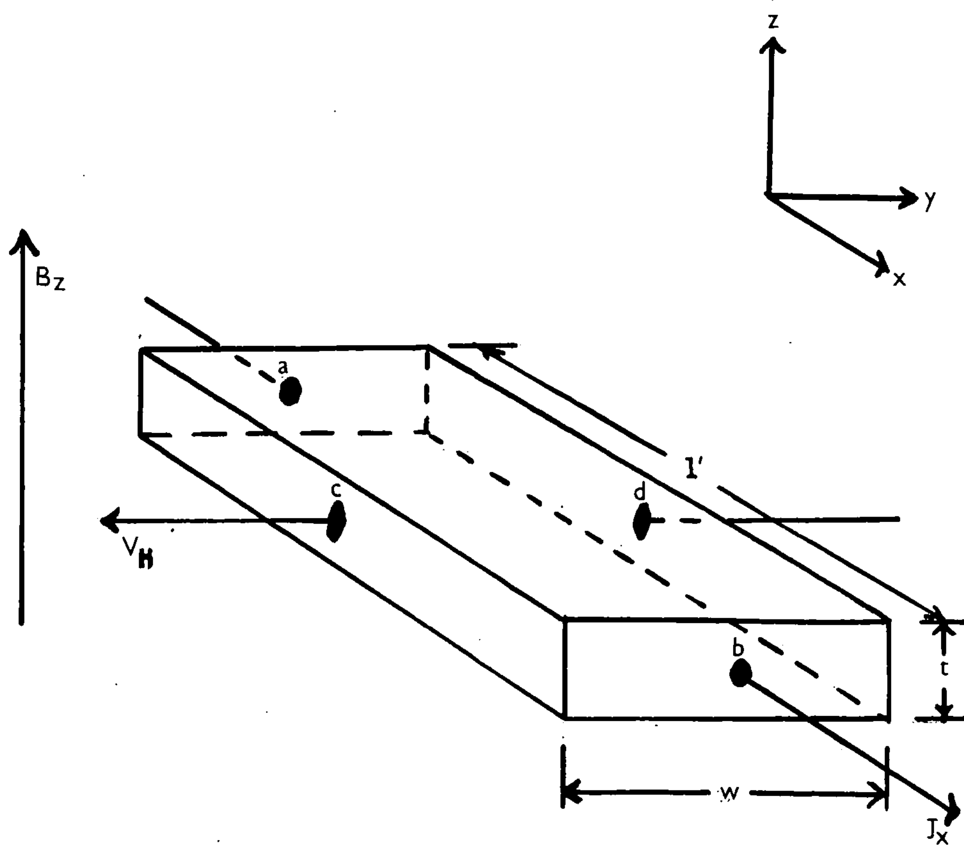

Figure 1.8: Hall effect in a rectangular bar conductor in a magnetic field B_z. An electric current of density J_x flowing from a to b, causes a Hall voltage V_H across c d.

The current density (J_x) is given by

$$J_x = n\ e\ v_x \tag{1.88}$$

Substituting for v in equation 1.87

$$F_y = \frac{J_x\ H_z}{nec} = R\ J_x\ H_z \tag{1.89}$$

In quantities actually measured

$$R = \frac{V_y\ \ t}{H_z\ \ I_x} \tag{1.90}$$

where t is the thickness of the specimen, V_y is the Hall voltage and R is known as the Hall coefficient.

From equation 1.89 it can be seen that the Hall coefficient R is given by

$$R = \frac{1}{nec} \tag{1.91}$$

This is true for a degenerate conductor. A more rigorous treatment, as given in section 4b below, gives the result

$$R = \frac{r}{nec} \tag{1.92}$$

where r is the ratio of the Hall mobility defined by

$$\mu_H = R\sigma \tag{1.93}$$

and the drift mobility defined by equation 1.50.

4b. <u>Ratio of Hall Mobility to Drift Mobility</u>

When a magnetic field is present, under isothermal conditions, from equations 1.31 and 1.33, the wave function must satisfy the equation

$$\underline{\psi} + \frac{\mu}{\tau}\,\underline{H} \wedge \underline{\psi} = \tau\,\underline{\mathcal{E}}\ , \tag{1.94}$$

where $\mu = \dfrac{e\,\tau}{m^*}$.

If the equation 1.47 is now written in component form, using the relationship 1.94, the expressions obtained are

$$\left.\begin{aligned} J_x &= e^2 \mathcal{E}_x K_1' + e \mathcal{E}_y K_1'' \\ J_y &= e^2 \mathcal{E}_y K_1' - e \mathcal{E}_x K_1'' \end{aligned}\right\} \qquad (1.95)$$

where τ in the expression 1.49 for K_n is replaced by

$$\frac{\tau}{1 + (\mu H)^2} \text{ for } K' \text{ and } \frac{\mu \tau H}{1 + (\mu H)^2} \text{ for } K''.$$

Assuming a Maxwell-Boltzmann distribution of the carriers, and spherical energy surfaces, equation 1.95 reduces to

$$\left.\begin{aligned} J_x &= \frac{ne}{m^*}\left\{ \mathcal{E}_x \left\langle \frac{\tau}{1+(\frac{\mu}{c}H)^2} \right\rangle + \mathcal{E}_y \left\langle \frac{\frac{\mu}{c}\tau H}{1+(\frac{\mu}{c}H)^2} \right\rangle \right\} \\ J_y &= \frac{ne}{m^*}\left\{ \mathcal{E}_y \left\langle \frac{\tau}{1+(\frac{\mu}{c}H)^2} \right\rangle - \mathcal{E}_x \left\langle \frac{\frac{\mu}{c}\tau H}{1+(\frac{\mu}{c}H)^2} \right\rangle \right\} \end{aligned}\right) \qquad (1.96)$$

where the symbol $\langle \tau \rangle$ represents the average value of $\tau(E)$ over the Boltzmann distribution.

$$\langle \tau \rangle = \frac{4}{3\sqrt{\pi}} \int_0^\infty \tau \eta^{3/2} \exp(-\eta)\, d\eta. \qquad (1.97)$$

If $\frac{\mu}{c}H \ll 1$ it is seen from equation 1.96 that

$$\mu_H = \frac{e}{m^*}\frac{\langle \tau^2 \rangle}{\langle \tau \rangle} \quad \text{and} \quad \mu_D = \frac{e \langle \tau \rangle}{m^*}, \qquad (1.98)$$

$$\text{therefore } r = \frac{\langle \tau^2 \rangle}{\langle \tau \rangle^2}. \qquad (1.99)$$

When the energy dependence of τ is considered

$$r = \frac{\Gamma(5/2)\, \Gamma(5/2 + 2s)}{\left[\Gamma(5/2 + s)\right]^2}, \qquad (1.100)$$

where the gamma function

$$\Gamma(z) = \int_0^\infty e^{-x} x^{z-1}\, dx,$$

if z is an integer $\Gamma(z) = (z - 1)!$

Equation 1.100 gives the particular results :-

for acoustic mode scattering

$$(s = -\tfrac{1}{2}) \qquad r = \frac{3\pi}{8} = 1.18 , \tag{1.101}$$

for optical made scattering

$$(s = \tfrac{1}{2}) \qquad r = \frac{45\pi}{128} = 1.10 , \tag{1.102}$$

and for ionised impurity scattering

$$(s = \tfrac{3}{2}) \qquad r = \frac{315\pi}{512} = 1.93 . \tag{1.103}$$

Section 5. Electron Scattering Mechanisms

5a. Introduction

An electron wave packet travelling through a perfect lattice will do so without any resistance to its motion. However, any deviation from perfect periodicity of the lattice will scatter the electrons. These deviations fall into two classes

(i) vibrations of the lattice

(ii) imperfections in the lattice structure.

5b. Phonons

For a crystal containing N atoms there are 3N independent modes of vibration of the lattice. These vibrations may be described as lattice waves and classified as longitudinal or transverse, depending on whether the direction of vibration is approximately parallel or perpendicular to the direction of propagation of the wave. There are two transverse waves but only one longitudinal one. In a crystal with n atoms per unit cell there are n kinds of wave of each of the three types.

Each vibrational mode is described by its wave vector $\underline{q}$ and index p which characterises the type of vibration and its circular frequency $\omega(p,\underline{q})$. Figure 1-9 shows a typical frequency spectrum for lattice waves. The energy of each vibrational mode is quantised, the quanta being

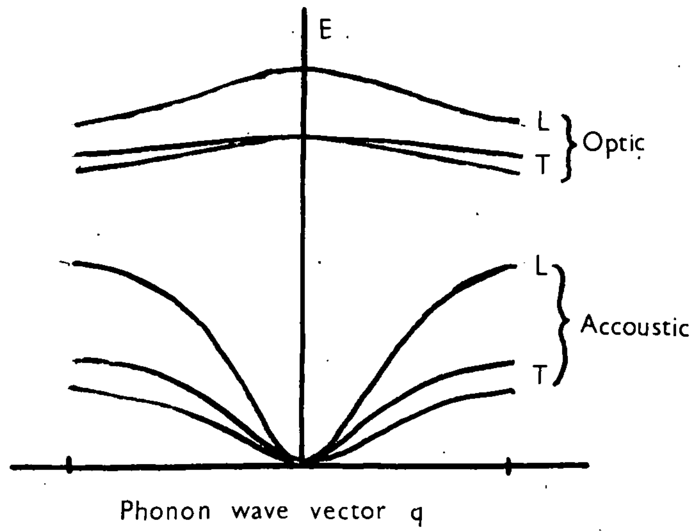

Figure 1.9: Frequency spectrum for phonons in a polar solid containing two atoms per unit cell.

L = longitudinal
T = transverse

N.B. For a more complete picture, it should be mentioned that there are two types of acoustic mode scattering. Deformation potential scattering is the most important as it can occur in any solid, and is thus discussed briefly in Chapter 1 Section 5c. The other type is polar acoustic or piezo-acoustic scattering. This type of scattering only occurs in crystals that are piezoelectric. Since the structure of stannic oxide has a centre of symmetry, it is not piezoelectric and so piezo-acoustic scattering is not considered.

known as phonons. Phonons obey Bose-Einstein statistics. This means that the average number of phonons ($\bar{n}$) is a state $\underline{q}$, p is given by

$$\bar{n}(\underline{q}, p) = \exp\left[\frac{\theta(\underline{q}, p)}{T} - 1\right]^{-1}, \qquad (1.104)$$

$$\text{where } \theta(\underline{q}, p) = \frac{\hbar\,\omega\,(\underline{q}, p)}{k}. \qquad (1.105)$$

is the characteristic temperature of the phonons.

5c. Acoustic Mode Lattice Scattering

If only one phonon is involved in the scattering process, the strength of scattering should be proportional to the number of phonons present. Thus M(T) in equation 1.32 will have a temperature dependence of $(\exp\frac{\theta}{T} - 1)$ which for $T \gg \theta$ means that the relaxation time τ will vary as T^{-1}.

The characteristic temperature for acoustical phonons is usually about 50° K.

Bardeen and Shockley (17) solved the problem of acoustic mode scattering by a deformation potential method. It is seen from figure 1.1. that a variation in lattice constant produces a change in energy of the band edge. The longitudinal phonons produce a local dilation that can be interpreted as a change in the band edge, which causes the scattering of the electrons. The expression they produce for the relaxation time is

$$\tau = \frac{h^4 c_{11}\,\rho\,E^{-\frac{1}{2}}}{8\,\pi^3\,(2m^*)^{3/2}\,kTd_1^2}, \qquad (1.106)$$

where c_{11} is the longitudinal component of strain in the direction of propagation, ρ is the density of the solid and d_1 a constant known as the deformation potential constant.

Thus the scattering parameter $s = -\frac{1}{2}$ and M(T) varies as T^{-1}. If the Boltzmann distribution of energy is assumed, the expression for the mobility is

$$\mu = \frac{(8\pi)^{\frac{1}{2}} e \hbar^4 c_{11} \rho}{3(kT)^{3/2} m^{*\,5/2} d_1^2} \qquad (1.107)$$

Thus the mobility varies as $T^{-3/2}$ and $m^{*\,-5/2}$.

In the fully degenerate situation, the mobility will vary as T^{-1}, but Harrison (18) has pointed out that for a degenerate multivalley band, the mobility due to acoustic mode scattering should vary as $T^{-\frac{1}{2}}$.

5d. Optical Mode Lattice Scattering

For optical modes the characteristic temperature does not depend strongly on wavelength and is usually in the range 250-600° K. So near room temperature the full expression 1.104 must usually be used for the phonon density.

There are two types of scattering by optical modes. In ionic crystals, the atoms carry a charge and the optical mode vibrations cause an electric polarisation of the lattice which scatters the electrons. In an elemental semiconductor, all atoms are similar and, although there can be no polarisation, scattering is still caused by the lattice distortion produced.

The latter case has been considered in detail by Harrison (18). He expects that at room temperature optical mode scattering would be of the same order as acoustical mode scattering in most cases. Since stannic oxide is a polar crystal, the former case will be considered in more detail.

A free electron introduced into a polar lattice will cause a distortion of the lattice. The term

'polaron' is used to describe the combination of the electron and the distortion. The strength of the interaction between the electrons and the polar modes, or coupling constant (α_c), is given by the formula

$$\alpha_c = \left(\frac{e^2}{h}\right) \left(\frac{m^*}{2\hbar\omega_L}\right)^{\frac{1}{2}} (\epsilon_\infty^{-1} - \epsilon_o^{-1}) , \quad (1.108)$$

where ϵ_o and ϵ_∞ are the dielectric constants of the crystal at low and high frequences. If α_c is small ($\ll 1$) a perturbation theory approach to the motion of the electrons may be used, but for stronger coupling a polaron theory must be used.

The problem was first considered by Fröhlich (19) who produced an expression for the relaxation time in a polar crystal at high temperatures as

$$\tau = \frac{a^3 M(\hbar\omega)^2 E^{\frac{1}{2}}}{2\pi(2m^*)^{\frac{1}{2}} e^4 kT} , \quad (1.109)$$

where M is the reduced mass of the ions and 'a' is the interatomic distance. Thus $s = \frac{1}{2}$ for optical mode scattering and in the degenerate case $\mu \propto T^{-1}$. Using the Fröhlich model, Howarth and Sondheimer (20) set up the Boltzmann equation and solved it by a variational method. They produced expressions for the thermoelectric power and electrical conductivity for all temperatures, for both the degenerate and non-degenerate cases, which should be valid for small α_c ($\ll 1$).

The expression for the mobility, as reformulated by Petritz and Scanlon (21) in the non-degenerate case is

$$\mu = \frac{8h^2}{3e} (2\pi m^* k \theta_L^2)^{-\frac{1}{2}} (\epsilon_\infty^{-1} - \epsilon_o^{-1})^{-1} \; Z^{-1} (e^Z - 1) \chi(Z), \quad (1.110)$$

where $\theta_L = \frac{\hbar\omega_L}{k}$, $Z = \frac{\theta_L}{T}$ and $\chi(Z) = 1$ for $Z \ll 1$

and $\frac{3(\pi Z)^{\frac{1}{2}}}{8}$ when $Z \gg 1$.

For the degenerate case, the conductivity may be formulated as

$$\sigma = \frac{4(kT)^2}{3\pi^2\hbar^2(\epsilon_\infty^{-1}-\epsilon_0^{-1})\omega_L} \frac{\tau_f^2 \sinh^2 Z/2}{Z} \qquad (1.111)$$

Thus for degeneracy $\sigma \propto \frac{1}{T}$ at high T, and $\sigma \propto T \exp(Z)$ at low T.

Various formulae have been proposed for the polaron-mobility in the case of intermediate coupling ($\alpha_c < 6$). All these formulae are only valid at low temperatures ($T \ll \theta$).

The earliest of these, proposed by Lee, Low and Pines (22, 23, 24), gives the relationship

$$\mu = \frac{e}{2 m \omega \alpha_c} \left(\frac{m^*}{m_p}\right) f(\alpha_c) \exp Z \qquad (1.112)$$

where $m_p = m^* (1 + \alpha_c/6)$ is known as the polaron mass and $f(\alpha_c)$ is a slowly varying function of α_c tabulated in reference 24.

More recent theories of Feynman et al (25) and Schultz (26) propose slightly different formulae for the mobility. The former proposes that $\mu \propto \frac{\exp Z}{Z}$ and the latter that $\mu \propto (\exp Z - 1)$.

Recently, theories have been proposed for the behaviour of small polarons (the situation where α_c is very large), but these are beyond the scope of the present work.

5e. Scattering by Ionised Impurities

Impurities, different in valence from the host lattice, give rise to long range coulomb fields, in the semiconductor, with a potential of the form

$$V(r) = \frac{e^2}{\epsilon r} \qquad (1.113)$$

where ϵ is the macroscopic dielectric constant of the semiconductor.

The problem was first considered by Conwell and Weisskopf (27). By ignoring scattering processes which

occured between incident electrons and impurities that were at distances greater than half the mean distance between impurity ions, they calculated that, if the Rutherford scattering of the electrons was the dominant process, the mobility in the non-degenerate case would be given by

$$\mu = \frac{8}{\pi}\sqrt{\frac{2}{\pi}}\;\frac{(kT)^{3/2}}{N_I e^3 m^{*1/2}}\left[\ln\left\{1 + \left(\frac{3\epsilon kT}{e^2 N_I^{3}}\right)^2\right\}\right]^{-1}, \qquad (1.114)$$

where N_I is the density of ionised impurity ions.

A more rigorous formula was obtained by Brooks (24)

$$\mu = \frac{2^{7/2}(kT)^{3/2}\epsilon^2}{\pi^{3/2} e^3 m^{*1/2} N_I}\left[\ln\ (1+b) - \frac{b}{1+b}\right]^{-1}, \qquad (1.115)$$

where $b = \dfrac{6m^*\ (kT)^2\ \epsilon}{\pi e^2\ \hbar^2\ N_I}$

This expression is identical to the one obtained by Mansfield (29), who also produced an expression for arbitrary degeneracy, which in the degenerate limit reduces to

$$\mu = \frac{3\ h^3\ \epsilon^2}{16\pi^2 e^3\ m^{*2}}\left[\ln\ (1+b) - \frac{b}{1+b}\right]^{-1}, \qquad (1.116)$$

where $b = \left(\dfrac{h}{e}\right)^2 \dfrac{\epsilon}{m^*} \left(\dfrac{3N_I}{8\pi}\right)^{1/3}$

In the degenerate case it is seen that the mobility is only dependent on the number of impurities through the logarithmic term and it is independent of temperature.

In the non-degenerate case, if the relatively small variation of the logarithmic term is ignored, the mobility should vary as $T^{3/2}$.

The scattering parameter (s) is equal to $3/2$ for ionised impurity scattering.

These formulae were deduced on the assumption that

the host lattice was non-ionic. Modification may be necessary if the material is wholly or partially ionic.

5f. Neutral Impurity Scattering

This type of scattering is only important at very low temperatures when most of the charge carriers are in the bound levels of the donors or acceptors. The effect has been discussed by Sclar (30).

5g. Dislocation Scattering

The effect of scattering due to the microscopic deformation of the crystal lattice at dislocations has been considered by Dexter & Seitz (31) who conclude that it is only important at very high dislocation densities (10^8-10^{10} dislocation lines /cm^2).

Read (26) has discussed the possibility of dislocations acting as acceptors. In n-type material the dislocation will be negatively charged, and be surrounded by a region of equal positive charge. This may be in the order of a micron in diameter. If the mean free path of the carriers, due to other scattering mechanisms, is small compared with the distance between dislocations, the electrons will tend to follow curved paths to avoid the dislocation region. An increase in resistivity will result. If the mean free path of the carriers is large, the carriers could be scattered by the space charge about the dislocation.

5h. Electron-Electron Scattering

Electron-electron scattering does not affect the mobility directly as the total energy, before and after a collision, is unchanged. However, these collisions can redistribute the energy so that other mechanisms can remove it more effectively.

6. Bonding

6a. Introduction

The simple model of an atom is a nucleus, around which orbit a number of electrons. These orbits have discrete energy levels and the electrons fill them according to the Pauli exclusion principle, which allows two electrons of opposite spin in each level. The lowest levels are filled first. Certain numbers of electrons make up a complete shell. The details of the electron configurations for the ground states of the elements may be found in text books such as Cartmell and Fowles (33). The important point is that only the electrons in the outer incomplete shells take part in bonding. There are many theories and types of bonding. Only the two most important will be considered here.

6b. Ionic Bonding

Both the tin and the oxygen atoms in stannic oxide require eight electrons to complete their outer shells. The tin atom already has four. The oxygen atom has six. For ionic bonding, the tin atom can give up its four outer electrons, becoming a quadruply charged, positive ion. These electrons are accepted by the oxygen atoms, two being needed to complete their outer shells, which then become doubly charged, negative ions. The tin and oxygen ions therefore pack themselves in a crystal lattice with two oxygen atoms for every tin atom. If this were the complete story, stannic oxide would not be a semiconductor, but an insulator. However, ionic bonding does play an important role.

6c. Covalent or Valence Bonding

When atoms are in close proximity, it is possible for

the wave functions, which describe the motion of the electrons in their separate orbitals, to overlap. When this occurs it is possible for an electron in an orbital in one atom to be shared between the two atoms. The usual situation is for the atoms to share electrons in such a way as to form complete outer electron shells about each of themselves. Thus two electrons, each of opposite spin, effectively orbit both atoms in the bonding orbitals.

6d. Directed Valency or Hybridisation

In order to obtain a stable bond in a lattice, where each atom has N nearest neighbours, it is necessary that there are N energy levels, with one electron in each, that can pair with electrons of similar energy but of opposite spin, on the neighbouring atoms. It thus becomes possible for an electron in a paired energy state, to be donated to a different state creating two unpaired electrons which may take part in bonding.

6e. Semiconducting Bond

Mooser and Pearson (34) have shown that semiconductor behaviour in a solid is the result of predominantly covalent bonds. In elemental semiconductors, the process of electron sharing must lead to completely filled 's' and 'p' orbitals in all atoms. In a semiconducting compound, only one atom of any two bonded together need acquire closed 's' and 'p' orbitals. The presence of unfilled orbitals in some atoms does not result in metallic behaviour of the solid, provided that these atoms are not bonded together.

6f. Nature of the Bond in Stannic Oxide

Coulson (35) gives a formula for the percentage ionic character (% i.c.) of a molecular bond as :-

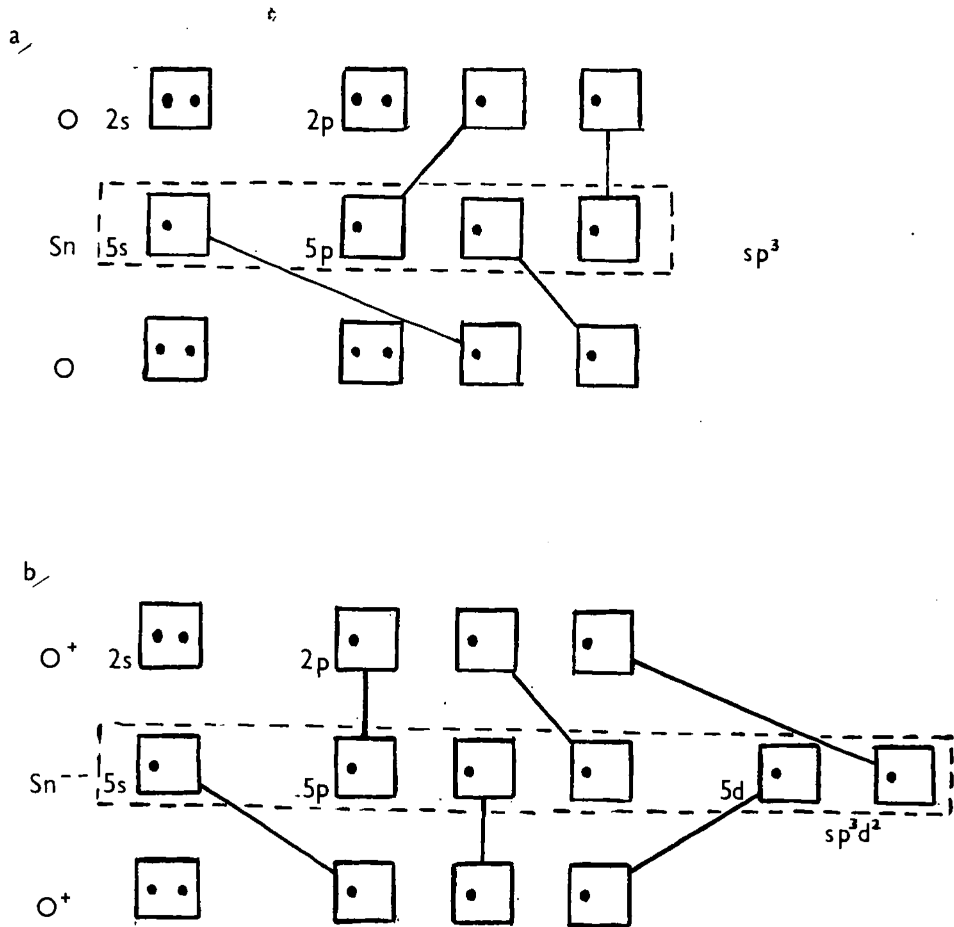

Figure 1.10: Electron sharing schemes for the covalent bond in stannic oxide for co-ordination numbers of (a) four and (b) six.

$$\% \text{ i.c.} = 16 |X_A - X_B| + 3.5 |X_A - X_B|^2,$$

where X_A and X_B are the values of the electronegativity of the two atoms. The electronegativity of tin and oxygen of are given by Pauling (36) as 1.8 and 3.5 respectively. Using these figures it is concluded that the bond in stannic oxide is 37% ionic.

Stannic oxide has a rutile structure, which means that each tin atom is surrounded by an octahedral arrangement of six nearest neighbour oxygen atoms. This octahedron is slightly distorted such that two atoms of these six are at a slightly greater distance from the tin atom than the other four. Mooser and Pearson (34) have proposed electron sharing schemes for co-ordination numbers 4 and 6 which satisfy the rules for a semiconductor bond in rutile (TiO_2). These schemes can be adapted for stannic oxide. The electronic configuration of tin requires $s\,p^3d^2$ hybridisation for a co-ordination number of 6 and $s\,p^3$ hybridisation for a co-ordination number of 4. The two possible schemes are shown in figure 1.10. It is probable that both schemes make a contribution towards the covalent bonding in the stannic oxide molecule.

CHAPTER II

Crystal Growth, Habit and Structure

Section 1. Physical Chemistry of the Tin-Oxygen System

1a. General

The tentative phase diagram shown in figure 2.1. was originally proposed by Spandau et al (37, 38). It has been modified according to the results of Donaldson et al (39, 40) who showed by X-ray analysis, that the disproportionation products of SnO_2 above 385°C are Sn and SnO rather than Sn_3O_4 as originally suggested.

It is now established that there are two oxides of tin, stannous oxide (Sn O) and stannic oxide (SnO_2).

Although stannous oxide exists in a solid form at temperatures up to 380°C, thermodynamic calculations show that it is unstable relative to tin metal and $Sn\,O_2$ from 25°C to 380°C (41). Brewer (42) reports that Sn O is the stable component in the vapour phase in the tin oxygen system.

Kryzhanovskii and Kuznetsov (43) have reported the electronic properties of Sn O in a compressed powder form. It was interesting that they found p-type conduction in some of their samples, before heat treatment. Since the stoichometry of their specimens is not known, the interpretation of their results is impossible. Single crystals of stannous oxide larger than 50 microns have not been grown.

Vapour pressure curves of tin and its oxide are reproduced in figure 2.2. Curve 1 for Sn O was obtained

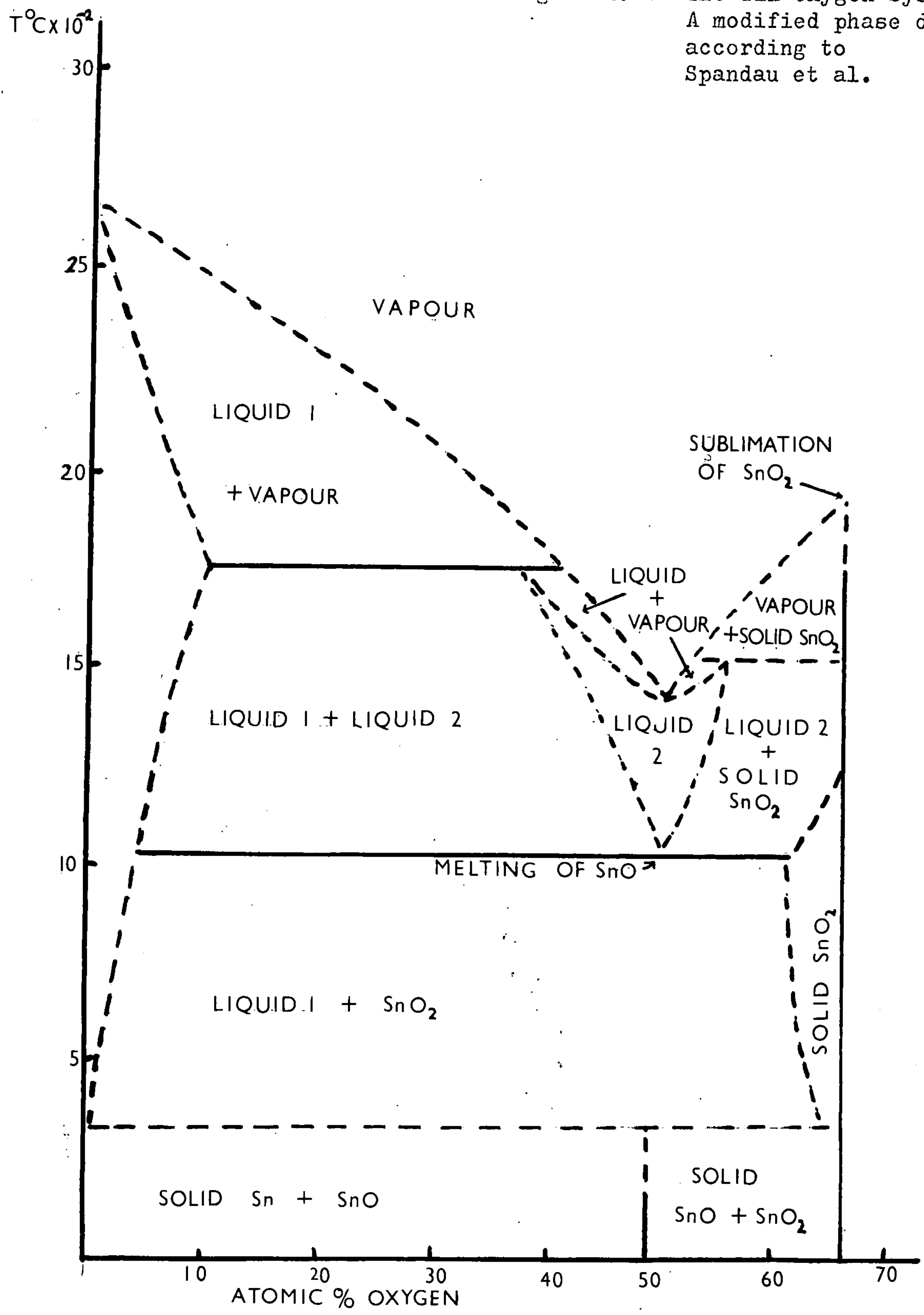

Figure 2.1: The Tin Oxygen System. A modified phase diagram according to Spandau et al.

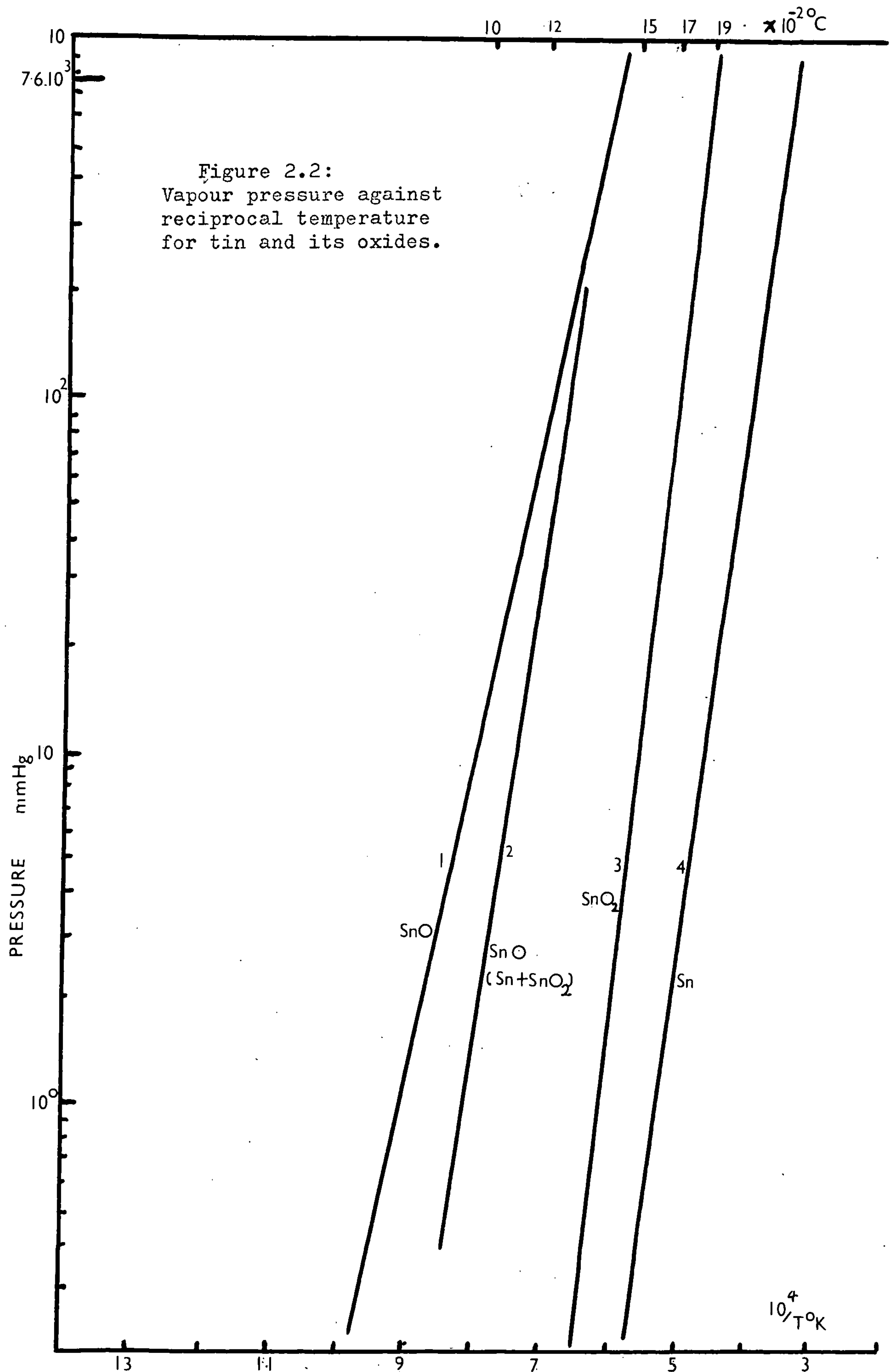

Figure 2.2:
Vapour pressure against reciprocal temperature for tin and its oxides.

by Spandau and Kohlmeyer (37). Curve 4 for Sn metal was calculated from the thermodynamic data (41). Curve 2 was determined by Platteeuw and Meyer (44) from equimolar mixtures of Sn and $Sn\ O_2$. The discrepancies between curves 1 and 2 are not explained although the extreme reactivity of Sn O at high temperatures makes experimentation difficult.

1b. Decomposition of Stannic Oxide

Stannic oxide decomposes at high temperatures according to the reversible reaction:

$$Sn\ O_2 \rightleftharpoons Sn\ O + \tfrac{1}{2} O_2 \qquad (2.1)$$

Marley and McAvoy (45) calculated the free energy for this reaction and then the "decomposition pressure" of $Sn\ O_2$ (the apparent vapour pressure of $Sn\ O_2$). The result is shown as curve 3 in figure 2.2. This curve can be expressed by the equation:

$$\log P(mm) = 11.23 - (1.822 \times 10^4) / T\ ^\circ K \qquad (2.2)$$

It can be seen from figure 2.2 that the apparent sublimation point of $Sn\ O_2$ is about 1850° C. According to the handbook of Chemistry & Physics (46) $Sn\ O_2$ decomposes at 1127° C. My own observations show no change in single crystal specimens heated to this temperature for short periods but evaporation begins to take place rapidly above about 1500° C.

No true estimate of the melting point of $Sn\ O_2$ has been made. In studies of diffusion Goodman and Gregg (47) have estimated the Tamman temperature of $Sn\ O_2$ to be 1100° C. Since this temperature is usually half that of the melting point, they estimated the melting point of $Sn\ O_2$ to be in the region of 2500° C. This could only be observed under many hundred atmospheres pressure of

oxygen, so crystal growth from the melt would be an extremely difficult operation.

Section 2. Growth from the Liquid Phase

2a. Fluxed Melt

One of the simplest methods of crystal growth can be the growth from a saturated solution. This method is extremely convenient with the common salts which are water soluble as crystal growth can take place at or near room temperature. Crystals grown by this method can be relatively free of thermal defects due to the low temperature of growth, but high purity can be difficult to achieve since crystals tend to contain inclusions of the solvent, and foreign atoms originating from the solvent and impurities in the solvent.

There are two basic methods of controlling crystal growth by this method. The first is by controlling the temperature of the saturated solution, such that as the solution cools, the excess solute deposits on the seed crystals. The second method is by controlling the rate of evaporation of the solvent.

Since there is no known room temperature solvent for stannic oxide, a brief survey was made of fluxes that have been used for growing similar materials at higher temperatures. Zinc oxide, for instance, may be grown from a melt of lead fluoride (48) and barium titanate from a melt of anlydrous potassium fluoride (49).

PbO, PbF_2, $PbCl_2$, KF, KCl, B_2O_3 and $CaCl_2$ were used as fluxes. The general procedure was to pütcc the salt with 20% by weight of SnO_2 powder in a platinum crucible. The crucible was placed in an electrical furnace and heated to about 1200° C – the actual temperature depended on the rate of evaporation of the particular flux – for 2 - 4 hours to

allow the solution of Sn O_2 into the flux. The furnace was then cooled at 10° C per hour until the solidification temperature of the flux was reached, after which the furnace was turned off. When cool, the resultant mixture was examined. The flux was leached out with a suitable solvent, usually water or nitric acid, and the Sn O_2 remaining examined for any change of form. The only partial success was obtained with a flux of lead oxide. A few very small reddish crystals were obtained. These crystals were rods or whiskers and were too small for either electrical or optical measurements to be made.

There are many inherent disadvantages of this method. The high volatility of the solvents at high temperatures makes the control of evaporation difficult. A platinum lid was crimped over the crucible to prevent as much evaporation as possible in the experiments. The high viscosity of most of these fluxes, including lead oxide, means that transport of the solute to the growing regions is slow and irregular. And as stannic oxide appeared to be less soluble than most impurities, this method was abandoned in favour of the more successful vapour phase method. Marley and MacAvoy (45) obtained similar results and quote the solubility SnO_2 in Pb O as less than 15% by weight at 1200° C.

Recently, Kunkle and Kohnke (50) have grown stannic oxide crystals from a flux of copper oxide (Cu_2O). The crystals are rods (1 mm^2 x 5 to 10 mm) and are reported to contain very little impurity.

2b. Hydrothermal Synthesis

Certain materials which are not very soluble in water under normal conditions can become so under conditions of very high temperature and pressure. Under controlled

conditions it is possible to obtain crystal growth from this state. With all probability, natural deposits of cassiterite were deposited hydrothermally and it should thus be possible to grow synthetic $Sn\ O_2$ by this method. Kus'mina and Litvin (51) have recently reported the hydrothermal synthesis of $Sn\ O_2$ from a solvent of Li O H solution at 400 - 600° C. and 2000 atmospheres pressure. No information is available on the dimensions or properties of these crystals.

Section 3. Growth from the Vapour Phase

3a. Sublimation in a Closed System

If stannic oxide were heated up to 1300° C in a scaled evacuated silica tube, from the figure given for the temperature of decomposition (1127° C) in reference 46, it might be expected that transport of material from the hot end to the cold end would occur; and if this could be controlled, single crystals could be grown at thecool end of the tube. This method works very well for cadmium sulphide (Cd S) which has a much lower sublimation temperature (52). CdS can also be grown at lower temperatures if iodine is introduced into the system, so that the reaction:

$$Cd\ S + I_2 \leftrightharpoons Cd\ I_2 + S \qquad (2.3)$$

takes place (53). The direction of transport depends on whether the reaction (23) is exothermic or endothermic.

Reagent grade stannic oxide powder was placed at one end of a sealed, evacuated silica tube. This tube was inserted into a furnace, such that a temperature gradient existed between the two ends. The stannic oxide powder was at the hot end of the tube, which was maintained at temperatures which varied between 1000° C and 1300° C

for different runs. A few small crystals were produced by this method. They were usually of habit 3 (see section 6). The introduction of iodine gave a slight improvement on one run. The crystals were formed at the hot end of the tube, on top of the original charge. This result could not, however, be repeated.

3b. Hydrolysis of Stannic Chloride

Thin films of stannic oxide that are used as resistors or transparent electrodes are usually prepared by the hydrolysis of stannic chloride (54, 55). They are usually formed by spraying an alcoholic or hydrochloric aqueous solution of stannic chloride on to a heated substrate such that the reaction (2.4) takes place.

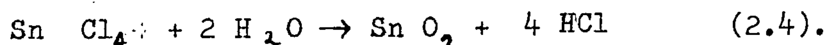

$$SnCl_4 + 2H_2O \rightarrow SnO_2 + 4HCl \qquad (2.4).$$

Recently Nagasawa et al (56) have shown that by suitably controlling this reaction single crystals may be grown. Their method entails passing oxygen over water and nitrogen over stannic chloride and allowing the streams to meet in an electrically heated furnace at 1300° C. Single crystals of up to 2 x 5 x 15 mm have been reported.

A similar method was tried in this laboratory. A large mass of crystalline material was formed, but individual crystals were difficult to separate and orientate. The crystals were white and opaque. The opacity was probably due to voids in the crystal structure which were encouraged by the low surface mobility of ions at the low temperature of formation.

3c. Vapour Phase Flame Fusion

Sapphire (Al_2O_3) has been grown by the hydrolysis of Al_3Cl_4 in an oxy-hydrogen flame, the temperature of which is adjusted to keep a molten surface on the growing crystal. The method has been described by Curtis (57).

Stannic oxide will be formed by the hydrolysis of stannic chloride ($Sn\ Cl_4$) in an oxy-hydrogen flame. The reaction is similar to equation (2.4) where the H_2O is formed by the burning of hydrogen in oxygen. As stannic oxide does not melt, but sublimes under atmospheric pressure, large single crystals could not be grown by this method. However, it was possible to grow bunches of thin dendritic needles. These needles were interesting in that they provided the best luminescent stannic oxide (see Ch. 3. sect. 5).

3d. Helium Flow Method

The most successful method of growing $Sn\ O_2$ crystals has been reported by Marley and MacAvoy (58). The starting material was very pure stannic oxide powder which was placed in the hot zone (1650° C) of a platinum wound furnace. A helium-oxygen mixture was passed over the powder and the crystals formed on a mullite substrate at a cooler part of the furnace. Crystals of up to 2 x 4 x 30 mm are reported. Studies of etch pits by Koffyberg (59) show that they have a dislocation density of 10^4 or $10^5\ cm^{-2}$. One of the conclusions of Marley and McAvoy was that the crystal habit was very dependent on temperature. Table 2.1 shows these conclusions.

Table 2.1 Growth habit and temperature according to Marley and McAvoy.

T °C	Habit
1620 - 1570	rods
1570 - 1460	twinned plates
1460 - 1300	needles

Section 4. Argon Flow Method

4a. Growth of $Sn\ O_2$ from Sn Vapour and O_2

Reed et al (60) showed that $Sn\ O_2$ could be grown at a lower temperature using Sn metal as the starting material. They used a quartz crucible 5 cm diameter x 8 cm long with a 1 cm diameter neck which extended outside the furnace. By heating this crucible containing tin metal for several days, rods up to 3 cm x 5 mm in area were produced. Attempts to reproduce their results were not so successful. The stannic oxide produced fell back into the molten tin. Stannous oxide was formed which reacted with the quartz crucible, forming an orange silicate of tin and destroying the crucible. Only needles were produced.

The method adopted for growing stannic oxide crystals was an argon flow method. By using Sn metal as the starting material, the maximum temperature required was not greater than 1450°C, which meant that a silicon carbide electrical heating element could be used. The furnace arrangements and temperature profile of the furnace are shown in figure 3. The dimensions are given in table 2.2.

5 N tin (from Koch-Light Ltd.) was placed in a re-crystallised alumina tray (30mm x 8mm x 7m), 10cm back from the centre of the furnace. The temperature at this

Figure 2.3: (a) The arrangement of the furnace and (b) its temperature profile, used for growing stannic oxide crystals.

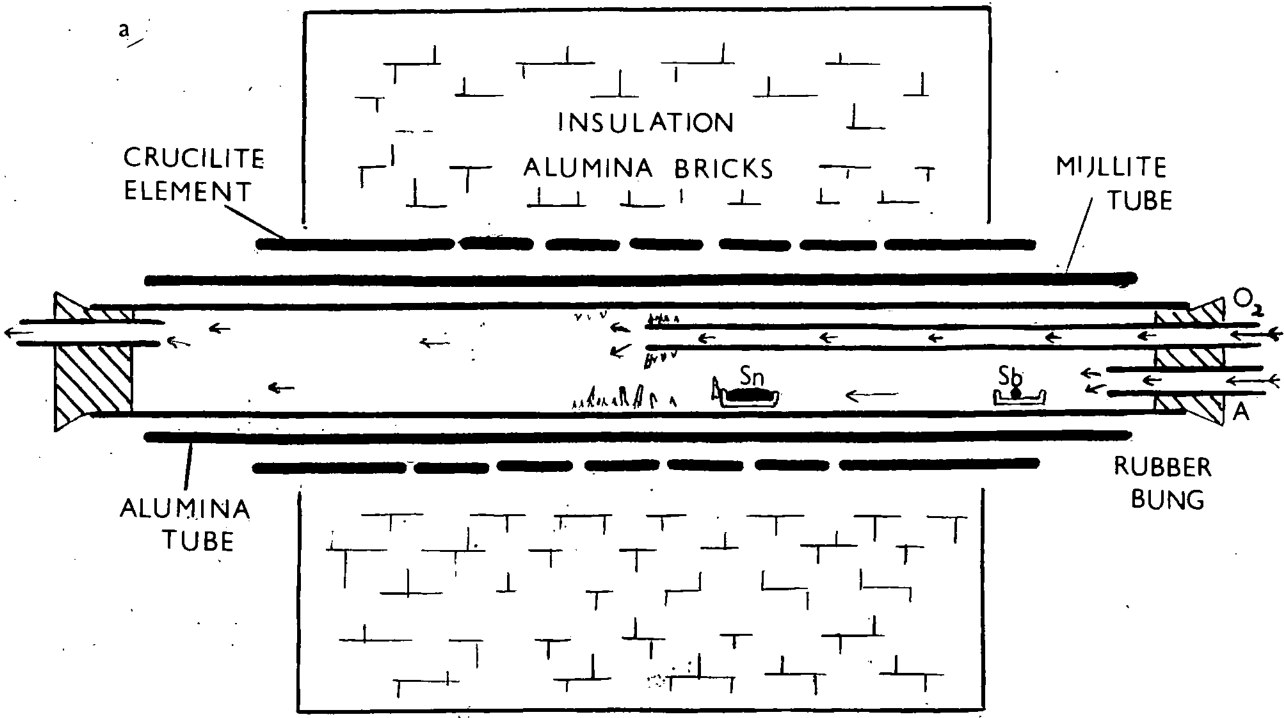

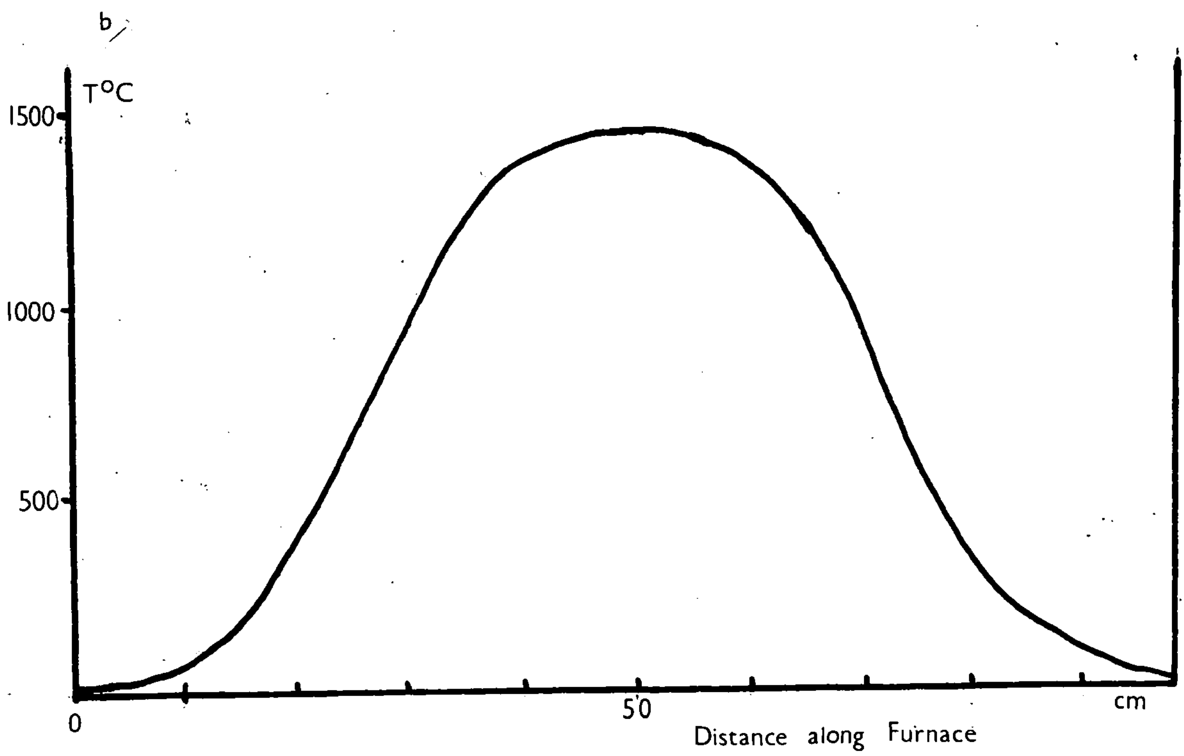

point was 1400° C. If the tray was placed any nearer the oxygen outlet, the surface of the liquid tin became covered with a thick oxide crust.

Table 2.2. Dimensions of Crystal Growing Furnace

Height 32 cm	Width 32 mm		Length 56 mm	
Dimensions of tubes	Crucible element	Alumina tube	Mullite tube	Inner Mullite tubes
length (mm)	650	825	975	600
internal diameter(mm)	54	38	25.5	5
external diameter(mm)	62	46	32	8
hot zone (mm)	300			
resistance(ohms)	2.1			

which effectively prevented further vapourisation. At cooler parts of the furnace the rate of vapourisation was much slower.

The doping agent, usually antimony, was placed in another alumina tray. The position chosen for this tray depended on the degree of doping required, the rate of vapourisation of the dopant and the ease with which it was accepted by the SnO_2 lattice, and so had to be found by experiment.

To prevent back streaming of the oxygen, the oxygen flow rate was adjusted not to exceed 40 cc/min and usually run at 20cc/min. The argon flow was maintained at 100-150 cc/min. Within these limits the quality of crystals did not appear to be affected by small fluctuations in flow rate.

The conditions of initial nucleation of the crystals

were found to be important. The best results were obtained if argon was passed through both tubes in the early period of the warming up of the furnace, and the oxygen flow switched on before the furnace had attained 1450° C (i.e., when the maximum temperature was approximately 1300° C).

4b. Effect of Different Carrier Gases

Although Marley and MacAvoy (58) reported greatest success using helium as the carrier gas (see sect.3c), helium was found to be unsuitable under the conditions of growth described. The only growth obtained was in the form of thin needles, as would be expected from their observations of Table 2.1, since the maximum temperature was only 1450° C. It seems that crystal habit is affected not only by temperature but also by the carrier gas.

Some crystals were grown using nitrogen, but argon gave a slightly smaller yield of slightly larger crystals.

If the oxygen was passed over water, the crystal yield was increased, but crystals so produced were often irregular in form and contained many large voids and other imperfections.

4c. Undoped Crystals - Quenching

If undoped crystals were allowed to cool slowly in the presence of oxygen, they were generally colourless. If they were removed from the furnace immediately, or allowed to cool in an inert atmosphere, they appeared a pale yellowish brown colour. These brown crystals had a higher electrical conductivity and lower activation energy than the colourless crystals (Ch. 3. Sect.1). This is an indication that an oxygen deficiency in the crystals results in one form of donor level. The brown colour of these crystals is due to impurity absorption near the band edge, which extends into the visible blue region of the spectrum (61).

4d. Antimony Doped Crystals

There was no difficulty in doping stannic oxide with antimony. When the pressure of antimony was high, the crystals grew very quickly (3 days) although the only habit was the [001] prismatic form which was usually hollow. The carrier density of these crystals was in the order of 10^{20} cm^{-3} . These crystals were a dark navy blue colour. At lower concentration of antimony, both rods and plates were formed but growth was much slower (10-14 days). These crystals were pale blue and transparent. The best crystals were rods which grew along an a-axis and tended to nucleate on the alumina boat containing the tin.

Miloslavskii (89) showed that the blue colouration is due to the infra red free carrier absorption extending well into the visible region. Figure 2.4(a) shows the transmission spectra of an undoped and an antimony doped ($\sim 10^{19}$ cm^{-3}) crystal.

Table 2.3 shows the carrier density of antimony doped crystals against the temperature of antimony in the furnace.

4e. Chromium Doped Crystals

Chromium trioxide has a very low vapour pressure and to obtain a significant concentration of chromium in the crystals, the boat containing the (Cr_2O_3) was placed in the centre of the furnace. Good crystals of a great variety of habit were formed. These showed a p-type sign of Seebeck voltage and were of high resistivity.

The crystals were red in colour. Figure 2.4b shows the transmission spectrum of a highly doped chromium plate which clearly shows very strong absorption in the green.

Electron spin resonance measurements on one of these crystals is reported in Ch 3. Sect. 4c.

100

50

Transmission %

Undoped

Antimony doped, $n \sim 10^{19}/cc$

Wavelength μ

·4 ·5 ·6 ·7 ·8

Figure 2.4(a): Transmission spectra of an antimony doped plate (230 μ thick) and an undoped plate (380 μ thick)

10

1

$\frac{1}{10}$

Transmission %

Wavelength μ

·4 ·5 ·6 ·7 ·8

Figure 2.4(b): Transmission spectrum of a chromium doped stannic oxide plate (860 μ thick).

Table 2.3.

Carrier density of antimony doped crystals against the temperature of the antimony metal in the furnace.

n. cm.$^{-3}$	Temp ^{o}C of Sb
9 10^{19}	610°
8 10^{18}	470°
5 10^{18}	230°
2 10^{18}	110°

4f. Indium Doped Crystals

Crystals would only grow very slowly in the presence of indium. The crystals produced were badly formed, small and yellow. The sign of their Seebeck voltage indicated that they were p-type but measurement of the electrical conductivity could not differentiate them from undoped samples. The fact that indium had actually gone into the lattice was confirmed by mass spectrographic analysis (Table 2.4).

4g. Gallium Doped Crystals

Attempts to grow gallium doped crystals produced similar results to those for indium doping.

4h. Cerium Doped Crystals

As the oxides of the rare earths are very refractory and thus have a very low vapour pressure, cerium chloride was used in an attempt to dope stannic oxide with cerium. Small irregular crystals were grown. These showed no distinctive luminescence and it is not known whether any cerium was accepted by the lattice. The large ionic radius of cerium (1·01Å) (36) indicates that it is very probable that it would not be accepted.

Section 5. Mass Spectrographic Analysis

Samples of tin oxide crystals from seven different

runs were powdered and despatched in tin foil to British Titan Products Co. Ltd., who kindly performed a mass spectrographic analysis of them. Their findings are shown in Table 2.4.

Samples 1 - 3 were undoped samples from different runs. Samples 4 and 5 were antimony doped, from the runs which produced specimens 1 and 2 used for electrical measurements (see Chapter 3, Sect. 2 & 3). Samples 6 and 7 were respectively chromium and indium doped.

Since it was suspected that some of the impurities present were introduced in the powdering operation, samples of powder and of single crystals were despatched to the Chemical Inspectorate, Royal Arsenal, Woolwich. There, the crystals were powdered by shaking in a plastic tube with plastic balls, so that no metallic impurities would be introduced. The results in Table 2.5 show that the crystals are of higher purity than first expected. It is surprising that these results show not only a low content of unexpected impurities (Ga, In, Te) but also of silicon and aluminium, which were expected, as both elements are to be found in the ceramic mullite tube in which the crystals were grown.

It is seen in Chapter 3, Sect. 3 that specimens 1 and 2 contain $8.8.10^{19}$ and $8.2.10^{18}$ carriers per cc. respectively. If we assume that one donor electron is introduced for each antimony atom, this corresponds to 0.3% and 0·03% Sb by weight in these crystals. The results of the mass spectrographic analysis give 0·2% and 0·04%. As these results are quoted with an error margin of a factor of 3, they are not in disagreement with the observations Lyashenko and Miloslavskii (62) who found that for thin films, one donor electron is produced for each antimony atom in the lattice.

Table 2.4.

Mass Spectrographic Analysis of Tin Oxide Samples performed by British Titan Products Co. Ltd.

Results quoted as p.p.m. by weight, subject to error of a factor of 3. (i.e. 300 p.m. represents a range from 900 p.p.m. to 100 p.p.m.

	samples						
Element	1	2	3	4	5	6	7
Sodium	150	500	150	15	150	150	150
Aluminium	1000	1000	500	100	100	100	100
Silicon	1000	3000	1000	250	1000	1000	1000
Potassium	100	300	100	300	100	100	100
Vanadium	10	30	10	3	30	10	10
Chromium	<30	<30	<30	<30	<30	85	<30
Iron	300	500	100	300	1000	300	300
Copper	60	<5	<5	10	10	<5	<5
Indium	<10	<10	<10	<10	<10	<10	200
Antimony	50	<10	<10	2000	400	100	<10
Mercury	10	5	<5	<5	30	<5	<5
Lead	10	10	<10	<10	10	<10	<10
Zirconium	50	50	50	50	50	50	50

All other impurities not detected i.e. 10 p.p.m.

see Chapter 2. Section 6(c)

Table 2.5

Mass Spectrographic Analysis of Tin Oxide performed by the Chemical Inspectorate, Royal Arsenal, Woolwich.

p.p.m. detected

Element	Crystals	Powder
Sodium	trace <5	trace <5
Calcium	5	10
Aluminium	20	200
Magnesium	trace <5	trace <5
Silicon	trace <20	300
Iron	trace <50	50
Gallium	n.d. <20	30
Mercury	n.d. <50	200
Tellurium	trace? <50	150

n.d. = not detected

Accuracy quoted as within a factor of 2.

Section 6. Crystal Habit

6a. Introduction

There were four common habits of stannic oxide crystals produced by the argon flow method. Rods which grew parallel to the c-axis usually formed on the end of the oxygen tube (see figure 2.5) and plates grew on either side of this region. Rods which grew parallel to the a-axis were formed actually on the alumina tray containing the tin. Figure 2.6 shows some of the various crystal forms, produced from several runs.

6b. Twinned Plates (Habit 1)

These diamond shaped plates (figure 2.7a) were the most common habit. They occurred in all runs, except those producing very heavily antimony doped crystals. The

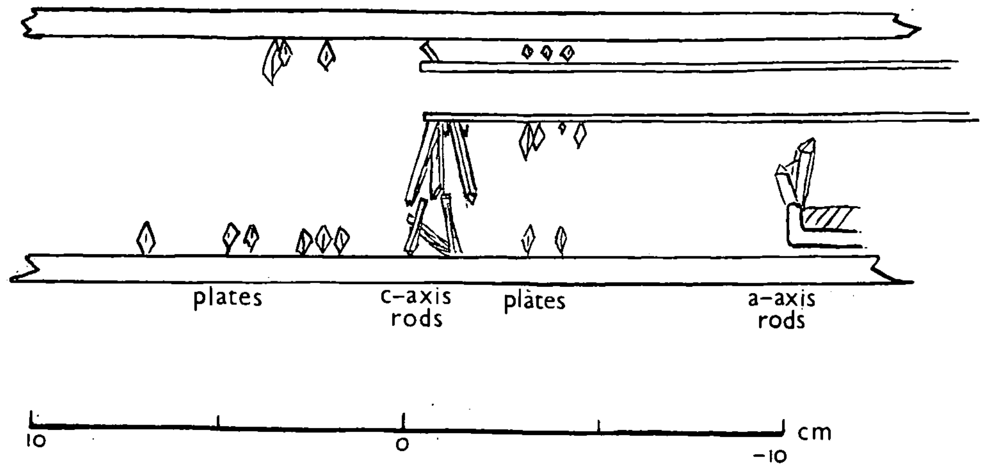

Figure 2.5: Position of growth of the chief crystal habits.

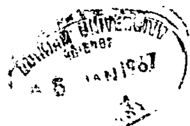

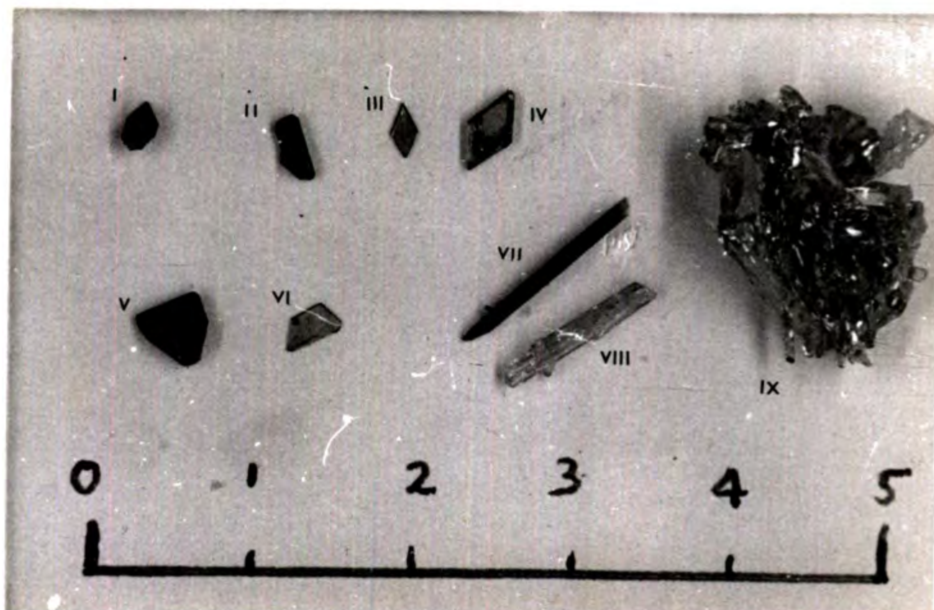

Scale in cms

Figure 2.6

Various crystal habits

i Chromium doped rhombohedron see figure 2.10c

ii Chromium doped a-axis rod see figure 2.12a

iii and iv Typical twinned plates see figure 2.7a

v Crystal of habit 3 see figure 2.12b

vi Chromium doped trapezoidal plate see figure 2.7b

vii and viii Typical c-axis rods see figure 2.10a and b

ix Crystalline mass produced by argon flow method.

HABIT I

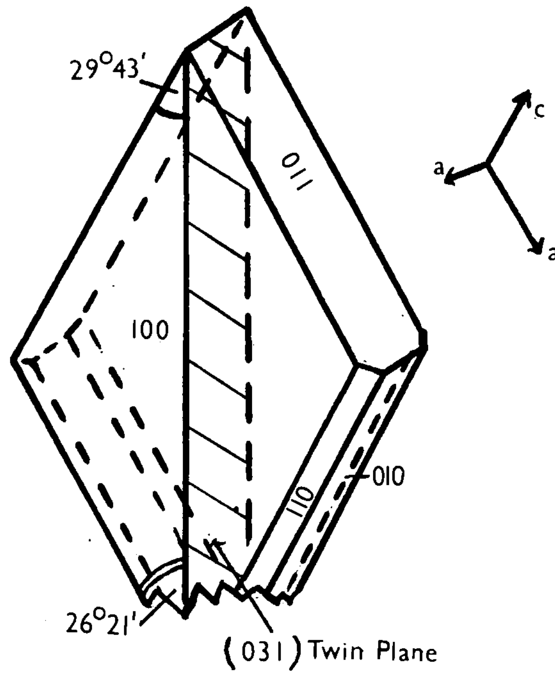

Figure 2.7(a):
Twinned plate, showing (031) twin plane

Figure 2.7(b):
Trapezoidal plate produced in some chromium doped runs. (see figure 2.6 (vi)).

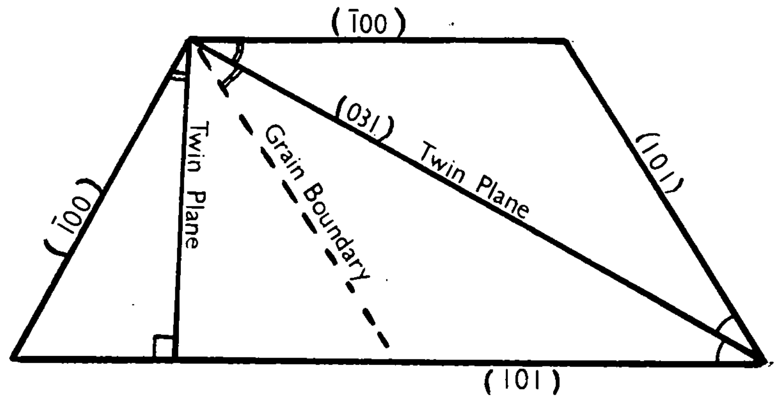

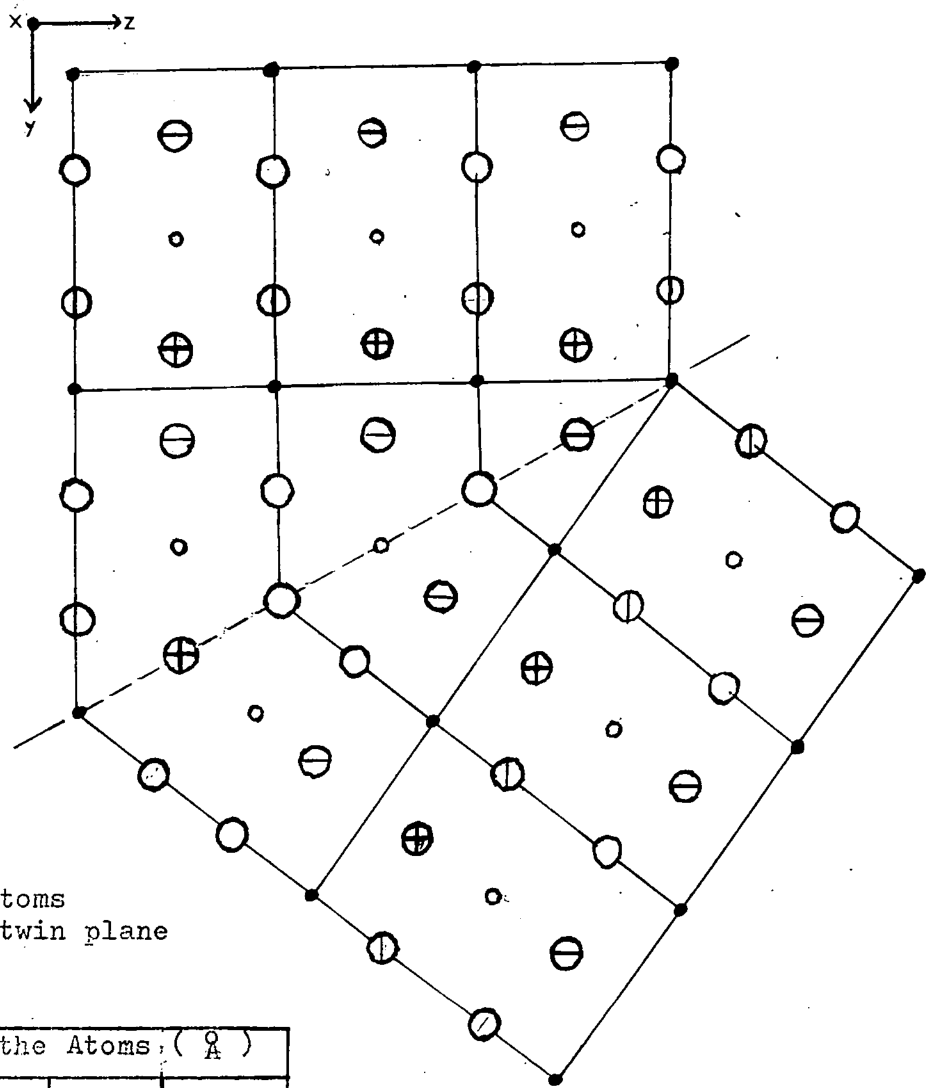

Figure 2.8:
Arrangement of atoms
along the (031) twin plane

Co-ordinates of the Atoms (Å)				
Sn	0.00	0.00	0.00	●
	2.37	2.37	1.60	∘
O	1.45	1.45	0.00	○
	3.28	3.28	0.00	⦶
	3.82	0.92	1.60	⊖
	0.92	3.82	1.60	⊕
a = 4.74		c = 3.20		

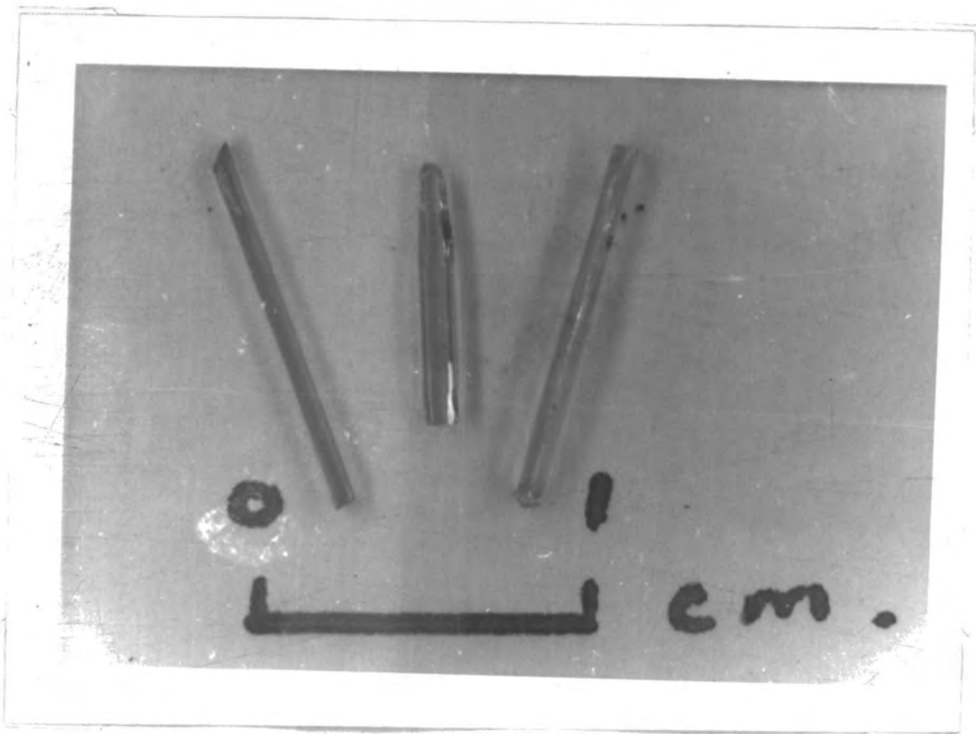

Figure 2.9a: Typical c-axis rods

Figure 2.9b: c-axis rods showing end voids

HABIT 2

Figure 2.10(a):

c-axis rod ([001] prism) showing end faces observed on an S_b doped crystal.

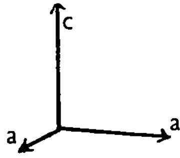

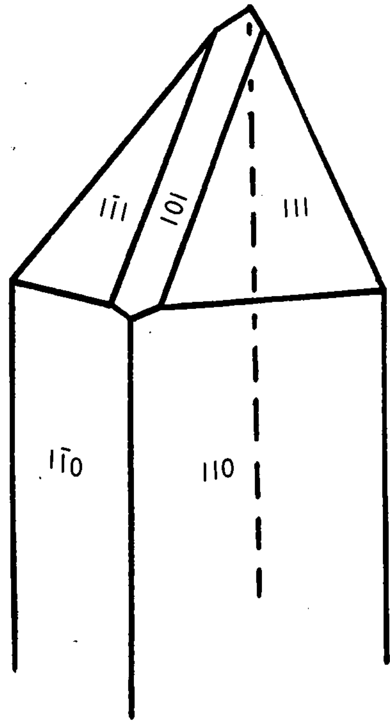

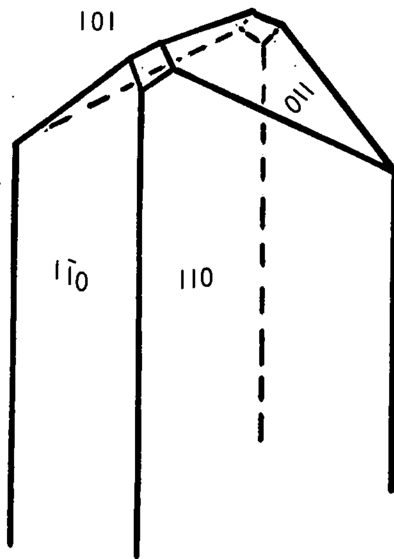

Figure 2.10(b):
c-axis rod showing faces observed on an undoped crystal.

Figure 2.10(c):
Rhombohedral crystal (see figure 2.6(i)).

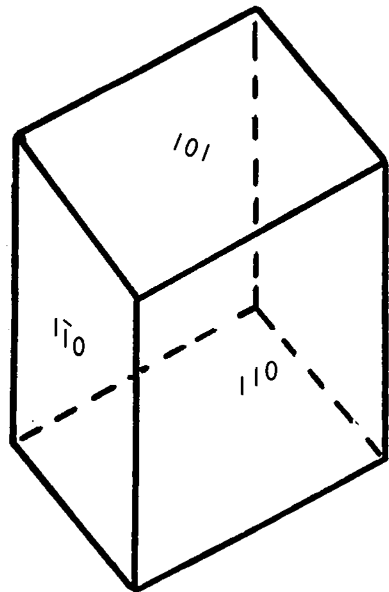

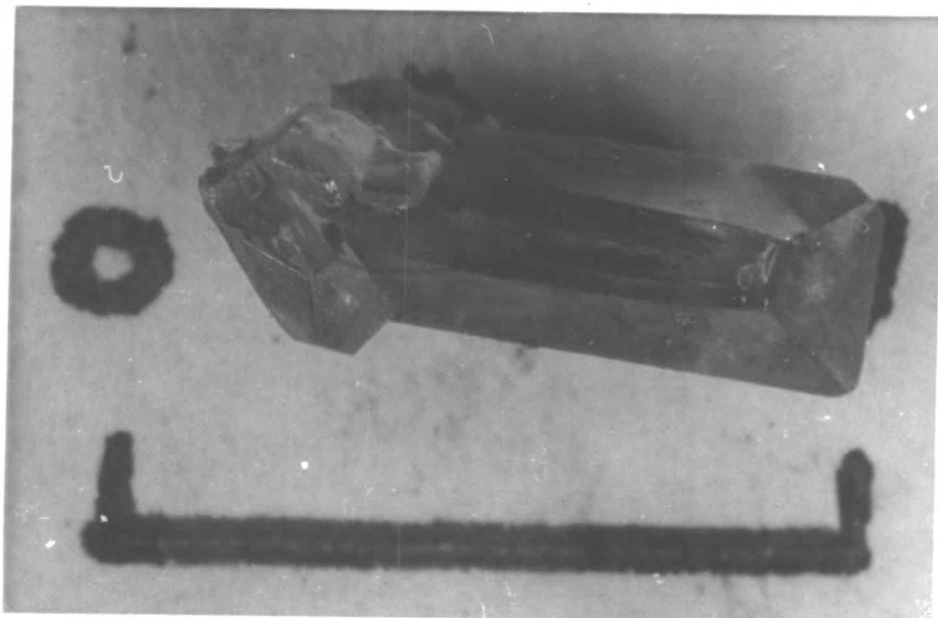

Figure 2.11a: a-axis rod used for specimen 3

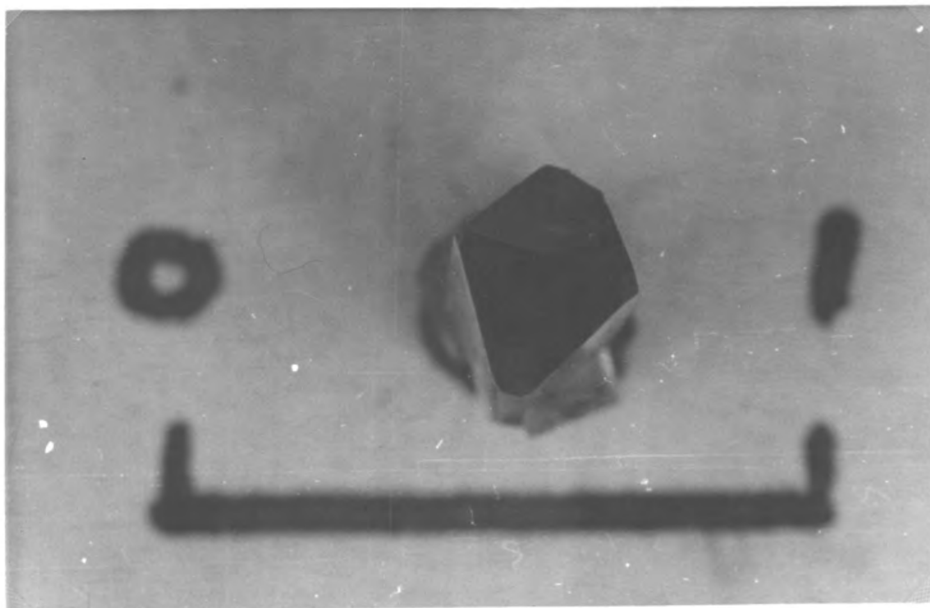

Figure 2.11b: End view of same crystal

Scale in cms

HABIT 3

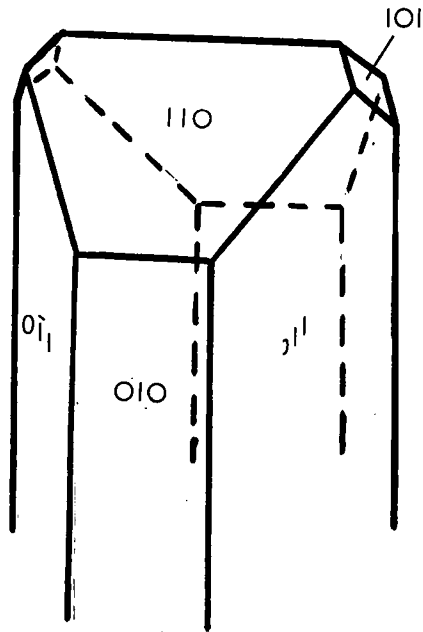

Figure 2.12(a):
Usual form of a-axis rod ([100] prism)

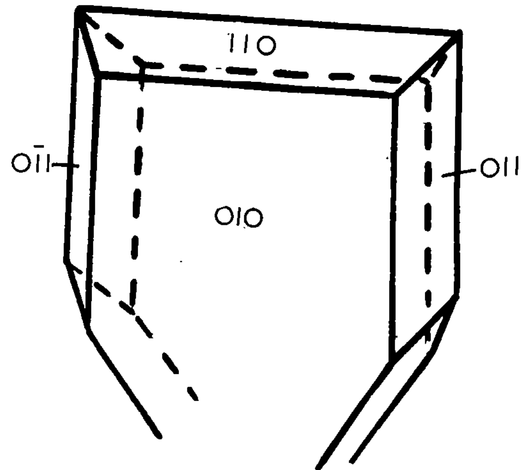

Figure 2.12(b):
Common type of plate which is similar in form to the above crystal.

HABIT 4

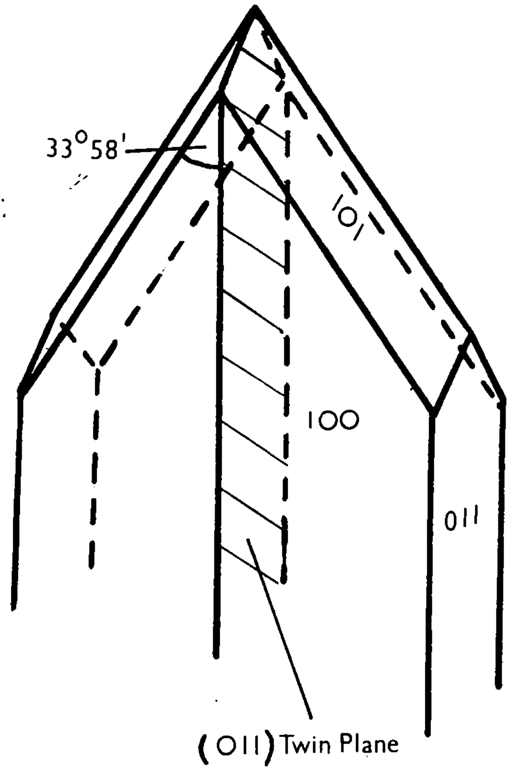

Figure 2.13(a)
Crystal twinned along (011) plane. Commonly found with chromium doped crystals.

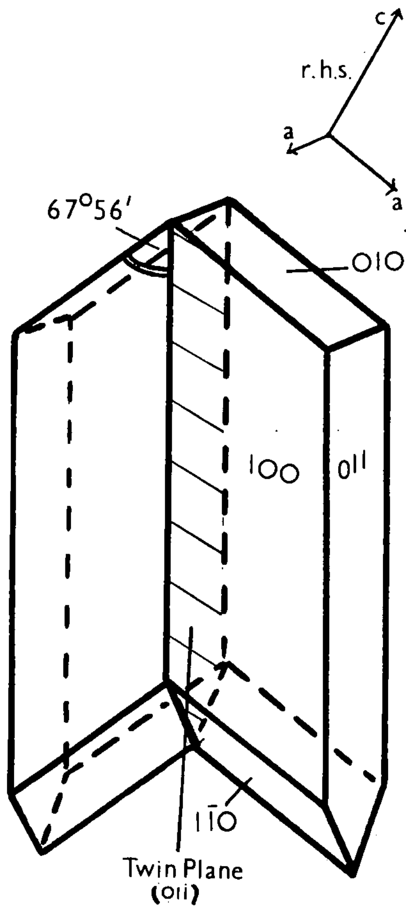

Figure 2.13(b)
Another form of crystal twinned along (011) plane.

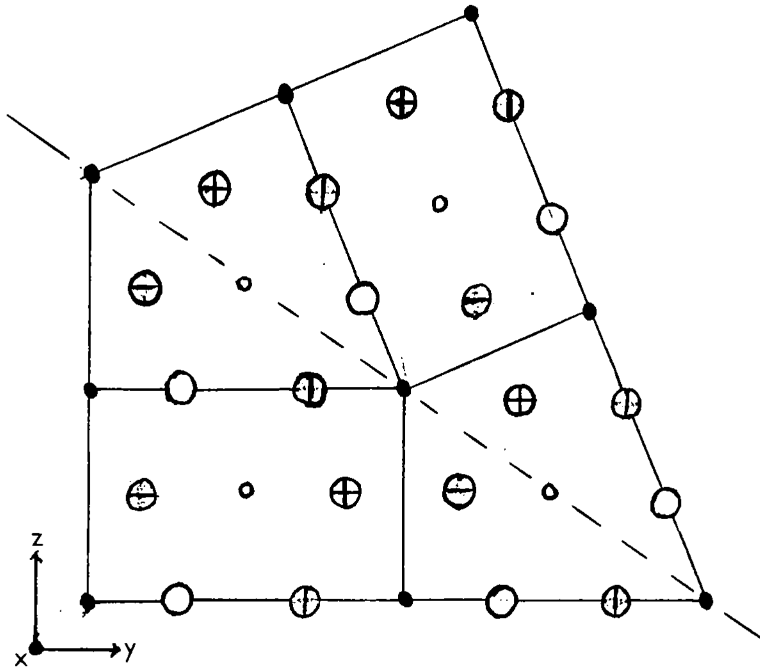

Figure 2.14: Arrangement of atoms along the (011) twin plane. Symbols are the same as for figure 2.8.

faces on these crystals, as grown, were often of optical quality, especially on the thinner crystals. Back reflection Laue photographs were used to orientate the crystals. The twin plane was found to be the (031) plane. The arrangement of atoms at the twin plane is shown in figure 2.8. (45).

6c. {001} Prisms (Habit 2)

Most rods did grow along the c-axis. If growth was too rapid the rods were hollow through the centre. On most crystals, there was a large void at the growing end (figure 2.9b). As there were no faces on the base of the crystals which were attached to the mullite tube during growth, end faces were often non existent. Figure 2.10shows some typical rods of this type. The rhombohedral shape (figure 2.10c and figure 2.6(i)) grew only in chromium doping runs.

6d. {100} Prisms (Habit 3)

Only a few crystals of this type were produced. The best sample, illustrated in figures 2.11 (a) and (b), was used as specimen 3 in the electrical measurements. A photograph of the cut form with holes drilled for thermocouples is shown in figure (0.1A). The plate form of this habit (figure 2.12(b) and 2.6(v)) often occurred in chromium doped runs but also appeared in undoped and antimony doped runs. Specimen 4 was a long thin plate of this type whose {011} and {110} faces were not well defined. It was an ideal shape for Hall measurements.

6a. Rods Twinned along the (011) Plane (Habit 4)

These rods usually only occurred in chromium doping runs, and crystals of both forms illustrated in figure 2.13 were observed. One crystal lightly doped with

antimony grew as a twinned rod in a [011] direction. This is illustrated on figure 0.1B. Figure 2.14 shows the arrangement of atoms along the (011) twin plane.

Section 7. Crystallographic Data

7a. Introduction

Stannic oxide occurs naturally as the mineral cassiterite. Its structure is similar to that of rutile $Ti\ O_2$), (see figure 2.15a) and is of the tetragonal system, class $4/_m\ 2/_m\ 2/_m$. The lattice parameters, as measured by various workers, are shown in table 2.6. There are two formula units per unit cell. The Sn atoms are found at sites 0, 0, 0; and $\frac{1}{2}$, $\frac{1}{2}$, $\frac{1}{2}$; and 0 atoms at sites x, x, 0; $\bar{x}$, $\bar{x}$, 0; $\frac{1}{2}$ - x, $\frac{1}{2}$ - x, $\frac{1}{2}$; and $\frac{1}{2}$ - x, $\frac{1}{2}$ + x, $\frac{1}{2}$, where x = 0.307. All Sn - 0 distances are the same (2.055A) within experimental error.

Each Sn atom may be considered to be at the centre of 6 oxygen atoms situated at the corners of a slightly distorted octahedron. There are two equivalent sites. The $\frac{1}{2}$, $\frac{1}{2}$, $\frac{1}{2}$, site is similar to the 0,0,0, site but rotated about the c axis through 90°, (see figure 2.15(b)).

From Andresen (24) according to Dana (65) natural cassiterite crystals are prismatic [001] in habit, with prominent faces {110} and {100} . These prisms are frequently terminated by the pyramids {101} and {111} (cf section 9). Natural twins are usually twinned along the (011) plane but Bourgeois (66) reported twinning along the (031) plane as found in the diamond shaped plates (habit 1).

7b. Powder Diffraction Photographs

Photographs of doped and undoped $Sn\ O_2$ were taken using a Debye-Scherrer camera of 11.46 in diameter. To

Figure 2.15(a): Rutile structure unit cell.

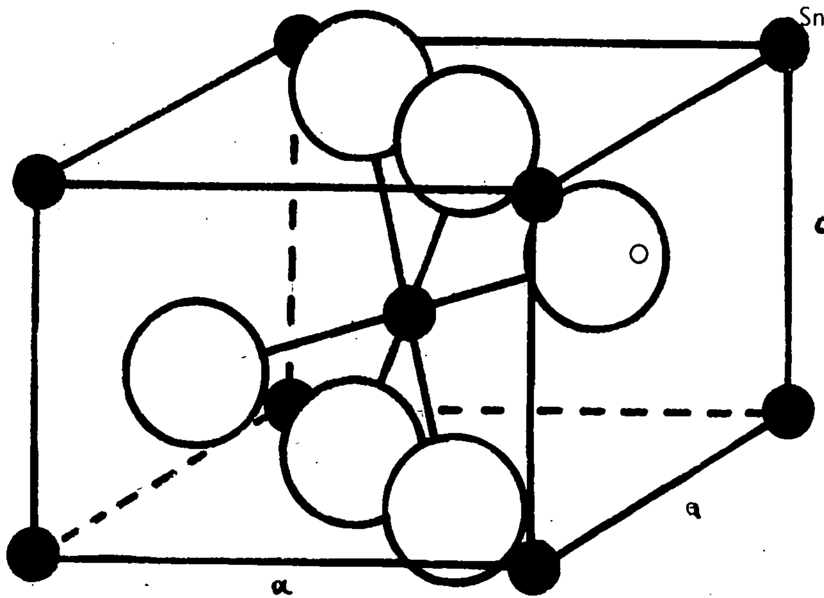

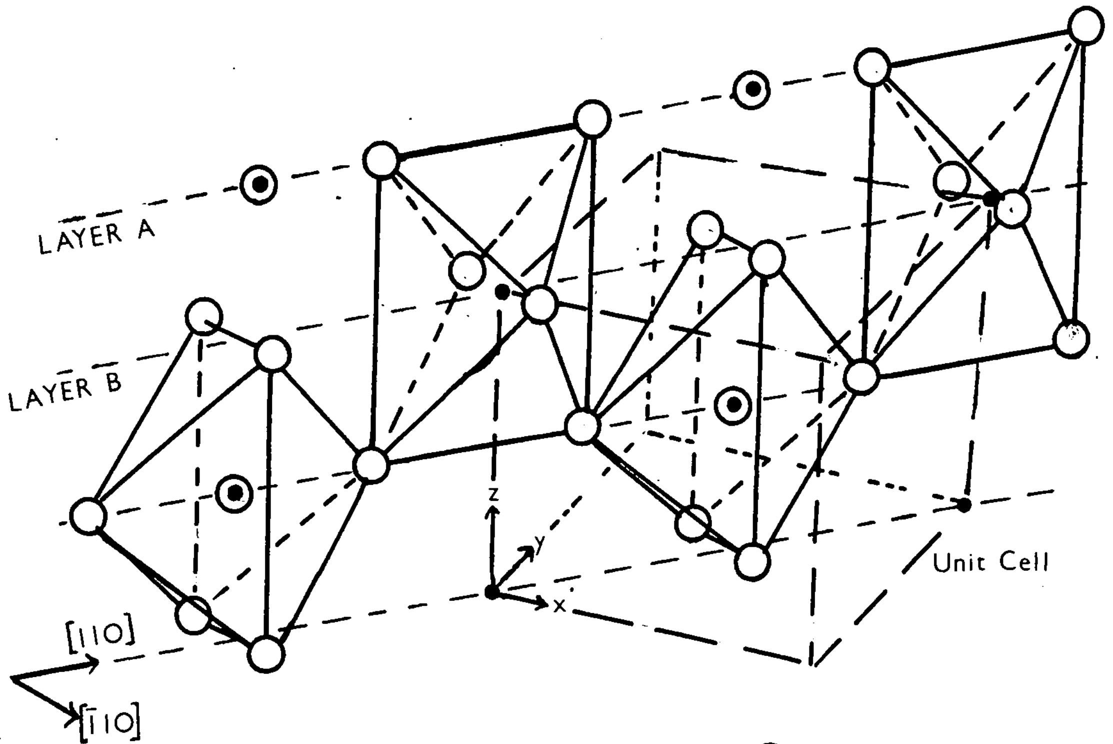

Figure 2.15(b): Rutile structure showing two equivalent sites for Sn atoms. (after Andresen (64)).

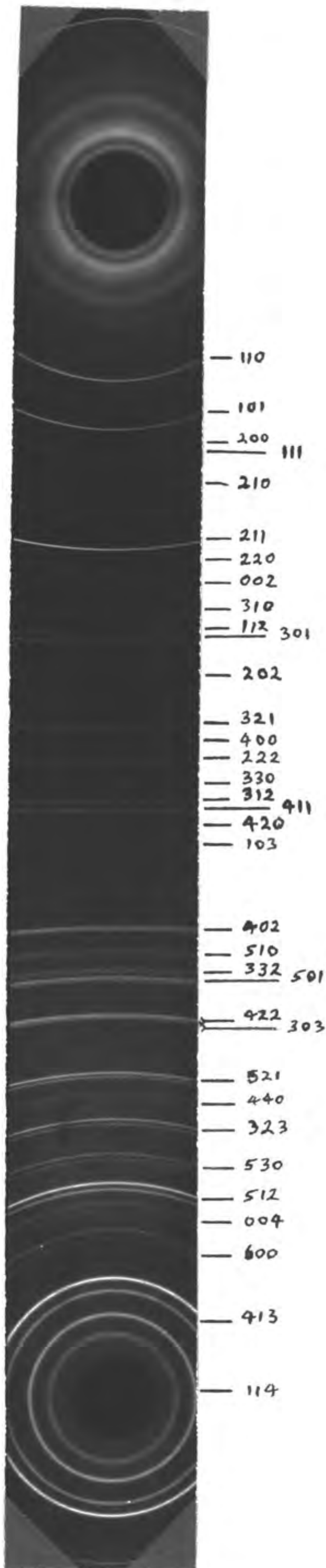

Figure 2.16a: Powder diffraction photograph lines indexed.

Figures 2.17(a) and 2.17(b): Nelson-Riley plots of powder diffraction photograph results for high angle lines.

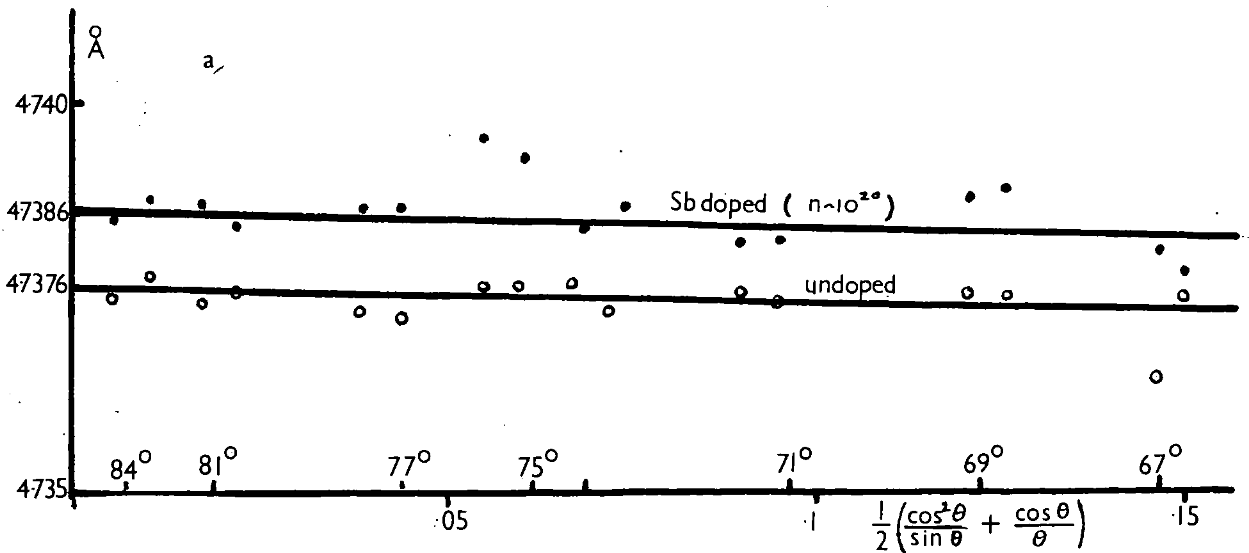

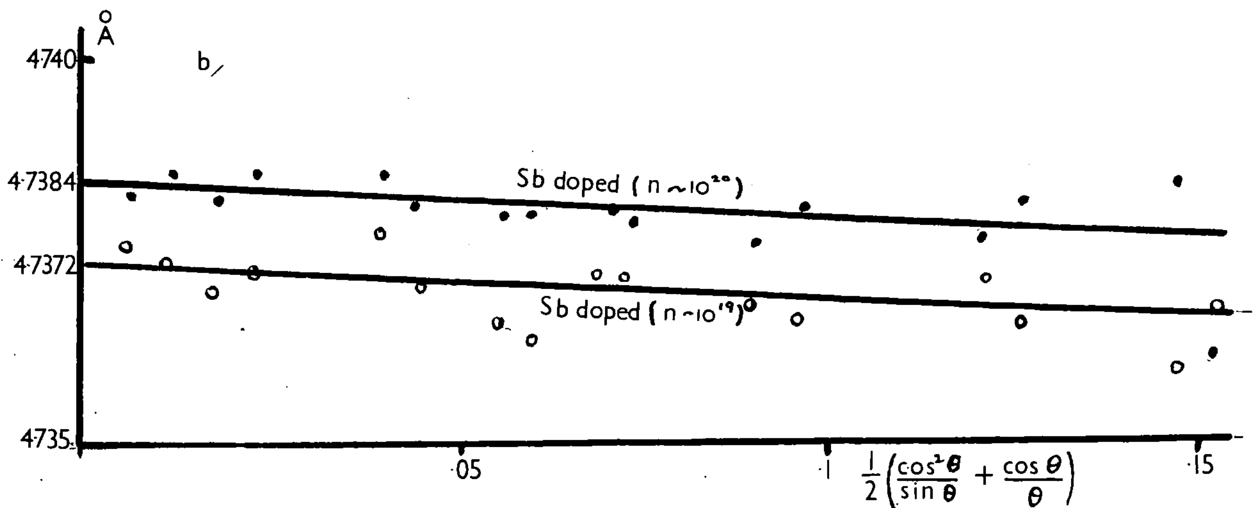

allow for systematic errors of the equipment, the same camera, and same beam from the X-ray generator were used for each set of exposures. Copper K_{α} radiation was used.

The diffraction photograph obtained from SnO_2 powder fortunately contains several high angle lines (see figure 2.16) which means that accurate determination of the crystal parameters is not too difficult.

The high angle lines were indexed using the relationship

$$\sin^2\theta = \left(\frac{\lambda}{2a}\right)^2 \left[h^2 + k^2 + \left(\frac{a}{c}\right)^2 l^2\right] , \qquad (2.5)$$

where the values of a and c were obtained from Baur (67).

The lines were measured to the nearest .005 cm on a vernier film measurer. Corrections were made for film shrinkage by obtaining the average measured position of the centres for both the high and low angle lines. The d values were obtained from published charts (68) of the relationship

$$d = \frac{\lambda}{2\sin\theta} \qquad (2.6)$$

for the copper K_{α_1} and K_{α_2} lines.

The value of a was obtained from the relationship:

$$a = d\sqrt{h^2 + k^2 + \left(\frac{a}{c}\right)^2 l^2} \qquad (2.7)$$

The value of $\frac{a}{c}$ was chosen to give the best agreement of a_0 for lines with zero and high 'l' indices.

Errors due to different sizes of specimen and absorption of the specimen were minimised by plotting the value of a on a Nelson-Riley plot (69). The results of two different comparisons are shown in figures 2.17a and 2.17b.

These results show that there is a probable increase in the lattice parameters of 0.02% between the undoped crystals and those highly doped ($n \sim 10^{20}\,cm^{-3}$) with antimony. The coefficient of linear expansion of ceramic stannic

oxide is in the order of 10^{-5}, so although the temperature was not controlled during exposures temperature variation of 20° C would be necessary to explain the difference. Klug and Alexander (70) show that the accuracy of measurements at 70° is 0.015%, the consistency of points on figures 2.17a and 2.17b indicate a greater relative accuracy.

The calculated ionic radius for Sn^{4+} is 0.71Å and for Sb^{5+} it is 0.62Å (36), so a direct substitution of antimony in a tin lattice site is in itself unlikely to cause an increase in the lattice parameter. The O^{--} ion has a radius of 1.40Å (36). The distance between each Sn and O atom is only 2.05Å so oxygen ions are unlikely to find an interstitial position. The simplest explanation for the increase in lattice parameter is that in the highly doped crystal there is a certain number of interstitial antimony ions which dilate the lattice slightly.

It can be seen that no difference in lattice parameter could be detected between undoped material and more lightly antimony doped ($n \sim 10^{19} cm^{-3}$) material.

A Debye-Scherrer photograph of chromium doped $Sn\,O_2$ gave lattice parameters of a = 4.737 and c = 3.186, identical with the undoped material. Since no measurement of the chromium content was available, a more accurate determination was not made.

Table 2.6 gives the lattice parameters of $Sn\,O_2$ according to the various workers.

Figure 2.18a

Back reflection Laue photograph of $Sn\ O_2$ taken in the [001] direction.

Figure 2.18b

Back reflection Laue photograph of SnO_2 taken in the [100] direction.

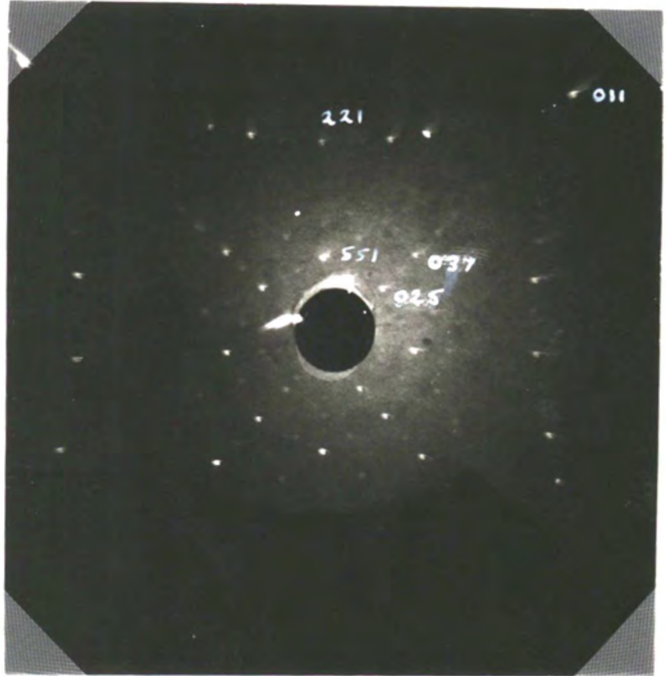
221
011
551
037
025

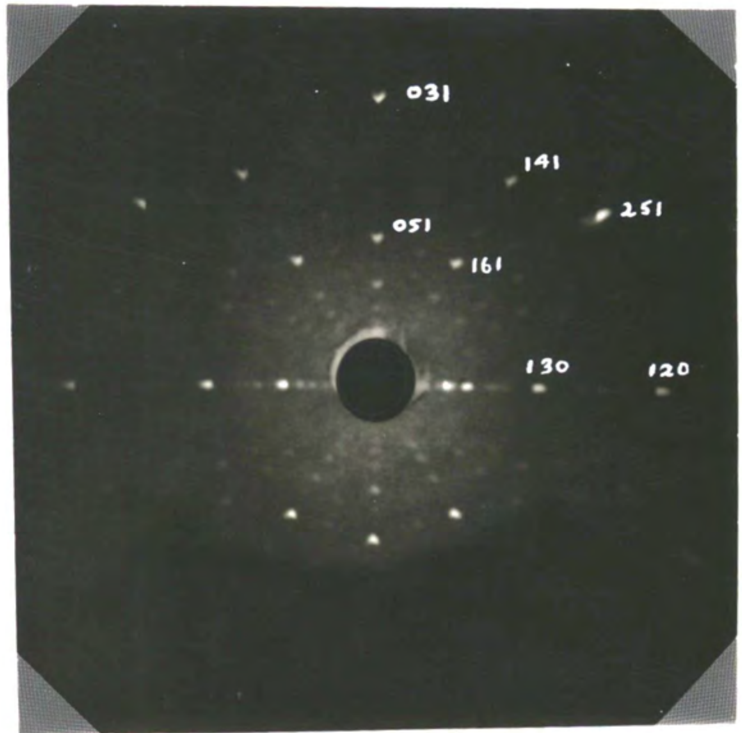
031
141
251
051
161
130
120

Table 2.6

The lattice parameters of $Sn\ O_2$ according to various workers -

a	c	c/a	references
4.738	3.188	0.673	Swanson and Tatge (71)
4.737	3.185	0.672	Baur (67)
4.7372	3.18638	0.6726	Schröke (72)
4.738	3.187	0.6726	Present work

7c. Back Reflection Laue Photographs

Back reflection Laue photographs were used to discover the orientation of the crystals. The photographs taken, with the crystal 3 cm away from the photographic plate, both in the [001] and [100] direction, are shown in figures 2.18a and 2.18b. The chief reflections are indexed.

7d. Etch Pits

A study of etch pits was made on various types of crystal using the technique of Koffyberg (59). He showed that etch pits could be formed by using a boiling solution of 47% hydriodic acid (HI), with a small quantity of hypophosphorous acid (H_3PO_2) added to remove excess iodine, and also that each pit corresponded to a point where a dislocation line intersected the crystal surface.

On faces of the form {110} rectangular shallow pits were formed after an etching time of 10 minutes. On faces of the form {011} wedge shaped pits were formed. These usually required an etching time of 30 minutes.

Figure 2.19 shows a {110} etched face of a crystal. This photograph clearly shows the etch pit shapes and

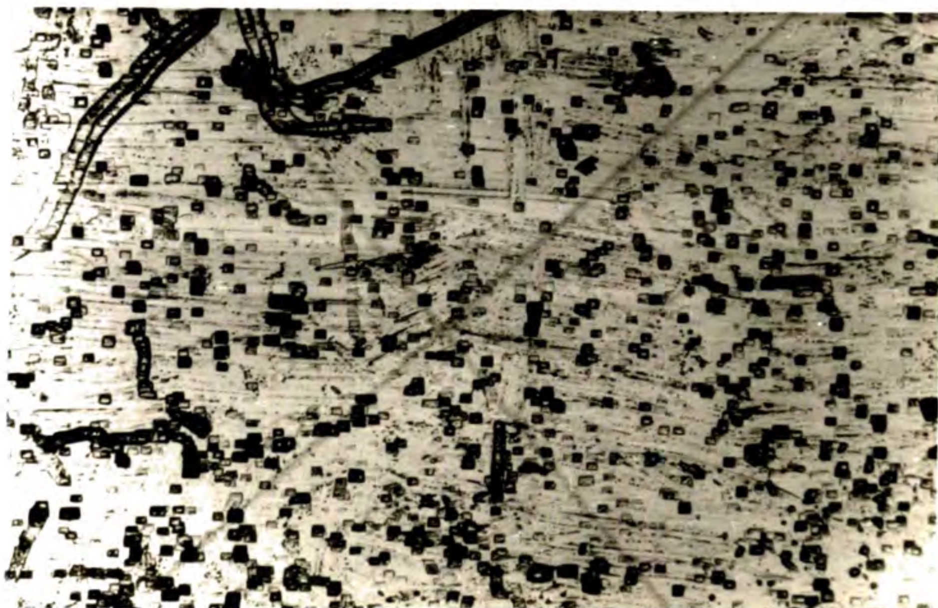

Figure 2.19

Typical (110) face of c-axis rod after a 10 minute etch in HI.

Scale

mm

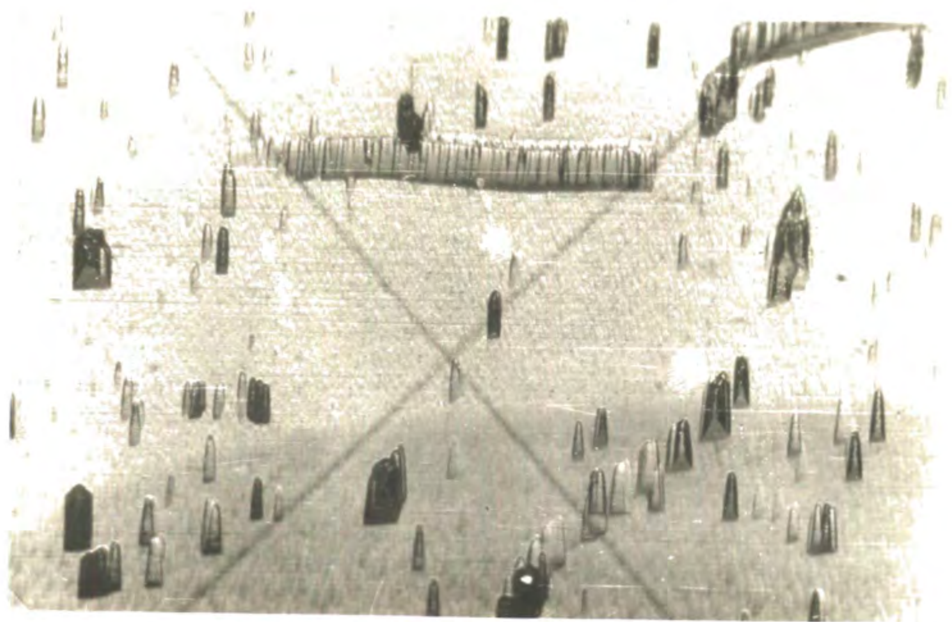

also lines of pits along polygon walls. All c-axis rods examined by this method had a similar average dislocation density ($1\text{-}2.10^5$ cm^{-2}), although large variations were found between different areas. In general the density of pits was greater in the 1 or 2 mm length nearest the end of the crystal that was attached to the mullite tube during growth.

Figure 2.20a shows the wedge shaped pits formed on a $\{011\}$ face after a 30 minute etch. The crystal was specimen 3 (see Chapter 3) an a-axis rod. It had a dislocation density which varied from 8.10^4, near the base, to 2.10^4 cm^{-2}, near the face end. Figure 2.20b shows the $\{110\}$ face of the same crystal showing the rectangular pits as expected. The etch pit density was again 2.10^4 cm^{-2} on this face.

$\{100\}$ faces did not appear to be etched by this method, so only the edge faces of the twinned plates were etched. These also had an etch pit density in the order of 10^5 cm^{-2}.

CHAPTER III

EXPERIMENTAL METHODS AND RESULTS

Section 1. Introduction

Since it was not found possible to grow stannic oxide crystals that were large enough for thermal conductivity experiments, it was decided to measure the product $\alpha^2\sigma$ which appears in the expression for the thermoelectric figure of merit (see Ch.1.,Sect.4e). The chief interest was in the high temperature behaviour of the material.

To obtain a full appraisal of any solid for thermoelectric applications, it is necessary to investigate its more fundamental properties, namely those parameters which occur in equation 1.86. Once these are known the optimum doping level can be calculated. Materials for use in thermoelectric devices usually have high carrier densities ($\sim 10^{19}$ cm^{-3}), so antimony doped specimens with carrier densities in the range 2.10^{18} - 9.10^{19} cm^{-3} were studied. The Seebeck effect was measured between room temperature and 1000° C and a measurement was also made on some crystals at near liquid nitrogen temperature. The electrical conductivity was measured between liquid nitrogen temperature 77°K and 1200°K, and the Hall effect between 77°K and 600°K.

A small amount of work was also done to measure the electrical conductivity of the undoped crystals and crystals doped with chromium and indium.

The final section of the chapter deals with various other experiments performed on the crystals.

Section 2. Electrical Conductivity at High Temperatures

2a. Two-Probe Method

For specimens of high resistivity a two-probe method

of measurement was used. Contacts were made to the ends of stannic oxide rods (habit 2) using a preparation of platinum paste (Johnson and Matthey type T 177). The crystal was held in position by the platinum wires that formed the electrical leads to the specimen. A small quantity of paste was applied to each end of the crystal. The paste then had to be fired by heating slowly up to 600° C. The contacts produced by this method were mechanically very strong and made more satisfactory electrical contact than any other type used at high temperatures. During measurement runs, the contacts were frequently checked to see that Ohm's Law was obeyed. If not, an 0.1μF condenser was charged to 400 V, using H.T. batteries, and discharged across the contacts (see reference 73). After a few such discharges ohmic behaviour was restored. This treatment did not appear to affect the crystal bulk at all. Contacts formed by this method usually deteriorated with time and change of temperature, and so the process had to be repeated at intervals.

Honig et al (74) made contacts by dipping the crystals into molten silver. This method was used at the beginning of the work. The contacts behaved reliably at high temperatures but below 500°C a sudden break in contact occurred. This failure is believed to have been due to the difference in thermal expansion between silver and stannic oxide. The mechanical strain caused by dipping the crystals into the molten silver often made the crystals very brittle.

'Silver Dag', a colloidal suspersion of silver in an

organic solvent (M.I.B.K.) that is marketed by Acheson Colloids Ltd., was also used to make contacts in the early stages of this research. It had the advantage that it dried quickly to form a mechanically stable contact and required no further heat treatment. Unfortunately electrical stability was difficult to achieve for conductivity measurements. Spark formation of the contacts could improve the stability for short periods but in general, for a steady applied voltage, the current would wander over a range of values that could differ by a factor of 10.

At high temperatures, the conductivity of the undoped specimens was low enough for four-probe measurements to be made. These were found to agree with the two-probe results within reasonable experimental error (see figure 3.2).

2b. Four-Probe Method

A photograph of the apparatus constructed for measuring the electrical conductivity of stannic oxide by a four-probe method at high temperatures is shown in figure 3.1a. Figure 3.1b shows the circuit arrangement. The principles of this apparatus were originally described by Marley and McAvoy (45). The method of construction was as follows:-

(i) A silica plate, $2\frac{1}{2}$" x $\frac{3}{4}$" in area and 2 mm thick, was taken and small slots cut into the edge of both the long sides. These acted as anchor points for the thermocouple and current carrying leads. The plate was then fused to the end of the six bore capillary tube of 6.5 mm diameter.

(ii) Two pieces of silica tubing of 0.5m bore and 0.5mm

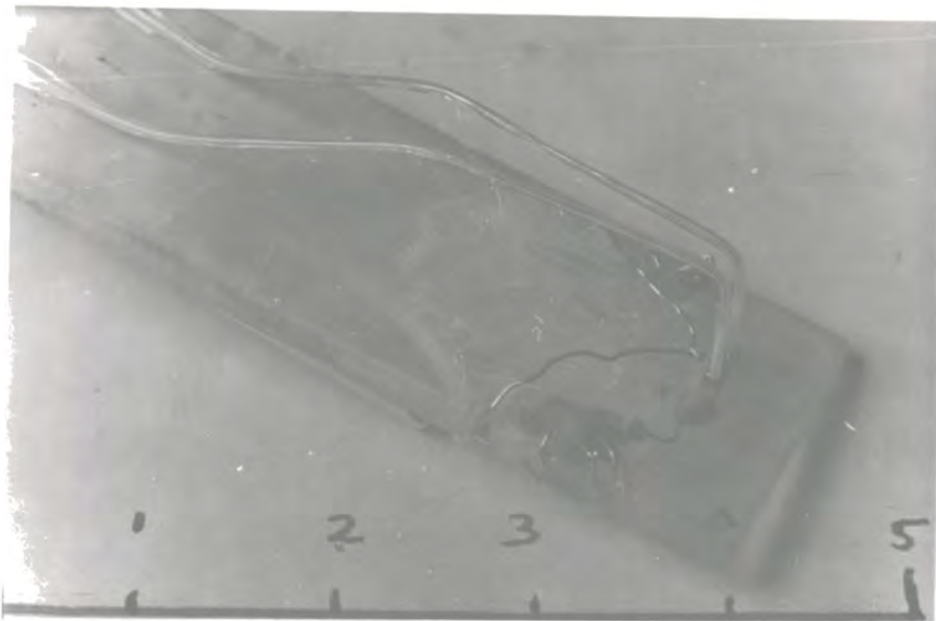

Scale in cms

Figure 3.1(a): High temperature holder for four probe conductivity measurement.
Figure 3.1(b): Circuit for four probe conductivity measurements.

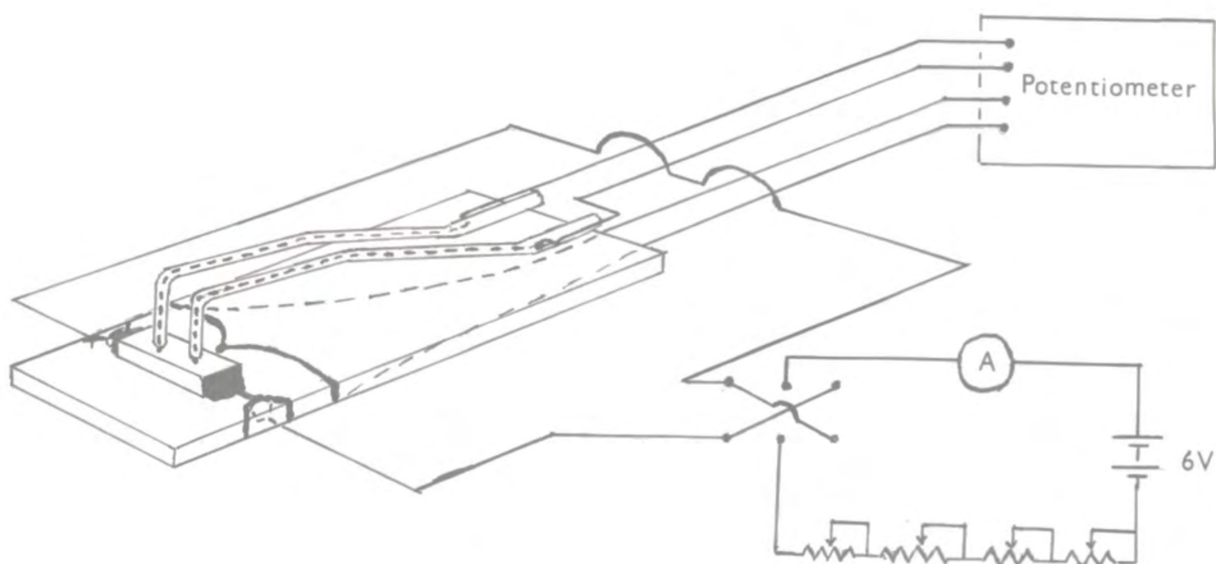

25 JAN 1967
LIBRARY

wall thickness were sealed at one end. A small hole was blown in each tube at approximately $\frac{3}{4}$" from this end. Beyond this hole the tubes were drawn out evenly until their external diameters were 0.5mm for a length of 2" and then cut.

(iii) The fine capillary bores thus produced were threaded with 0.05 mm diameter platinum wire by means of the hole blown near their thick ends. The ends of the wire, that emerged through the open ends of the fine bores, were melted so that small round beads were produced. These prevented the wires from being drawn back inside the tubes and provided the surface that was to make electrical contact with the crystal.

(iv) The thick ends of the capillary tubes were fused to the silica plate near the six bore tubing. The tubes were then shaped as shown in the photograph (figure 3.1a). A cool flame was necessary to prevent the melting of the platinum wires at their centres. These shaped, platinum threaded, capillary bores provided the voltage probes to the specimen.

(v) Platinum wire leads, 0.25mm diameter, were threaded through four of the bores in the six bore capillary tube. Two of these were fused to the voltage probe wires, and two were anchored to the side slots in the plate. A thermocouple of Pt/Pt 13% Rh was constructed so that its junction would rest near the specimen. This occupied the remaining two bores of the six bore tube.

(vi) The voltage probes were flexible enough to allow the leads to be spring loaded on to the sample. The current contacts were made by applying platinum paste, which had to be fired on.

This apparatus was successfully used in air up to 1000°C, although long periods at this temperature caused recrystallisation of the surface of the silica. This made the fragile voltage probe capillary tubes very brittle.

Some difficulty was experienced in obtaining low resistance contacts between the voltage probes and the specimen. Spark discharge through the contacts, as described in section 2a, was often successful. A very reliable contact was made if a layer of indium was evaporated on the surface of the crystal under these contacts.

The external circuitry meant that the highest resistance that could be reasonably measured was about $10^3 \Omega$.

The results of conductivity measurements on the antimony doped specimens are given in section 4.

2c. Results on Undoped Crystals

The experimental results of both two and four probe methods for colourless stannic oxide rods are shown in figure 3.2. If the straight regions of the curves 2, 4, 5 and 6 (between 700°K and 1200°K) are fitted to the equation.

$$\sigma = B \exp\left(-\frac{E_{act}}{2kT}\right), \qquad (3.1)$$

where E_{act} is known as the activation energy, the average value for E_{act} is 3.04 eV. This agrees with Kohnke (75), who measured activation energy of natural crystals.

Comparing equation 3.1 with equations 1.51 and 1.20, and assuming only electronic conduction, it is seen that

$$B = (N_c N_v)^{\frac{1}{2}} e\mu_e \qquad (3.2)$$

and is thus not independent of temperature. This will be further discussed in Chapter 4 section 3c.

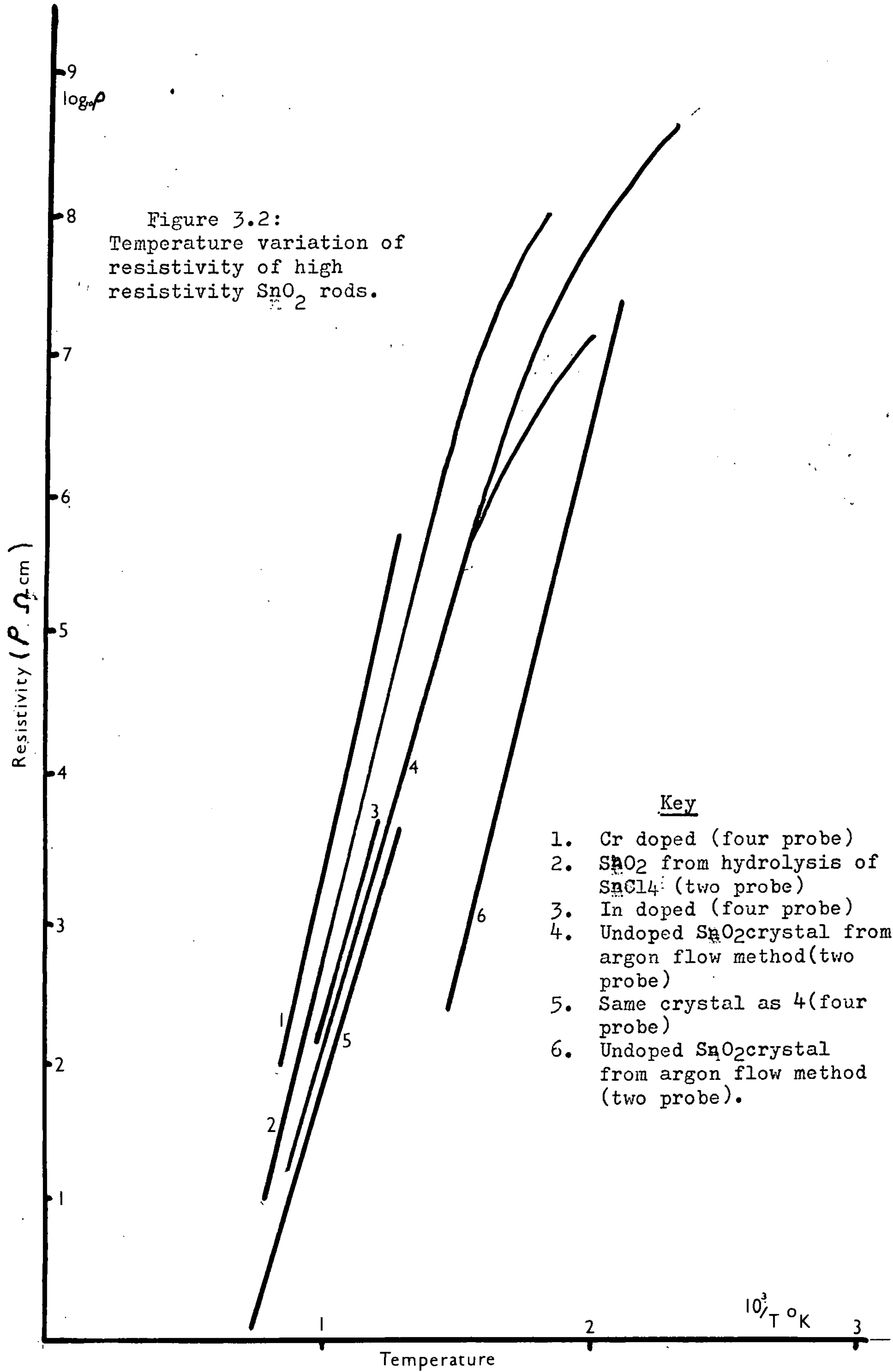

Figure 3.2: Temperature variation of resistivity of high resistivity SnO_2 rods.

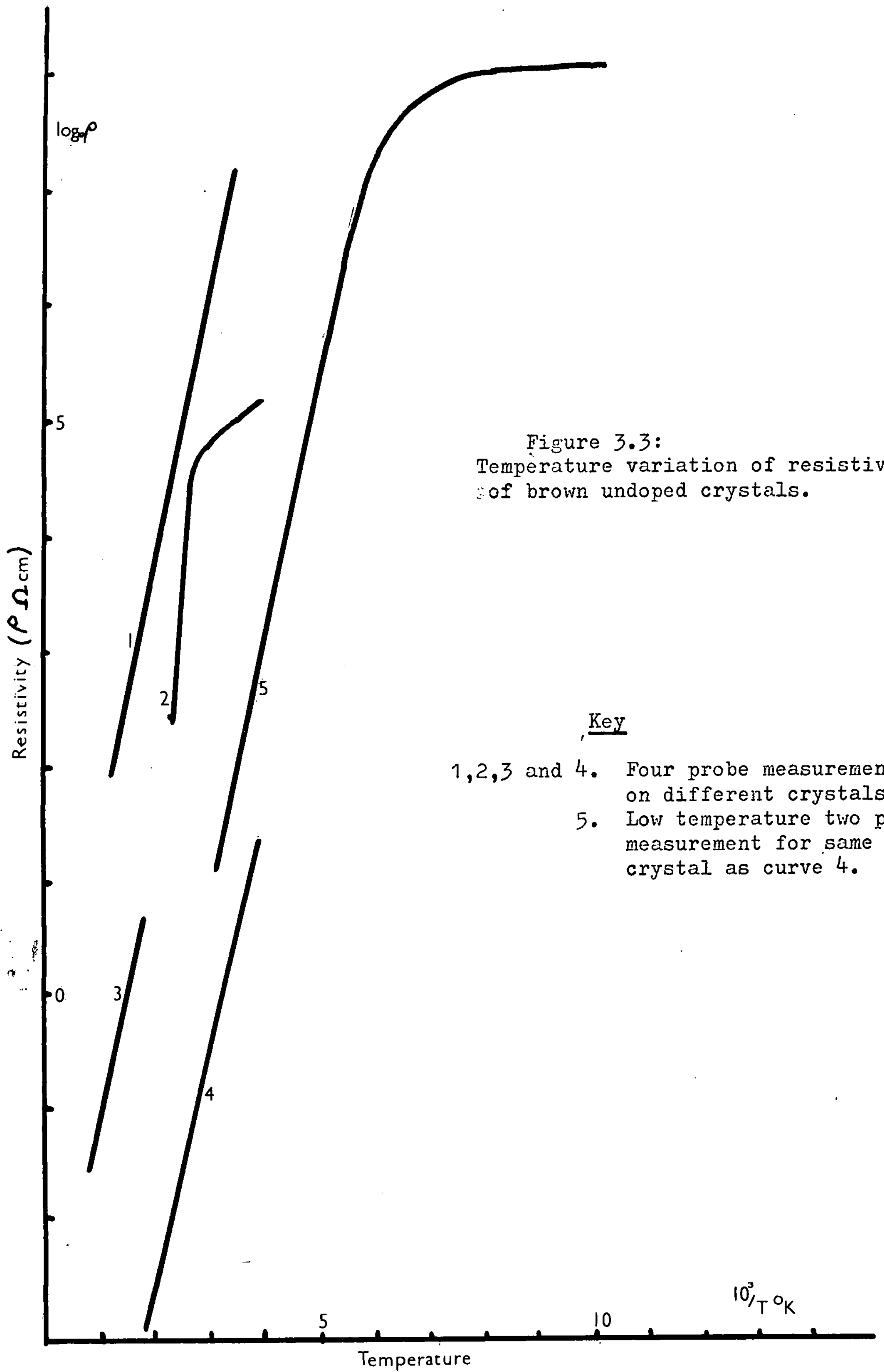

Figure 3.3:
Temperature variation of resistivity of brown undoped crystals.

The brown undoped crystals had a rather higher conductivity than the colourless crystals. The results obtained from measurements on this type of crystal are shown in figure 3.3. The low temperature measurements were made using the Hall effect holder described in section 4a. The average activation energy, as defined by equation 3.1, for these crystals was 0.94eV.

Due to the variation of B with temperature, and the variation of the band gap with temperature, the activation energy does not give a direct measurement of the band gap (see Chapter 4 Sect.3c.).

2d. Chromium and Indium Doped Crystals

The plots for the variation of conductivity with temperature for a chromium doped and an indium doped crystal are also shown in figure 3.2. The activation energies calculated from these plots were 3.7eV for the chromium doped and 3.0eV for the indium doped crystal.

The chromium doped crystal was a deep red colour (see figure O.1 D) and so it was likely that this contained a rather higher impurity concentration than the indium doped crystal, which was only a very pale yellow. By considering the electronic configuration of chromium and indium, both types of atom could act as acceptors. It is probable that the higher activation energy of the chromium doped crystal is accounted for by a variation in hole mobility. Since only one crystal was measured, definite conclusions cannot be drawn.

Section 3. Seebeck Coefficient

3a. Apparatus:

The Seebeck effect at high temperatures was measured in an apparatus based on the design of Middleton and Scanlon (76). A diagram of this apparatus is shown in

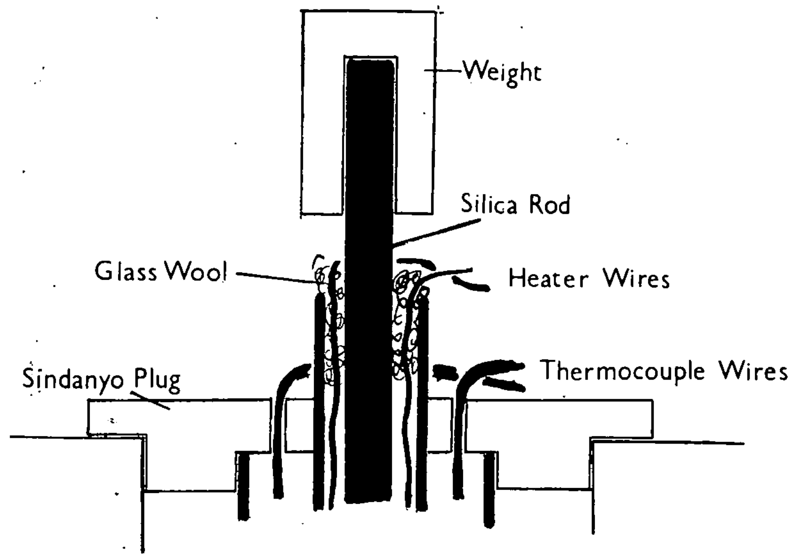

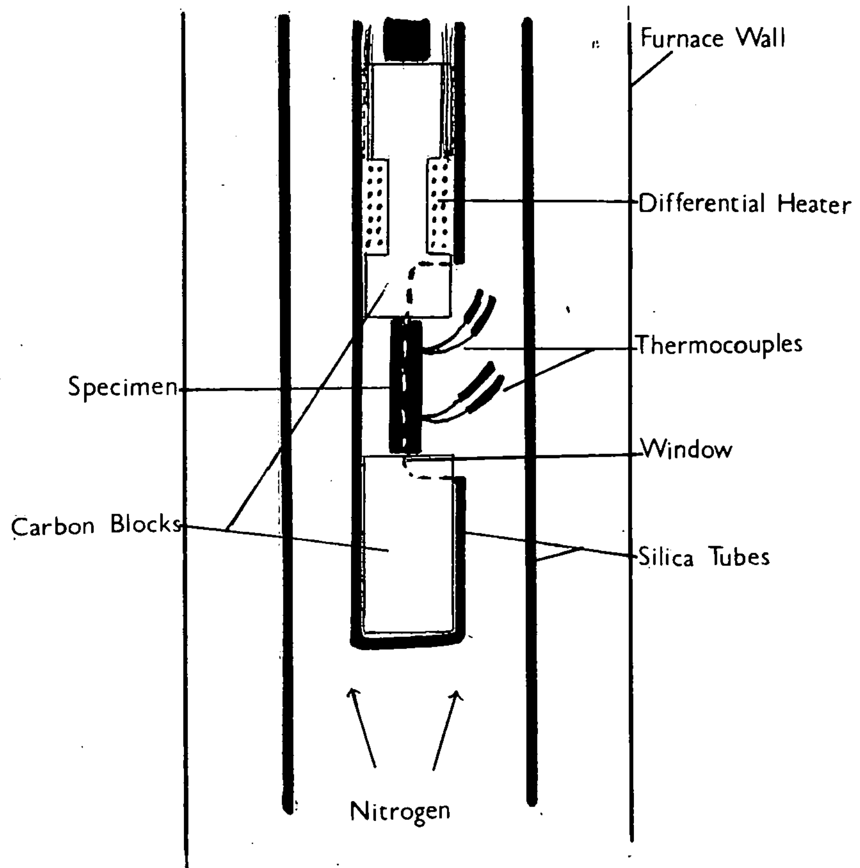

Figure 3.4: Apparatus for measuring the variation of Seebeck coefficient with temperature.

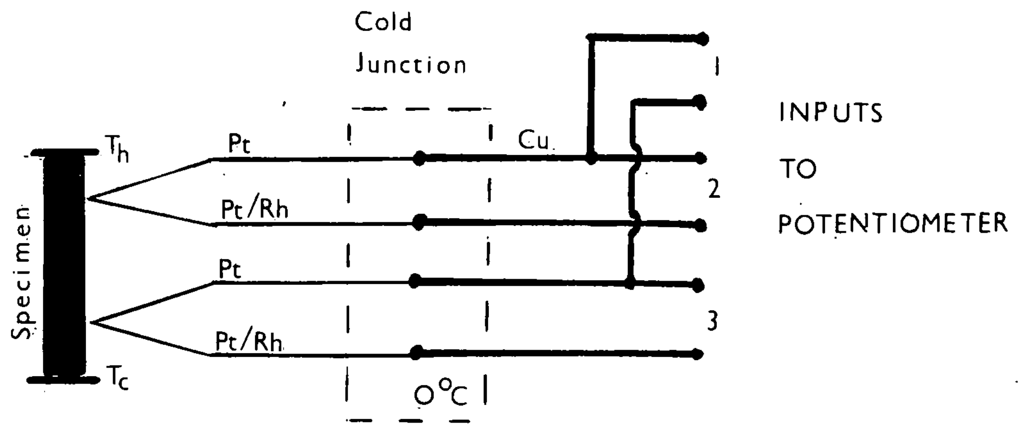

Figure 3.5: Circuit for measuring the Seebeck coefficient.

figure 3.4. By constructing it in silica and by operating it in an atmosphere of nitrogen to prevent oxidation of the carbon blocks used for the heat source and heat sink, the apparatus could be operated up to 1000° C. Kanthal resistance wire was used for the differential heater. The heater wires and thermocouple wires were insulated using "Refrasil" sleeving.

The junction between the silica tubes and the sindanyo bung were not absolutely gas tight, so a continuous stream of nitrogen was passed through the system while it was at high temperatures. The flow was stopped, and the system allowed to reach thermal equilibrium before each reading was taken.

3b. Method

The circuit diagram for the measurement of the Seebeck voltage is shown in figure 3.5. To allow for small differences in the absolute value of the Seebeck voltage of the thermocouples, the Seebeck voltage of each specimen(V_{α}) was plotted against the temperature difference (ΔT) recorded by the thermocouples

$$\Delta T = (V_h - V_c)\,\alpha_{Tc}\,(T) \quad , \qquad (3.3)$$

where V_h and V_c are the voltages of the hot and cold junctions of the thermocouples at an average temperature T and α_{Tc} is the Seebeck coefficient for the couples at the temperature T. α_{Tc} was obtained from tables (77).

The Seebeck coefficient of each specimen was measured with respect to the platinum leads of the thermocouples. To obtain the absolute value of α_{SnO_2}, the value of α_{Pt} had to be subtracted from the observed value (see equation 1.68). Values of α_{Pt} were obtained from Nyström (13).

The thermocouples were attached to the specimens using 'Silver Dag'. If possible, small holes were

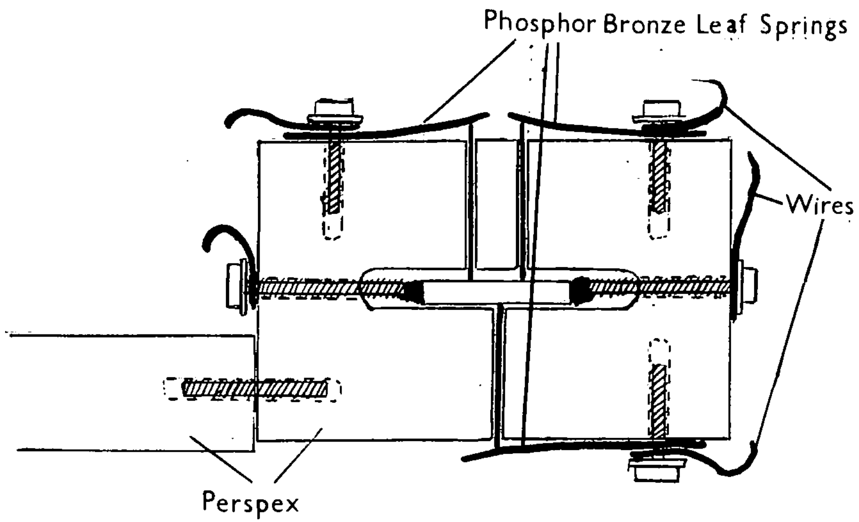

Figure 3.6(a): Hall effect specimen holder

Figure 3.6(b): Circuit for measuring the Hall effect.

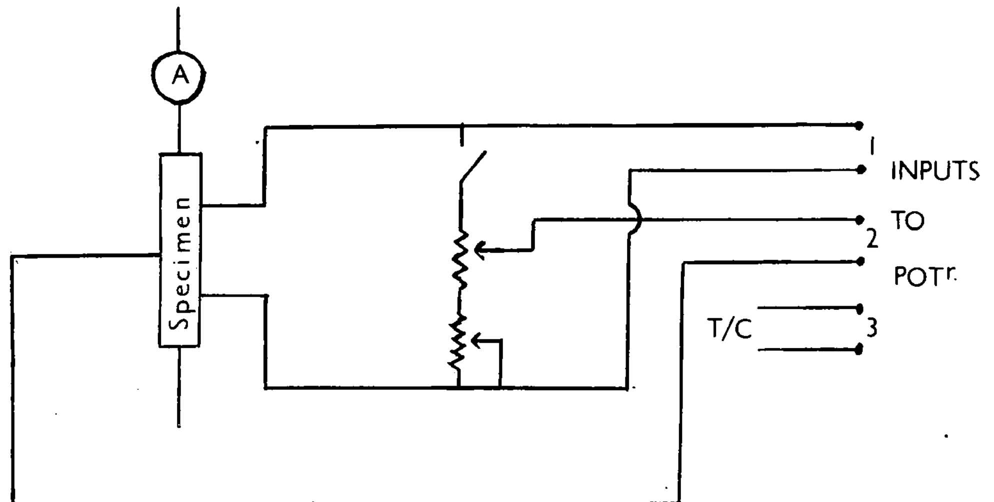

Figure 3.7: Temperature variation of Seebeck coefficient of antimony doped specimens.

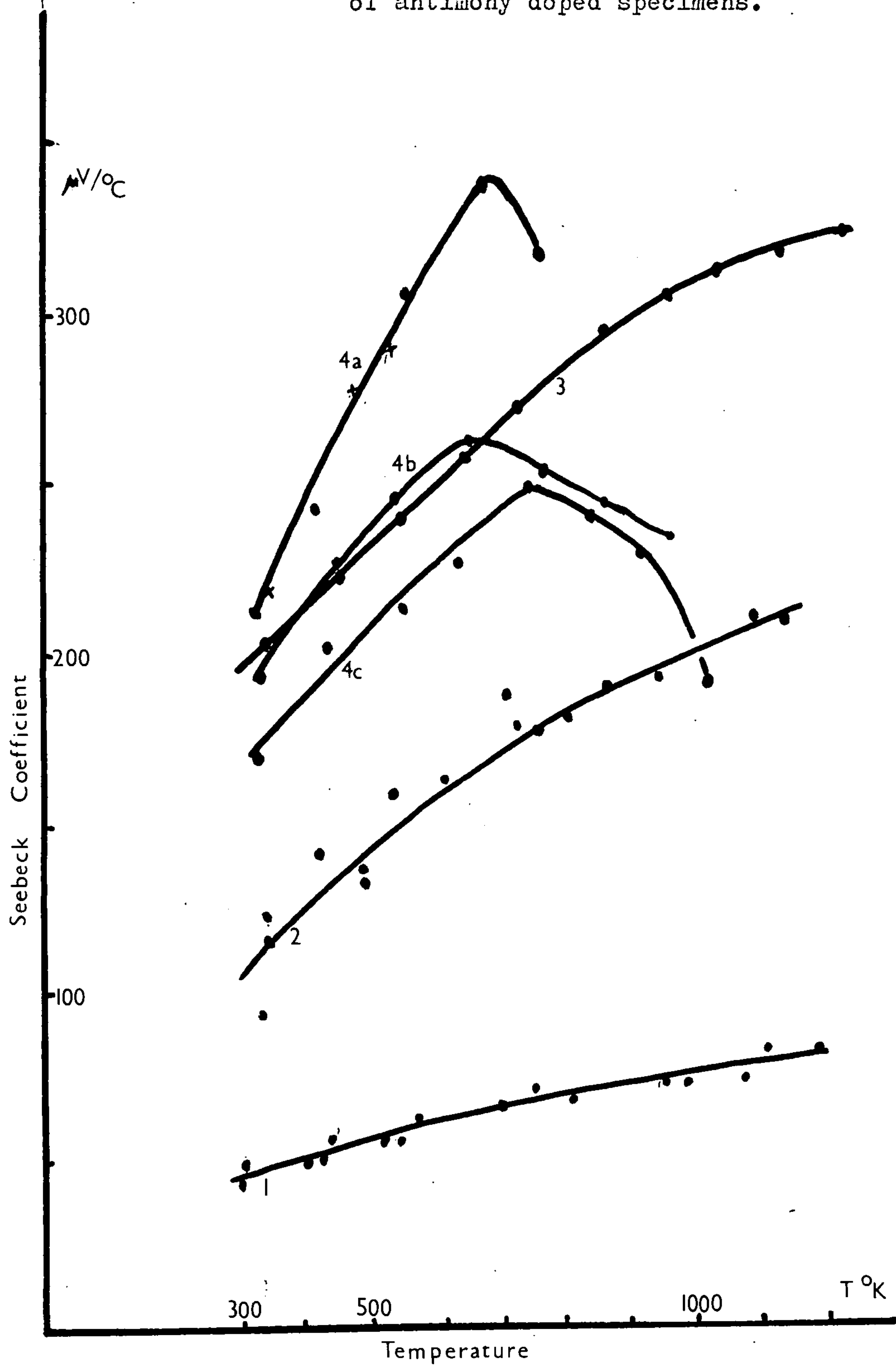

drilled in the specimens, using an abrasive cutter, into which the thermocouple junctions could be inserted. This was only practicable for one crystal (specimen 3).

The Seebeck voltage was measured on a Philips high impedance valve microvoltmeter (model GM 6020) which gave a continuous indication of its magnitude and stability. The voltage was also checked using the potentiometer.

On the specimens of high resistivity the electrical pick-up was greater than the Seebeck voltage. So measurements could not be made without screening the whole apparatus. On the antimony doped specimens of low resistivity, extraneous pick-up was negligible and reproducible results could be obtained.

3c. Results

The variation of Seebeck coefficient with temperature of four antimony doped crystals was measured. Table 3.1 shows the dimensions of each specimen as well as the values for R, n, σ and μ at room temperature. Specimens 1 and 2 were of the [001] prismatic form and so all measurements were taken parallel to the c-axis. Specimens 3 and 4 were of the [100] prismatic form and the measurements were taken parallel to one of the a-axes. In each of these specimens (3 and 4) the c-axis was parallel to the shortest side.

As Marley and McAvoy (45) and Koffyberg (59) reported a variation in defect concentration between the surface and the bulk of some crystals, the surfaces were ground down using 800 grade carborundum powder. It was easier to make ohmic contacts to the ground surface than to the surface as grown.

Figure 3.7 shows the measured variation of the absolute Seebeck coefficient of each specimen with temperature. The values were always negative.

The results of low temperature Seebeck measurements are shown in Table 4.2.

3d. Irreproducibility of Specimen 4

The curves 4a,4b and 4c on figure 3.7 show the results of successive runs to measure the variation of Seebeck coefficient with temperature. The first run showed a sudden fall in the Seebeck coefficient at 750°K. Because of this, the run was terminated and the contacts remade. The second run (curve 4b) gave a lower value than the initial run for the Seebeck coefficient at all temperatures and again the value fell at temperatures above 700°K. As the initial results gave a value of effective mass that was similar to that obtained for specimen 3, the crystal was examined a third time at a later date. The value of Seebeck coefficient was still lower, as shown by curve 4c.

The Hall coefficient was remeasured and found to be 2.98, a reduction of 5% on the value obtained previous to performing the first set of Seebeck measurements, (see Table 3.1) and within probable experimental error. The conductivity appeared unchanged.

Since the Seebeck measurements were performed in a nitrogen atmosphere, it was suspected that this fall in the Seebeck coefficient at high temperatures was due to the loss of oxygen from the surface layer of the crystal, and that the oxygen vacancies provided donor centres. Thus the carrier density at the surface of the crystal was increased.

To confirm this, the crystal was heated in air at 1000°C for four hours. A few Seebeck measurements were made and the results were found to agree with the first run. The points obtained are marked with crosses on the curve 4a.

It has already been reported (78) that the addition of antimony stabilises thin films of stannic oxide. It was no doubt because specimens 1 and 2 contained a higher concentration of antimony that this irreversible effect did not occur in them.

The thermocouples in specimen 3 were embedded in holes drilled into crystal. Since these holes were filled with 'Silver Dag' it was unlikely that the oxygen could escape from the surface underneath the thermocouples. So the effect may have been unnoticed on this specimen.

Table 3.1

Dimensions and values of electrical parameters at room temperature of antimony doped crystals.

Specimen	1	2	3	4
R($coulomb^{-1} cm^{-3}$)	-7.1×10^{-2}	-0.80	1.23	-3.12
N (cm^{-3})	$8.8\ 10^{19}$	$8.2\ 10^{18}$	$5.1\ 10^{18}$	2.10^{18}
σ Ω^{-1} cm^{-1}	$1.2\ 10^{3}$	91	102	27
μ cm^{-2} $V^{-1}sec^{-1}$	87	69	125	85
width (mm)	1.22	1.48	2.18	1.22
thickness (mm)	0.95	1.34	1.13	0.44
length (mm)	8	7	$5\frac{1}{2}$	$5\frac{1}{2}$
Colour	Dark Blue	Pale Blue	Very Pale Blue	Almost Transparent

Section 4 Hall Effect

4a. Low Temperature

A five probe method was adopted for measuring the Hall effect of the low resistivity, antimony doped crystals. Diagrams of the apparatus and circuit are shown in figures 3.6a and 3.6b. The current control

circuit was similar to that used for the four probe conductivity measurements. The potentiometer was a Tinsley model 3387B capable of measuring divisions of one microvolt. The Hall effect holder was also used for the four probe conductivity measurements at low temperatures and for the two probe measurements on specimens of high resistivity at low temperatures.

The Hall effect holder was enclosed in a split copper cylinder ($1\frac{1}{4}$" diameter and 2" long), the centre of which was milled out to accommodate it. The cavity was lined with mica for electrical insulation. The whole apparatus was inserted into a closely fitting Dewar flask, which was filled with liquid nitrogen. When the system had reached liquid nitrogen temperature and readings had been taken at this temperature, the excess liquid was poured out and the apparatus allowed to warm up slowly while the conductivity and Hall voltage were measured. The temperature was measured with a copper-constantan thermocouple. The magnet used had 4" diameter pole pieces with an air gap of 2". It was capable of producing a field of 6 kilogauss.

Current contacts were made using indium-gallium paste or indium amalgam. The potential probe contacts were made by evaporating small areas of indium on the crystal surface in the correct positions. A small pellet of indium was placed on top of the evaporated layer. The copper probes were pressed into this indium pellet and held by the phosphor bronze leaf springs.

4b. <u>High Temperature</u>

At high temperatures a system was used that was first

employed by Breckenridge and Hosler (79) for measuring the Hall effect in rutile. Small silica posts were fused to a silica plate. Platinum leads were attached to these posts. One end of these leads was pressed into an indium pellet on the specimen to form the potential probe contacts. The other end was brought out to the external circuit which was essentially the same as shown in figure 3.6b. Platinum paste was used for the current contacts. A small furnace, of external dimensions 5" x 2" x 1¾", was constructed to fit between the pole pieces of the magnet. A silica tube, 2 cm diameter and 12 cm long, was wound with 36 s.w.g. Kanthal resistance wire. The resistance of the element when cold was 120 Ω. The tube was coated with alumina cement and enclosed in a syndanyo case. The resistance heater was powered from the mains through a 2 amp 'Regavolt' variable voltage transformer. The furnace was easily capable of reaching 1000°C.

The limitation on the high temperature operation of this apparatus was set by the contacts. Above the melting point of indium the contacts had little mechanical strength and the slightest vibration would disturb them. Oxidation of the surface of the molten contacts did not affect results. No measurement was obtained above 600°K.

4c. Variation of Mobility with Temperature

There was no detectable change in the Hall coefficient of any of the four specimens over the range of temperature measured. The most accurate readings were obtained at room temperature and liquid nitrogen temperature where a constant temperature could be maintained while a number of readings were taken. The room temperature values of Hall coefficient are given in table 3.1.

Since the magnitude of the Seebeck coefficient indicated that all the specimens were degenerate at low

Figure 3.8: Temperature variation of electrical conductivity of antimony doped specimens.

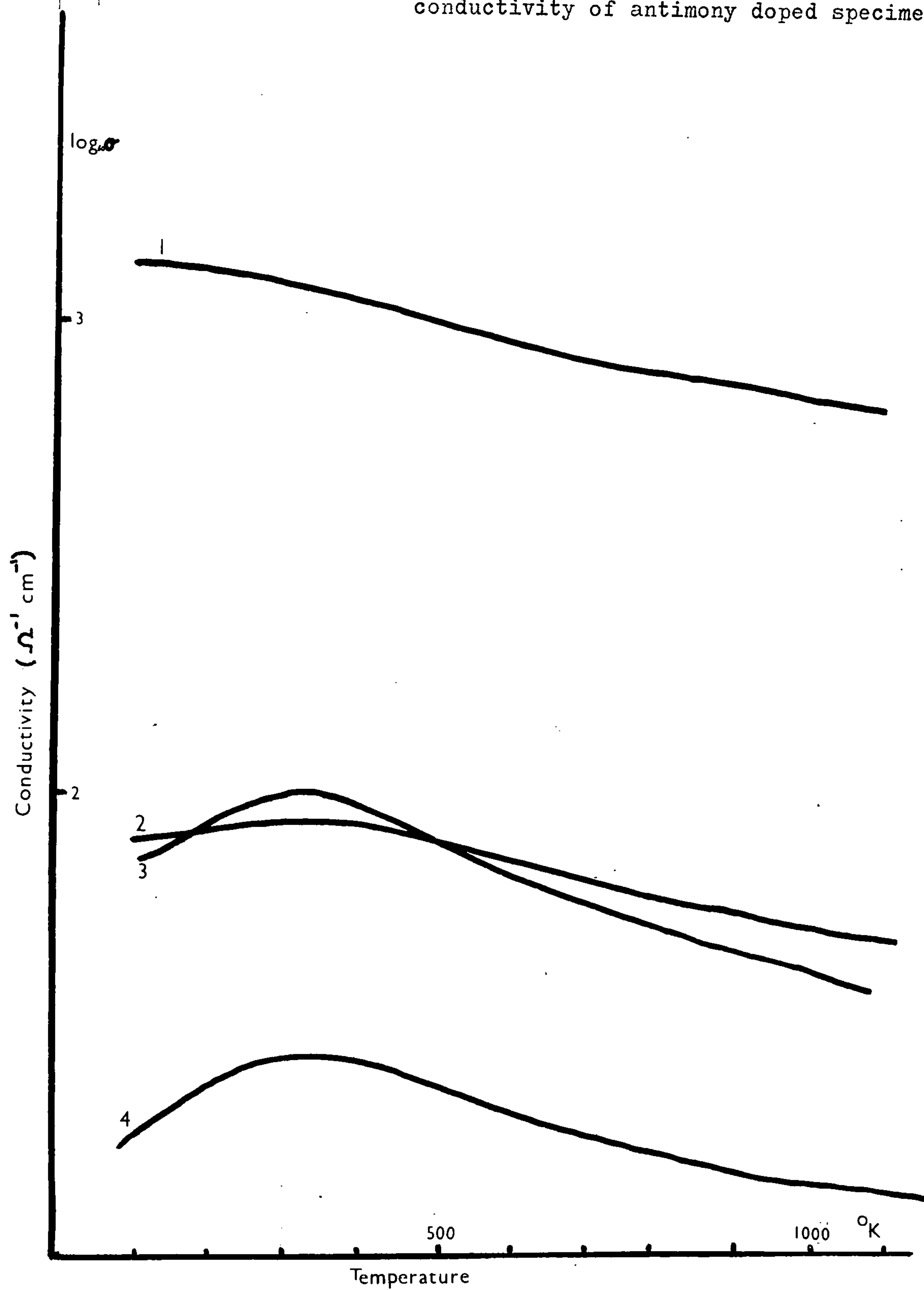

Figure 3.9: Temperature variation of mobility of antimony doped specimens.

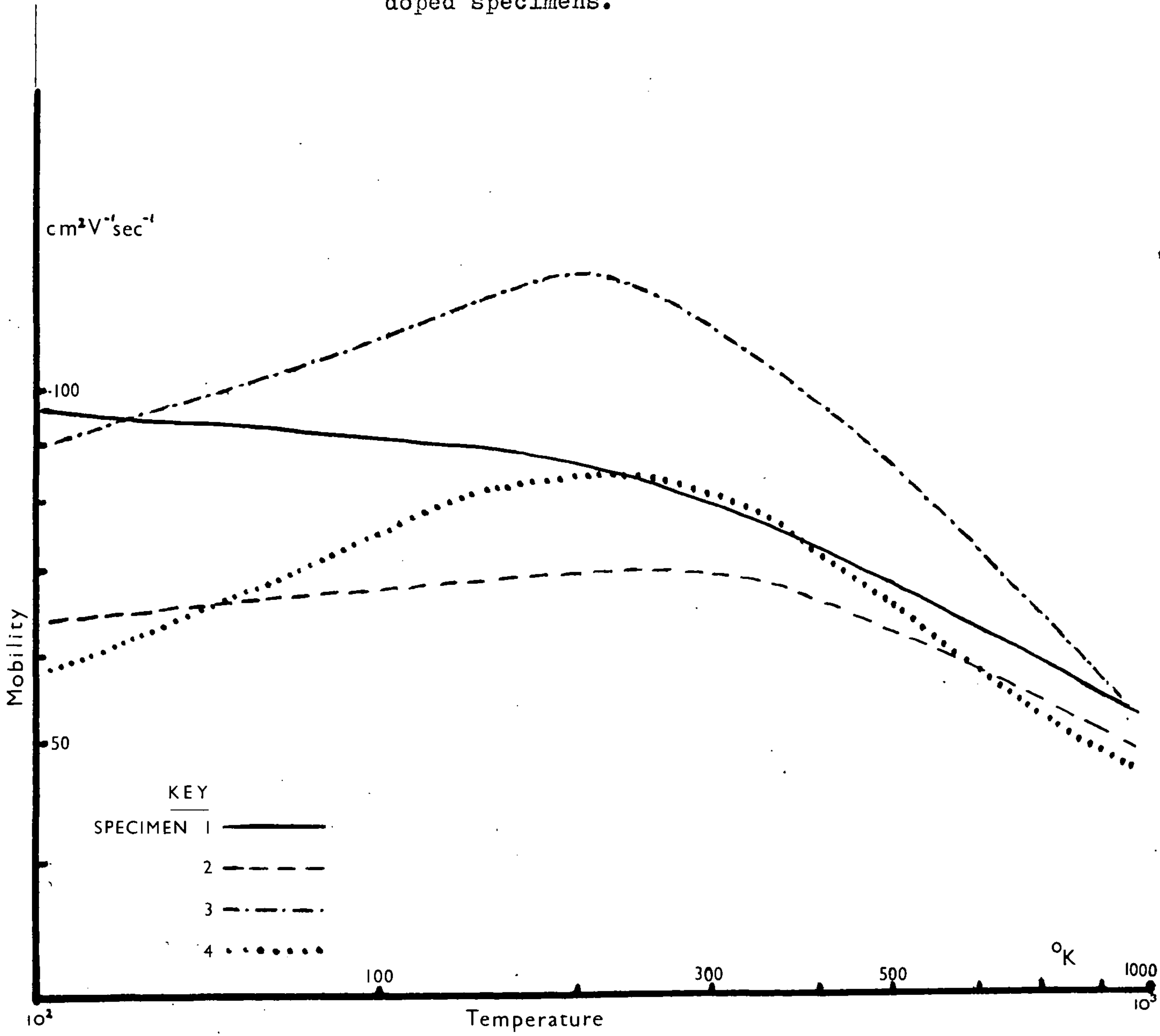

temperatures, the factor r in equation 1.92 was taken as unity in calculating the carrier density and drift mobility.

Figure 3.8 shows the variation of conductivity with temperature of the four samples. Since no variation in Hall constant was detected, the variation of mobility with temperature (figure 3.9) was calculated assuming that the carrier density was constant up to 1000°C.

The interpretation of the temperature variation of mobility is found in Chapter 4 section 2.

4d. Errors

The largest errors in the absolute value of the mobility were probably made in measuring the dimensions of the sample and the separation of the voltage probes. Each of these measurements could not be expected to have an accuracy greater than within 5%.

The value of μ in terms of the quantities that were actually measured may be given by

$$\mu = R\sigma = \frac{V_H}{V_r} \frac{l}{H w} , \qquad (3.4)$$

where V_H is the Hall voltage, V_r the voltage between the resistance probes, l the separation of the voltage probe, w the width of the specimen and H the magnetic field strength.

The measurement of the magnetic field was made using a flux meter. The scatter of points indicated a possible error of 2%. Fluctuations in the Hall voltage readings could easily account for an error of one microvolt. On specimens 1 and 2 the maximum Hall voltage attainable was 30 μV. The current became unstable if increased further. The error on the other specimens was of a similar relative magnitude. The error in measuring the voltage across the resistance probes was negligible compared with these other quantities. The maximum probable error in the absolute

value of the mobility is therefore 15%. The accuracy of the relative values of mobility measured on the same sample at different temperatures was very much better ($<$ 1% error). Even the large error allowance of 15% does not account for the range of values obtained for the mobilities of the four specimens. These figures do not, however, take into consideration possible inhomogeneities of the specimens. If the magnitude and geometry of inhomogeneities is unknown it is impossible to predict accurately any effect they may have. The thermoelectric probe showed that the donor concentration of specimen 3 was fairly uniform (sect.5d), so the results from this specimen are probably the most reliable.

Section 5. Other Measurements

5a. Luminescence

Crystals of stannic oxide and stannic oxide powder were examined under an ultra-violet lamp with the spectral distribution between 0.35μ and 0.40μ. The antimony and chromium doped crystals showed no observable luminescence, nor did the colourless undoped crystals. The brown crystals, indium doped and gallium doped crystals and stannic oxide powder all showed a faint yellow luminescence at low temperatures. The brightest luminescence was found in the whiskers grown by the hydrolysis of $Sn\,Cl_4$ in an oxyhydrogen flame. These appeared a greenish white at liquid nitrogen temperature and the characteristic yellow colour at the temperature of solid carbon dioxide. This luminescence disappeared just below room temperature. At room temperature it was believed that a faint red luminescence was observed.

The luminescence from these whiskers was bright enough to obtain a spectral distribution curve, shown in figure 3.10. The slits of the Hilger and Watts spectrometer were at their largest apperture (1.5mm) so fine

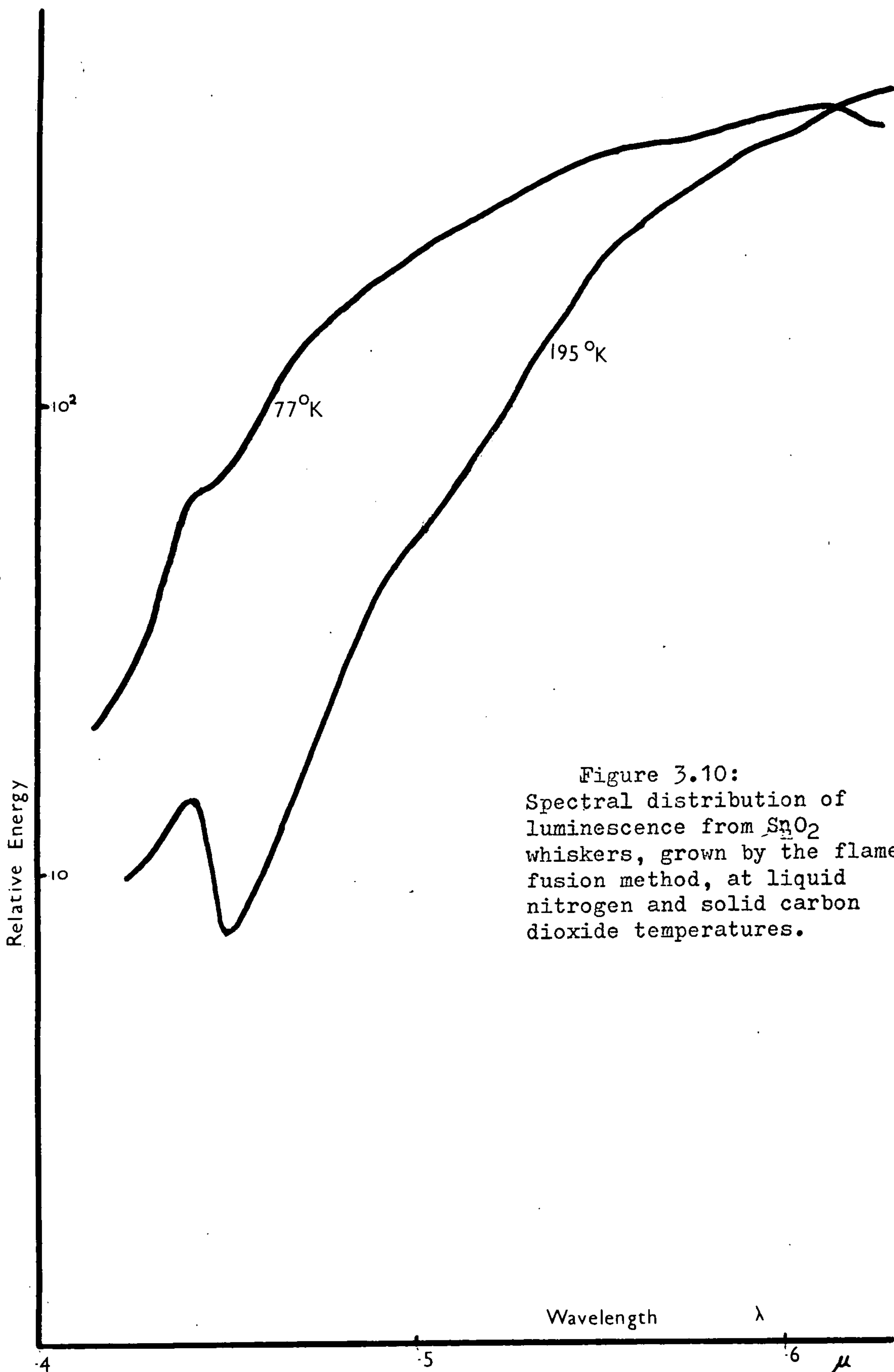

Figure 3.10:
Spectral distribution of luminescence from SnO_2 whiskers, grown by the flame fusion method, at liquid nitrogen and solid carbon dioxide temperatures.

structure of the peaks was not expected. The photo-multiplier was calibrated against a thermopile and the relative energy response plotted against wavelength. Readings were taken at intervals of 0.1μ.

Figure 3.10 shows probable peaks in the luminescence at 0.44, 0.49, 0.55 and 0.60 μ which correspond to 2.8, 2.5, 2.3 and 2.1 eV respectively. Most of these were probably due to surface states.

5b. Photoconductivity

The brown crystals also showed an increase of conductivity when illuminated with u.v. light at room temperature and liquid nitrogen temperature. Normal daylight had no observable effect.

Houston and Kohnke (80) have reported photoconductivity, and measured the thermally stimulated photocurrent in crystals grown from a flux of copper oxide (Cu_2O). Copper is known to diffuse easily into most substances and also to increase the sensitivity of photoconductivity in Zn S and Cd S (81). Copper was introduced into a rod of stannic oxide by evaporating a layer of copper on to the surface and heating it in an evacuated sealed silica tube at 900° C for a few hours. The conductivity of the specimen increased from 10^{-6} to $10^{2}\ \Omega^{-1}cm^{-1}$. This value of conductivity remained constant between room temperature and 400° C, but ~~suddenly~~ decreased, indicating that the copper had diffused out of the crystal, when left at this temperature overnight. A qualitative appraisal of the photoconductivity of the Cu doped crystal indicated that it did have a greater sensitivity when illuminated by the u.v. lamp.

No photoelectric effect was detected on the colourless

undoped crystals.

5c. Electron Paramagnetic Resonance

Stannic oxide, being of a similar structure to rutile, is also a suitable host lattice for paramagnetic ions for electron spin resonance measurements. It was for this reason that chromium doped crystals were grown. One of the largest crystals was mounted in a Q-band spectrometer (34.4 kMc/s), many lines were observed. Some of these were identified as chromium lines by comparison with From (82) who has studied the paramagnetic resonance of Cr^{3+} in $Sn\ O_2$. The other lines observed were believed to be due to iron Fe^{3+}, which probably originated from the chromic oxide doping material. The signal was too weak for measurement of the spin relaxation times.

An undoped crystal was examined in the X band (94.4 kMc/s) spectrometer at room temperature. Many lines were observed at fields between 3.3 and 4.1 Koersted. No attempt has been made to identify them.

5d. Effect of High Fields

Under high fields, Ohm's law for a conductor will break down. The electrons in the solid will reach a terminal velocity when

$$\frac{1}{2} m v^2 = h \nu_o , \qquad (3.5)$$

where ν_o is the frequency of optical mode vibrations, and v the average velocity of the electrons.

Thus, at high fields, a saturation value of current is attained. This current does not increase significantly with further increase in the field until just before breakdown occurs.

mA

5

Current

100

V 200

Voltage

Figure 3.11:
Typical measurement of current behaviour under high fields at 77°K.
Crystal thickness 0.38 mm
Surface area 4 sq. mm.

Figure 3.12: Circuit for Thermoelectric probe.

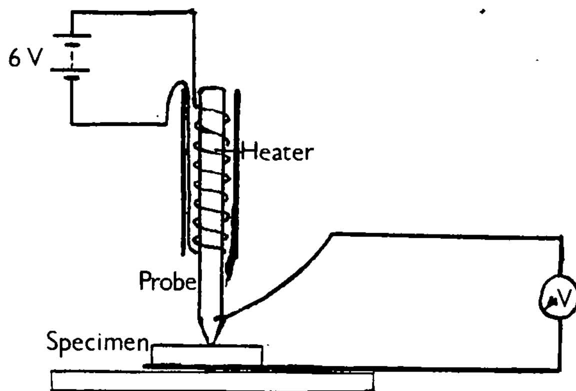

N.8. The high field conductivity measurements were performed on brown undoped crystals. In figure 3.11 it can be seen that I is approximately proportional to V^2. A. Rose (R.C.A. Rev. 12, 362, (1951)) proposed that for a trap free solid in which the current is limited by space charge $I \propto V^2$. indium contacts were used. Indium has a low work function and so the contacts could act as electron injecting contacts, which would account for the apparently small, low field, resistivity of the sample ($\sim 50\,\Omega\,$cm).

Stannic oxide plates about .04 cm thick were held in a jig between indium coated copper surfaces and voltages of up to 300 V applied. A typical result is shown in figure 3.11a. The experiment was performed in liquid nitrogen, but even so it is most likely that the deviation from Ohm's law was due to local heating of the crystal. No saturation current was noticed before breakdown, so no conclusions could be drawn.

The breakdown field varied from 30-75 KV/cm for different crystals.

5e. Thermoelectric Probe

One means of obtaining a qualitative estimate of the homogeneity of a specimen is to use a thermoelectric probe. The probe used was essentially an electrically heated copper rod with a small blunt point at one end that protruded from beyond the insulatory sheath that surrounded it. The copper rod was connected to one side of the input to the Philips microvoltmeter. The other side of the input was attached to the back face of the crystals which were coated with 'Silver Dag'. A diagram of the circuit is shown in figure 3.12. If the doping level were uniform throughout the crystal, no variation in the voltmeter would be expected as the probe was placed at different points on the front face of the crystal. When used on the four antimony doped specimens, only for specimen 3 was the variation small ($<$ 10%). The other crystals showed quite large variations ($>$20%).

CHAPTER IV

DISCUSSIONS AND CONCLUSIONS

Section 1. Previous Work on Stannic Oxide

1a. Thin Films

The earliest electrical measurements on stannic oxide were made in 1937 by Bauer (83). The samples were poly-crystalline thin films prepared by the thermal oxidation of tin evaporated on quartz plates. The specific conductivity of these films was between 10^{-4} and 34 Ω^{-1} cm^{-1}, and the mobility, from Hall effect measurements, was between 0.9 and 6.6 cm^2 V^{-1} sec^{-1}.

Since then the usual method of preparation has been by the hydrolysis of a suitable compound of tin, usually stannic chloride ($Sn\ Cl_4$) in an alcoholic or aqueous hydrochloric acid solution. The solution is sprayed on to a hot substrate. Papers by Aitcheson (84), Burkett (85) and Holland (86) contain details of the production of thin films. Mochel (88) discovered that the addition of antimony stabilised the films and gave them a higher, and even positive, temperature coefficient of resistivity. Stannic oxide films on a glass base have been manufactured extensively as resistors and although there is extensive patents literature on the subject, relatively few technical papers have been written.

Two papers by Ishiguro et al (54) and Imai (88) report electrical and optical measurements on both undoped and antimony doped tin oxide films. Arai (78) interprets these results and his own, proposing a tentative band scheme. Among the conclusions of these papers, was that the predominant scattering mechanism at room temperature,

even in the undoped crystals, was that of ionised impurities.

Miloslavskii and Lyashenko (62, 89, 90) performed similar measurements entirely on antimony doped films. They concluded that each antimony ion introduced into the lattice gives rise to one donor centre, the depth of which they found from optical measurements to be 0.15 eV. Reference 90 explains the infra red absorption in these doped films on the assumption that the electron effective mass varies with the donor concentration.

The most recent publications of the optical and electrical properties of undoped tin oxide films have been by Koch (55, 91, 92). The electrical properties of the films were measured between liquid air temperature and 100°C: above this temperature irreversible changes took place. The antimony doped films of Arai(78) were stable even above 800° C. Koch interpreted his results on the theory of conduction in polar semiconductors proposed by Howarth and Sondheimer (20): thus recognising that the scattering was by the polar longitudinal optical mode vibrations of the lattice. A minimum in the Hall constant at 150°K was discovered. According to the theory of Lewis and Sondheimer (93), this coincides with the characteristic temperature of the optical phonons. The temperature coefficient of resistivity of the films did not obey the predictions of the Howarth and Sondheimer theory.

In reference 91, the value of the effective mass is discussed. A value of 0.17 m_o was deduced from the measurement of optical dispersion.

1b. Polycrystalline Samples

Loch (94) prepared samples of stannic oxide by compressing $Sn\ O_2$ powder with various proportions of antimony

trioxide (Sb_2O_3) to act as a donor impurity. The electrical conductivity and Seebeck coefficient were measured on these samples in a vacuum. The mobility of these specimens was in the range 10.9-12 $cm^2 V^{-1} sec^{-1}$ and it did not vary with temperature over the range covered (100-800°C). The fact that this mobility is very much smaller than the values subsequently obtained from measurements on single crystals indicates that the effect of grain boundaries and other imperfections was considerable. Irregularities in the high temperature results were interpreted as being due to the antimony coming out of solution.

1c. Natural Single Crystals

There does not appear to be any data published on single crystals of stannic oxide before those of Kohnke (75), who measured the electrical and optical properties of good natural crystals. He found that the activation energy for intrinsic conduction above 800°K was 3.05 eV; and the energy gaps as obtained from optical absorption and photo-conductivity were 3.54 and 3.44 eV respectively. Room temperature Hall mobilities varied from 7 to 315 $cm^2 V^{-1} sec^{-1}$ and increased with increasing carrier concentration.

1d. Synthetic Single Crystals

Publications on methods of crystal growth have already been mentioned in Chapter 2.

Nagasawa et al (56, 95) have published measurements made on single crystals which were grown by the hydrolysis of stannic chloride. Marley and Dockerty (96) have reported the results of measurements on several undoped and antimony doped crystals grown by the helium flow method of Marley and McAvoy (58). These results are discussed

Key to Figure 4.1

	Author	Material	Reference
————————	Koch	Thin Films	55
--- • ---	Imai	do.	88
A	Arai	do.	78
I	Ishiguro et al	do.	54
....	Van der Maesen and Witmer	do.	97
-•-•-	Van Daal and Enz	Single Crystal	98
- - M - -	Marley and McAvoy	do.	45
N	Nagasawa et al	do.	56
◘ ◘ ◘○	do. do.	do.	95
-••-••-	Kohnke	do.	75

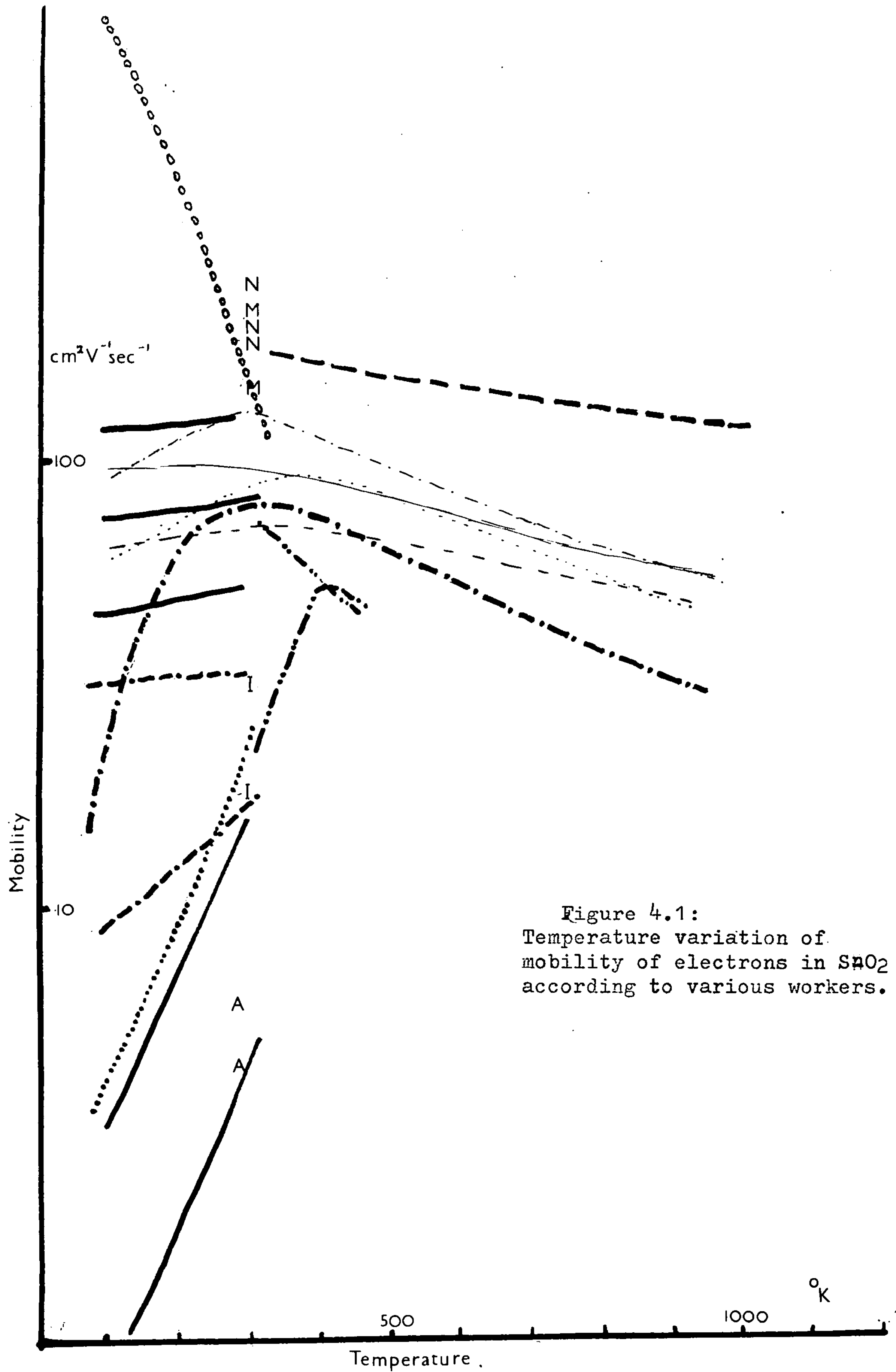

Figure 4.1: Temperature variation of mobility of electrons in SnO_2 according to various workers.

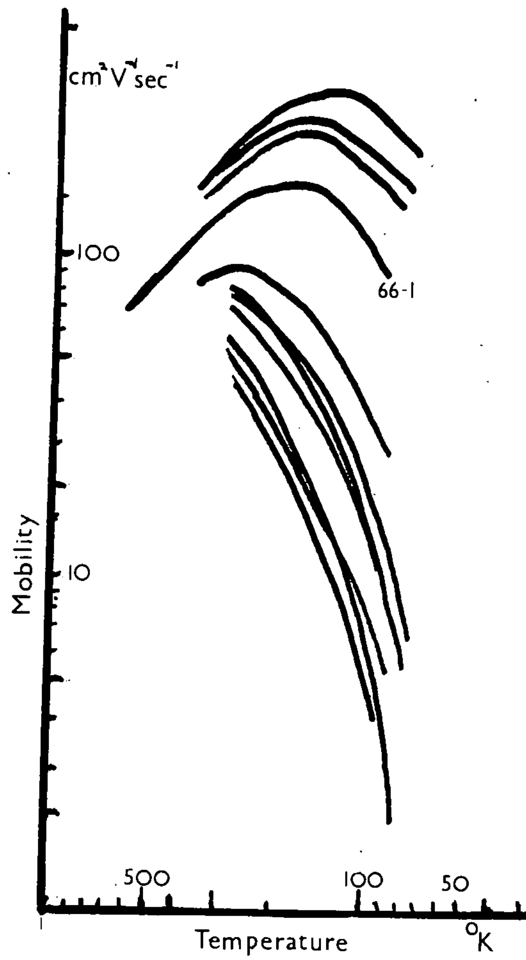

Figure 4.2: Temperature variation of mobility of various crystals as measured by Marley and Dockerty (96).

more fully in sections 2c and 2d.

1e. Summary of Mobility Measurements

Figure 4.1 shows most of the published results of mobility measurements on stannic oxide. The results of Marley and Dockerty are omitted for clarity and are shown in figure 4.2.

All these results show the same general trend. The mobility increased with increasing temperature up to about 300°K and then decreases with increasing temperature up to the highest temperature (1200°K) at which measurements have been made. The notable exception of this is the recent result of Nagasawa et al (95).

Koch (55) shows that if the scattering is by optical mode vibrations, according to the Howarth and Sondheimer theory (20):

$$\sigma \propto n^{4/3} , \qquad (4.1)$$

where n is the carrier density,

His room temperature results approximately obey this relationship. The temperature dependence of mobility of the films below room temperature is probably influenced more by ionised impurity scattering and so the behaviour predicted by this theory is not observed.

Section 2. Variation of Mobility with Temperature

2a. Above 300°K

Figure 3.9 shows that the variation, both at low and high temperatures, of mobility closely obeys a $\mu \propto T^{x}$ relationship. The value of x is different for each specimen at both extremes of the temperature range over which the mobility was measured. At high temperature the two crystals with the highest carrier densities had a value of x that was very nearly $-\frac{1}{2}$.

A simple theory of scattering by optical modes states that for high temperatures ($kT \gg h\nu_0$) $x = -\frac{1}{2}$ (99). However, this result is obtained using Maxwell-Boltzmann statistics for the energy distribution of the carriers and so it is not expected to apply to the degenerate case. In general, for a degenerate semiconductor, a value of $x = -1$ is predicted for all types of lattice scattering at high temperatures except, perhaps in the case of a many valley semiconductor (see Chapter 1. Sect. 5c).

The value of x is for all specimens very much greater than the $-3/2$ predicted for acoustic mode scattering. Etch pit counts show that the dislocation density is several orders too small to have any significant effect. The conclusions of Koch (55) and more recently by Marley and Dockerty (96) indicate that the important scattering mechanism at high temperatures is due to polar optical mode vibrations. The effective mass calculations of section 3 offer further evidence in favour of this.

If optical mode scattering is important in a polar crystal it is necessary to have an estimate of the coupling constant (α_c)(see equation 1.108). Reddaway (100) has recently determined by optical methods, the wavelengths of the optical modes of vibration. He proposes that the most important value of λ is 703cm ; although if more than one mode is present in the crystal all modes will give some contribution towards the coupling constant. If this value is used, together with the results that $m^* = 0.16m_0$ (see section 3), $\epsilon_\infty = 4$ (101) and $\epsilon_0 = 24$ (102), in equation 1.108, the value obtained for α_c is 0.6. Higher values of λ will produce higher values of α_c. If θ is taken to be 150° K (from reference 55) and $\theta = \frac{h\nu_0}{k}$, then $\alpha_c = 2.5$. The true value probably lies between these values. This means that an intermediate coupling theory should be applicable. The Howarth and Sondheimer theory,

which is valid for $\alpha_c \ll 1$, gives at high temperatures, $x = -1$ for both degenerate and non-degenerate semiconductors. The observed absolute value of mobility is lower than that predicted by this theory. The theory of Lee, Low and Pines (equation 1.112) fits the results quite well quantitatively if a value of $\alpha_c \sim 1$ is used. Their expression also gives $x = -1$ at high temperatures, although they do not expect it to be valid for $T > \theta$ (see reference 23).

If the values $N_I = 10^{20}$, $m^* = 0.16m_o$, and $\epsilon = 4$ are substituted into Mansfield's equation for ionised impurity scattering in a degenerate semiconductor (equation 1.116) a very small value of μ ($=8$ cm^2 V^{-1}sec^{-2}) is obtained. If the static dielectric constant ($\epsilon = 24$) is used, the result will be almost 36 times greater. However, the relaxation time obtained from equation 1.52 indicates that the high frequency dielectric constant should be used. It must also be remembered that this equation was obtained assuming a non-polar lattice and it might be expected that the effect of ionised impurities would be reduced in an ionic lattice. However, if this result ($\mu = 8$cm^2 V^{-1}sec^{-2}) is correct, and as the Seebeck and Hall measurements indicate that all the specimens are at least partially degenerate at high temperatures, most of the current must be carried in regions of the crystal that are not as highly doped as the Hall measurements indicate.

The thermoelectric probe (Chapter 3 Sect.5e) showed that there was a certain amount of variation in the doping level between different points on the crystals. The mobility of a completely degenerate semiconductor, due to ionised impurity scattering, is independent of temperature, but if there were a gradation of donor density throughout the crystal some regions could become partially or non-

degenerate as the temperature was raised. The ionised impurity component of mobility would increase in these regions. It is impossible to calculate the exact behaviour that such non-uniformities of doping would have on the mobility but it would lead to a higher value of x than the value of -1 expected for the degenerate case. For specimen 3, which was the most evenly doped, x (= - 0.91) most nearly approached this figure.

2b. Below 300° K

Since the slope of the log μ vs, log T plots (figure 3.9) at high temperatures did not fit exactly to any theory, to obtain an approximate estimate of the low temperature component of mobility the following procedure was followed.

The straight line region above 500° K was extrapolated right back to 100° K for each specimen, using the approximate formula quoted in Chapter 1 (equation 1.54)

$$\mu_{obs}^{-1} = \mu_{opt}^{-1} + \mu_{ion}^{-1} \qquad (4.2)$$

(where μ_{obs} was the observed mobility; μ_{opt} was the high temperature component of mobility, believed to be at least partly due to scattering by optical phonons; and μ_{ion} was the low temperature component at mobility which is shown here to be due to ionised impurity scattering), the variation of μ_{ion} was calculated. The result for each crystal is shown in figure 4.3. It can be seen that, considering the approximations, the variation of mobility with temperature is similar for each crystal. It also approximates to the $\mu \propto T^{3/2}$ law expected for ionised impurity scattering in a non-degenerate specimen. Also shown for comparison is the calculated value of μ obtained from the formula of Brooks (28) and Mansfield

Figure 4.3:
Low temperature component of mobility (μion) as calculated (Ch.4, sect. 2b).
Key is the same as for figure 3.9.

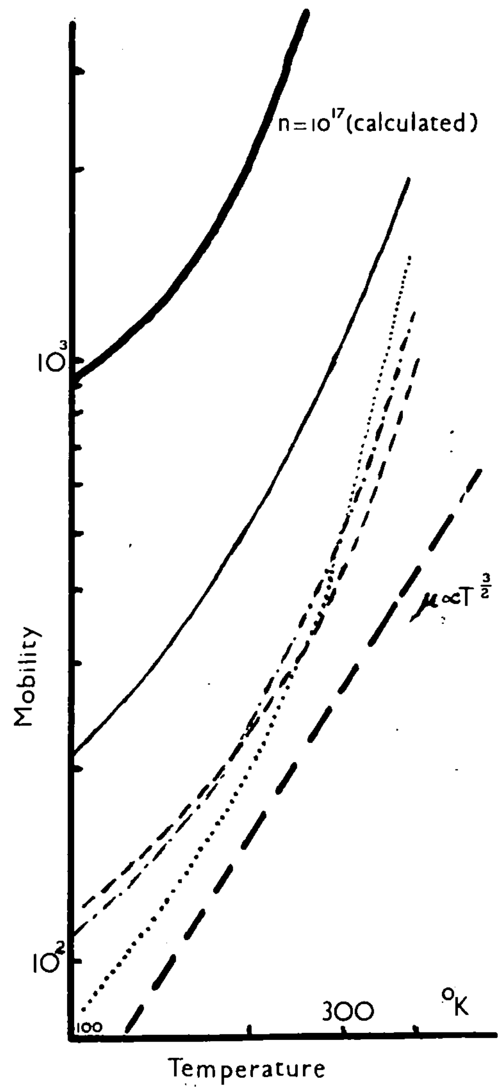

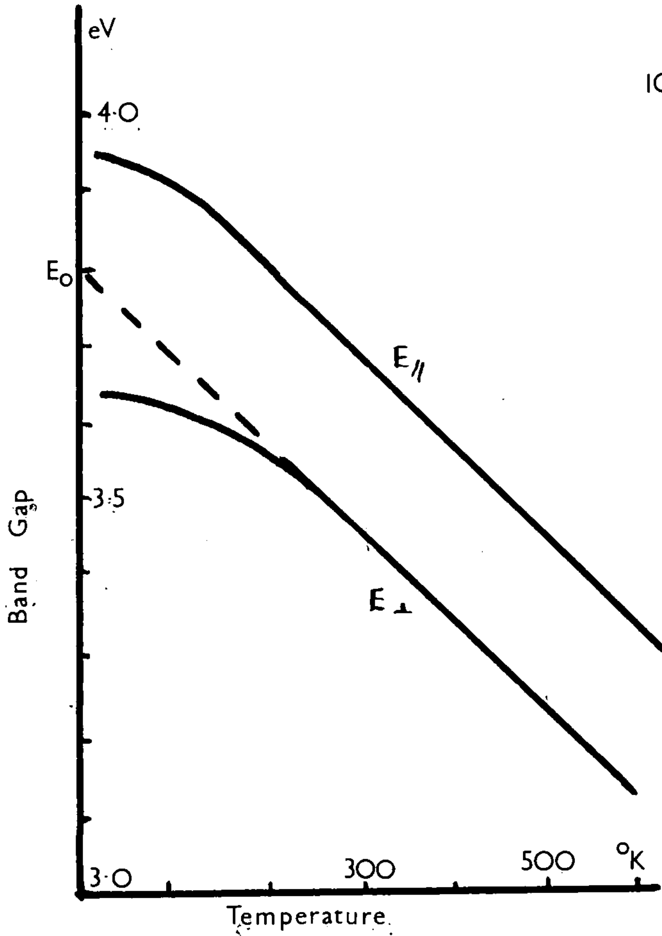

Figure 4.4:
Variation of band gap with temperature as measured by Summitt and Borrelli.

(29) (equation 1.115) for $N_I = 10^{17}$, $m^* = 0.16\ m_o$ and $\epsilon = 4$, assuming non-degeneracy. The observed behaviour is consistent with the proposal, made in section 2a, that regions of the crystals were less highly doped than others and behaved non-degenerately.

2c. Brief Discussion of the Results of Marley and Dockerty

Marley and Dockerty (96) measured the high temperature variation of mobility of one undoped crystal (specimen 66-1, figure 4.2a). The carrier density of this crystal was about 10^{18} cm^{-3} at room temperature. Irreversible effects occurred above 500°C in crystals with lower carrier concentrations. The value of x was -1.1. They used a value of $\theta = 500°K$ in the Lee, Low and Pines formula (equation 1.112) and showed that it fitted their results at high temperatures. Low and Pines, in reference 33, do express doubts on the validity of this formula when $T > \theta$.

At temperatures less than 300°K, Marley and Dockerty obtained values for x greater than 3/2. This was interpreted in terms of combined ionised impurity scattering and impurity band conduction.

2d. Brief Discussion of the Results of Nagasawa, Shionoya and Makishima

Nagasawa et al (95) have published preliminary measurements of Hall mobility and carrier density of one crystal between 90°K and 300°K. They also show that a curve μ_H = constant $\times\ T^{-2}$ fits their results over the higher end of the temperature range and interpret this in terms of predominantly acoustic mode scattering, with a further contribution due to optical modes. However, it can be shown that the same results fit a curve $\mu_H = \text{const.} \times \exp \frac{\theta}{T}$ (where $\theta = 215°K$) over the same high

end of the temperature range. The deviation from this relationship at lower temperature end can be shown to be due to ionised impurity scattering using the same analysis as described in section 2b.

They quote a value of effective mass (= $0.33m_o$) which was obtained from the room temperature Seebeck coefficient assuming acoustic mode scattering ($s = -\frac{1}{2}$ in equation 1.69). If optical mode scattering is assumed ($s=\frac{1}{2}$ in equation 1.69) and the result recalculated, an effective mass of $0.17\ m_o$ is obtained. This value is in good agreement with the present work.

Section 3. Effective Masses of Electrons and Holes

3a. Electron Effective Mass

In the simple model of a broad band semiconductor the effective mass of the carriers can be considered constant. The effective mass was calculated from the Seebeck results for specimens 1 - 4 using equations 1.18 and 1.69. The value of n was obtained from the Hall effect. Table 4.1 shows the Fermi energy (E_f) and effective mass (m^*) of each specimen for optical mode ($s=\frac{1}{2}$) and ionised impurity scattering ($s=3/2$) for temperatures between 300°K and 1200°K. Table 4.2 shows for comparison the results of the measurements of Seebeck coefficient near liquid nitrogen temperature.

The most reliable results are those obtained from specimen 3. Not only was this crystal large enough for the holes to be drilled into it to accommodate the thermocouples in the Seebeck measurements, but the thermoelectric probe indicated that it had a fairly uniform carrier density. If optical mode scattering is assumed for all T, the results show a fairly constant value of effective mass, averaging $0.16\ m_o$. The same result is also obtained for the first measurement run on specimen 4. (see Chapter 3, sect. 3d). Measurements on both these crystals were along the a-axis.

Table 4.1

Effective Mass and Fermi level of Antimony Doped Crystals

		S \ T °K	300	400	500	600	700	800	900	1000	1100	1200
Specimen 1	E_f (ev)	1/2	0.30	0.35	0.41	0.45	0.48	0.52	0.56	0.60	0.64	0.68
		3/2	0.46	0.50	0.58	0.64	0.71	0.78	0.85	0.92	0.99	1.05
	m^*/m_o	1/2	0.24	0.20	0.18	0.16	0.15	0.14	0.13	0.12	0.11	0.10
		3/2	0.16	0.14	0.12	0.11	0.10	0.09	0.08	0.08	0.07	0.07
Specimen 2	E_f (ev)	1/2	0.12	0.12	0.12	0.12	0.12	0.12	0.12	0.12	0.11	
		3/2	0.19	0.21	0.22	0.22	0.24	0.24	0.26	0.26	0.27	
	m^*/m_o	1/2	0.12	0.11	0.11	0.11	0.10	0.10	0.09	0.09	0.09	
		3/2	0.08	0.07	0.07	0.07	0.06	0.06	0.05	0.05	0.05	
Specimen 3	E_f (ev)	1/2	0.04	0.04	0.04	0.05	0.01	-0.01	-0.02	-0.04	-0.05	-0.06
		3/2	0.08	0.10	0.10	0.10	0.10	0.09	0.08	0.07	0.07	
	m^*/m_o	1/2	0.17	0.17	0.16	0.16	0.16	0.16	0.16	0.15	0.15	
		3/2	0.11	0.09	0.08	0.08	0.08	0.08	0.07	0.07	0.07	
Specimen 4	E_f (ev)	1/2	0.04	0.02	-0.01	-0.03	-0.05					
		3/2	0.08	0.07	0.05	0.03	0.02					
	m^*/m_o	1/2	0.13	0.12	0.14	0.16	0.16					
		3/2	0.07	0.07	0.08	0.09	0.08					

Table 4.2.

Effective Mass and Fermi level as measured near 100° K.

Specimen	1		2		3	
$\mu V/^{o}C$	13		29		84	
s	$\frac{1}{2}$	$3/2$	$\frac{1}{2}$	$3/2$	$\frac{1}{2}$	$3/2$
E_f	0.39	0.29	0.17	0.13	0.05	0.08
m^*/m_o	0.17	0.08	0.14	0.11	0.19	0.13

The results of specimens 1 and 2 are a little more difficult to interpret. These crystals were measured along the c-axis. Specimen 2 shows a constant value of E_f over a wide range of temperature when optical mode scattering is assumed. The average value of m* is $0.10m_o$. This value is also approached by the results from specimen 1 at high temperatures, where it might be expected that scattering by optical phonons would be more important than at the lower temperatures. If ionised impurity scattering is assumed at room temperature for specimen 1, $m^* = 0.16m_o$. This is in agreement with the value obtained for specimen 3.

In Chapter 1, section 1u, it was seen that the band need not be parabolic and furthermore Chapter 1 section 1w showed that the band could be distorted by the presence of an overlapping impurity band at high impurity concentrations. If this was occurring in specimen 1, we might expect the high temperature results to give the nearest value to that expected for the undistorted conduction band. This is because the number of impurity states depends on the number of impurity ions present in the crystal and this is constant; whereas the effective density of states in the conduction band is proportional to $T^{3/2}$. So the ratio of the number of states in the conduction band to the number of impurity states is increased as the temperature is increased.

On this reasoning it could be argued that there is a variation of effective mass with crystallographic direction. This has not previously been reported in literature and it is probably safer at this stage to explain the discrepancy in terms of the inhomogeneities detected in these highly doped specimens.

3b. Conclusion

It has already been stated in section 1a that Koch

had obtained a value of $m^* = 0.17m_o$ from optical measurements. Section 2d showed that the results of Nagasawa et al could be reinterpreted to give the same value. Marley and Dockerty (96) give no details, but state that measurements of the Seebeck coefficient on their crystals give values of m^* between $0.12\ m_o$ and $0.18\ m_o$. The present results give a most reliable value of $m^* = 0.16\ m_o$ or $0.17\ m_o$. Further experiments should be performed to determine whether the electron effective mass is anisotropic as suggested in section 3a.

3c. Forbidden Energy Gap

Summitt and Borrelli (103) have recently determined the band gap of stannic oxide from optical measurements over a wide range of temperature. Figure 4.4 shows the curves they obtain for light polorised perpendicular and parallel to the c-axis. The lower of these is considered as it would have the greatest effect on the intrinsic conductivity.

Above 200^oK the curve for the variation of E with temperature is a straight line, and so the energy gap may be written as

$$E_g = E_o + \gamma T, \qquad (4.3)$$

where E_o is the extrapolated value of the band gap at 0^oK (=3.8 eV) and γ is a constant.

Comparing equations 1.20 and 1.21 with 3.1 it can be seen that

$$\sigma = B \exp-(\frac{E_g}{2kT}) \qquad (4.4)$$

substituting for E_g from 4.3

$$\sigma = B \exp-(\frac{E_o + \gamma T}{2 k T}) = B' \exp(-\frac{E_o}{2 kT}), \qquad (4.5)$$

where $B' = (N_c N_v)^{1/2} e\mu \exp \frac{-\gamma}{2k}$.

The product $(N_c N_v)^{1/2}$ is proportional to $T^{3/2}$ and section 2a shows that the expected variation of μ for a nondegenerate crystal is as T^{-1}. Thus B is approximately proportional to $T^{1/2}$. On the slope of log σ vs T^{-1} between $500^{o}K$ and $1000^{o}K$, this would make only a small difference equivalent to 0.08 e V (or 3%) on the measured activation energy which would otherwise be equal to E_o. The measured value of E_{act} was 3.04 eV (Chapter 3 sect.2c). The third figure is not significant, so the energy gap at $0^{o}K$ (E_o) as measured is 3.0 eV. This is somewhat lower than the value of Summitt and Borrelli, although the result obtained on the chromium doped crystal (3.7 eV) is very much nearer their value. It is usual for the energy gaps in a polar semiconductor, as determined by optical and electrical methods, to be slightly different.

3d. <u>Hole Effective Mass</u>

By making various assumptions and using the results available, it is possible to obtain an estimate of the hole effective mass from equation 1.22. In an intrinsic semiconductor $n_e = n_h$ and a value of n_e is obtained using the values $\sigma = 2.10^{-3}$ (from curve 2, figure 3.2, at $1000^{o}K$) and $\mu = 50$ (from specimen 3 figure 3.9, at $1000^{o}K$) in equation 1.51. If a value of $E_o = 3.0$e V is used and also the value of γ (= $1.2.10^{-3}$ eV/^{o}K) obtained from Summitt and Borrelli, the value of the band gap (E_g) at $1000^{o}K$ is 1.8 eV. If this figure, and the value obtained for the electron effect-mass ($m_e^* = 0.16m_o$) is now substituted into equation 1.22 the hole effective mass is found to be $19m_o$. This is likely to be a lower limit. If the value of band gap at $1000^{o}K$ obtained by extrapolating Summitt and Borrelli's results is used (E_g= 2.6 eV), then $m_h^* = 55 m_o$.

Such a high effective mass would explain why p-type material of high conductivity has not been produced.

3e. Impurity Levels

The brown undoped crystals had an activation energy of 0.94 eV. The comparison of equation 3.1 and equation 1.24 shows that if the number of acceptors is small, this should correspond to the depth of the donor levels below the conduction band. If the number of acceptors is large, then $E_D = \frac{1}{2} E_{act} = 0.47$ eV (equation 1.26). It is believed that the donor levels in these crystals are created by oxygen vacancies in the lattice as they only occur in crystals that were quenched from a high temperature or cooled in the absence of oxygen. However, since the mass spectrographic analysis (Table 2.5) showed that the largest single impurity was aluminium, and being a group III element it would act as an acceptor if it replaced tin in the stannic oxide lattice, the latter case should not be ignored.

Houston and Kohnke (104) have determined several defect levels in $Sn O_2$ crystals by measuring the thermally excited photocurrent. Among these are levels at 0.52 and 1.0 eV which are both near to the possible positions of the donor level.

The brown crystals showed a faint luminescence in the yellow. The transition observed was probably the same one that gave a peak at 0.49 μ (2.5 eV) in the flame fusion whiskers (figure 3.10). This was observed at liquid nitrogen temperature where the band gap might be expected to be near 3.0 eV (see section 3c) or 3.6 eV (reference 103). So there is a possibility that this transition corresponds to one between the donor level and the valence band. It is, however, difficult to relate the defect levels proposed by Houston and Kohnke with the

transitions observed from the spectral distribution of the luminescence.

The theoretical value of the first ionised potential of a donor, based on the Bohr model of the hydrogen atom, is given as

$$E_D = \frac{2\pi^2 m^* e^4}{\epsilon^2 h^2} = \frac{13.6}{\epsilon^2} \frac{(m^*)}{(m_o)} \text{ eV} \qquad (4.6)$$

Using the values of $m^* = 0.16m_o$ and $\epsilon = 4$, then E =0.136eV. This is close to the value obtained by Miloslavskii and Lyashenko (89) for the depth of the donor levels in antimony doped films (0.15 eV).

Section 4. Thermoelectric Figure of Merit

4a. $\alpha^2\sigma$ Product

The values of $\alpha^2\sigma$ for the four crystals are directly obtainable from the values of Seebeck coefficient and electrical conductivity reported in Chapter III. The variation of $\alpha^2\sigma$ with temperature for each specimen is shown in figure 4.5a. Even at high temperatures the magnitude of this product is an order of magnitude lower than the best high temperature thermoelectric materials known today. Ge-Si alloys, which are among the best, have a value of $\alpha^2\sigma = 2.5.10^{-5}$ at 900°K.

The value of $\alpha^2\sigma$ should vary with the degree of doping. For each temperature there will be a doping level for which this product will have a maximum value.

4b. Thermal Conductivity (K)

Unfortunately no results of measurements of the thermal conductivity of stannic oxide single crystals have been published. A value for ceramic material of 57.10^{-3} cal $cm^{-2}\,°C^{-1}sec^{-1}$ (0.0136 watts $cm^{-2}\,°C^{-1}$) is reported by Marley and McAvoy (45). This is of the same order as thermoelectric materials such as bismuth telluride (105) (0.015 watts $cm^{-2}\,°C^{-1}$) and lead telluride (106)(0.025 watts $cm^{-2}\,°C^{-1}$), although it is possible that the single crystal would have a higher value.

The Handbook of Chemistry and Physics (107) also

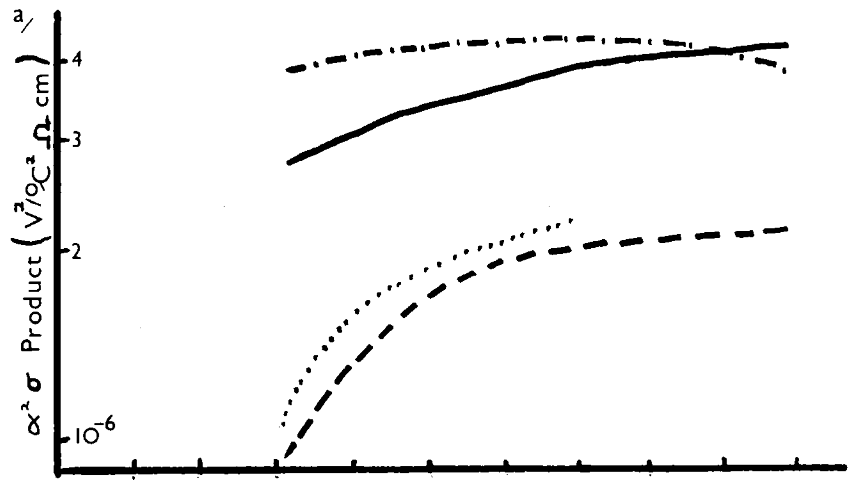

Figure 4.5:
Temperature variation of various thermo-electric parameters.

a) $\alpha^2\sigma$ product (measure)
b) κ (calculated)
c) $Z = \dfrac{\alpha^2\sigma}{\kappa}$

Key: the same as figure 3.9.

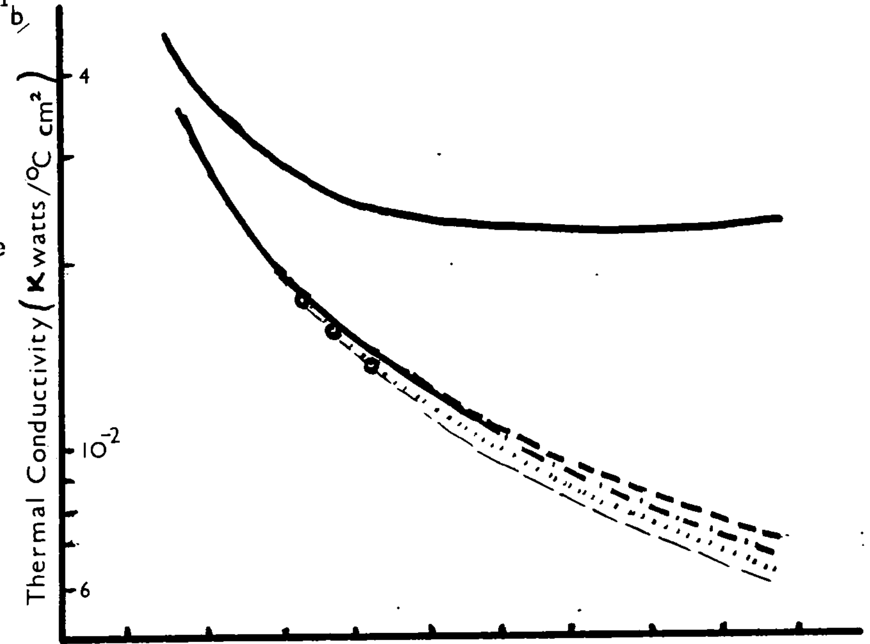

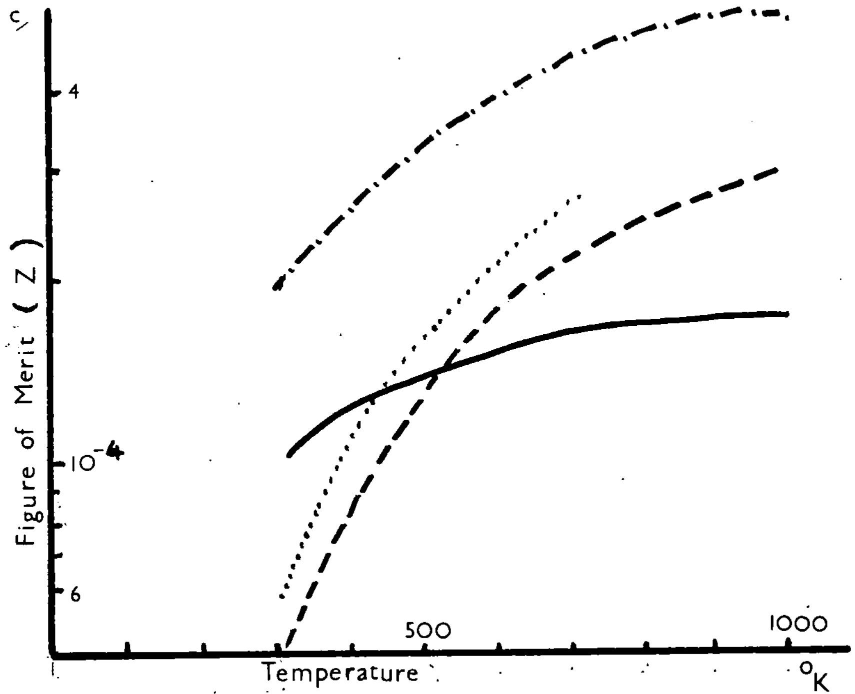

quotes results for the thermal conductivity of ceramic $Sn\ O_2$. It does so for three different temperatures. These results are shown in figure 4.5b. Since the electrical conductivity of ceramic $Sn\ O_2$ is usually very low, it was assumed that the values given were due entirely to the lattice component of thermal conductivity.

The electronic component (K_e) was calculated from equations 1.58 and 1.60. The values of K_L for other temperatures were calculated ~~for other temperatures~~ assuming that $K_L \propto T^{-1}$ (see Chapter 1, Sect. 2f). The total expected thermal conductivity at each temperature was found by adding the two components (equation 1.64). The results are shown in figure 4.5b.

4c. Figure of Merit (Z)

The estimated of the value of Z and its temperature variation was made by simply combining the results plotted in figures 4.5a and 4.56. Although this value of Z is an order of magnitude smaller than the best known thermoelectric materials, it is comparable with such materials as the III-V compounds In Sb and In As (108).

4d. Conclusion

The above results,coupled with the fact that no p-type material of high conductivity has yet been obtained,suggest that it is unlikely that stannic oxide would be a good material for any particular thermoelectric application.

Section 5. Summary and Suggestions for Further Work

Although the technology of manufacturing stable thin films of stannic oxide has been developed for many years, it is only recently that any scientific publications on the properties of the material have been made. Good single crystals of stannic oxide have now been grown by various workers (50, 56, 58 and 60) so the field is now open to quantitive study. Even so there are still many difficulties to be overcome. It is difficult to make low noise, ohmic

contacts to the crystals and these are essential for reliable Hall measurements. Although there is no information on the homogeneity of doped crystals grown by other workers, the present work shows that uniformity of doping is difficult to achieve.

It appears that scattering by longitudinal optical polar modes is the predominant mechanism in limiting the mobility of electrons at high temperatures. Unfortunately, there is as yet no polaron theory that claims to be valid at high temperatures. The characteristic temperature of the optical mode vibrations has not yet been determined with any certainty, but values of 150°K (55), 500°K (96), 196°K and 414°K (103) have been used to explain experimental results.

All methods of crystal growth require a high temperature. This results in a high defect concentration in the crystals and means that the effect of the optical mode scattering at low temperatures is masked by the impurity scattering. If crystals of low defect concentration could be produced it might be possible to confirm one of the expressions proposed for polaron mobility (24, 25, 26), and also to obtain accurate values for α_c and θ. The recent crystals of Nagasawa et al (56, 95) which show a mobility which increases with decreasing temperature down to 100°K may possibly be used for this type of measurement.

Although as a thermoelectric material stannic oxide may not be particularly interesting, further more precise work on the conduction mechanism could be profitable. It would be interesting to obtain much more information on the nature of the valence band.

Electron paramagnetic resonance studies on doped and undoped crystals could yield interesting results. An undoped crystal showed many unidentified lines when examined

at room temperature. At liquid helium temperatures it may be possible to learn something from the fine structure of such lines and to relate some of them to various types of defect.

There has been a small amount of work on the photoconductivity of stannic oxide but very little is yet known about the effect of various impurities on this phenomena. The present work has also shown that there is luminescence in stannic oxide prepared by some methods. It would be interesting to discover the types of defect responsible for the various transitions.

At present, the only commercial interest in stannic oxide is as a thin film resistor, or as a transparent conducting film; but as a material very little is known about some of its most basic properties and it could provide topics of research for many years to come.

REFERENCES

1. J. MacDougall and E. S. Stoner: Trans. Roy. Soc., A 237, 67, (1939)
2. P. Rhodes: Proc. Phys. Soc., A 204, 396, (1950)
3. W. A. Johnson and F. M. Shipley: Phys. Rev., 90, 523, (1953)
4. A. C. Beer, M. N. Chase and P. E. Choquard: Helv. Phys. Acta, 28, 529, (1955)
5. O. Madelung: Halbleiter: Handbook der Physik, 20, 1, (1957)
6. Landsberg: Proc. Phys. Soc. (London), A66, 662, (1953)
7. Guggenheim: - do. - A66, 121, (1953)
8. G.Liebfried and E. Schlomann: Nachr. Akad. Wus., Göttingen, Math-Physik, Kl 29, 71, (1954)
9. G. Borelius, W. H. Keesom and C. H. Johansson: Comme Leiden, 46a, (1928)
10. G. Borelius, W. H. Keesom, C. H. Johansson and J. O. Linde: Comme Leiden, 206a, 206b, (1930) and 217d, (1932)
11. G. Borelius: Physica, 19, 807, (1953)
12. N. Cusack and P. Kendall: Proc. Phys. Soc. (London), 72, 898, (1958)
13. J. Nyström : J.Arkiv für Fysik, 34A, 27, (1947)
14. L. Onsager: Phys. Rev., 37, 405, (1931); 38, 2265, (1931)
15. C. A. Domenicali: Rev. Mod. Phys., 26, 237, (1954).
16. W. Thomson (Lord Kelvin) Proc. Roy. Soc. (Edinburgh). Trans. 21, Pt 1, 123, (1857)
17. J. Bardeen and W. Shockley: Phys. Rev., 80, 72, (1950)
18. W. A. Harrison: Phys. Rev. 104, 1281, (1956)
19. H. Fröhlich: Proc. Roy. Soc., A160, 230, (1937)
20. D. J. Howarth and E. H. Sondheimer: Proc. Roy. Soc., A219, 53, (1953)
21. R. L. Petritz and W. W. Scanlon: Phys. Rev., 97, 1620, (1955)
22. T. D. Lee, F. E. Low and D. Pines: Phys. Rev., 90, 297, (1953)
23. F. E. Low and D. Pines: Phys. Rev., 91, 193, (1953)

24. F. E. Low and D. Pines: Phys. Rev., 98, 414, (1955)

25. R. P. Feynmann, R. W. Hellwarth, C. K. Iddings and P. M. Platzman: Phys. Rev., 127, 1004, (1962)

26. T. D. Schultz: Phys. Rev., 116, 526, (1959)

27. E. Conwell and V. F. Weisskopf: Phys. Rev., 69, 258A, (1946)

28. H. Brooks: Phys. Rev., 83, 879, (1951)

29. R. Mansfield: Proc. Phys. Soc. (London), B69, 76, (1956)

30. N. Sclar: Phys. Rev., 104, 1559, (1956)

31. D. L. Dexter and F. Seitz: Phys. Rev., 86, 964, (1952)

32. W. T. Read, Jr.: Phil. Mag., 45, 775, (1954), 46, 111, (1955)

33. E. Cartmell and G. W. A. Fowles: Valenay and Moleculor Structure, Butterworths, (1961)

34. E. Mooser and W. B. Pearson: Journal of Electronics, 1, 629, (1956)

35. C. A. Coulson: Valence, p.134., Oliver and Boyd, (1952)

36. L. Pauling: Nature of the Chemical Bond, Cornell Univ. Press, (1945)

37. H. Spandau and E. J. Kohlmeyer: Z. Anorg. Chem. 254, [illegible]5, (1947)

38. H. Spandau and Ullrich: Z. Anorg. 274, 271, (1953)

39. J. D. Donaldson and W. Moser: J. Chem. Soc., 835, (1961)

40. J. D. Donaldson and W. Moser and W. B. Simpson: J. Chem. Soc., 839, (1961)

41. J. P. Coughlin: Heats and Free Energies of Formation of Inorganic Oxides, U.S. Bureau of Mines, Bulletin 542, (1954)

42. L. Brewer: Chem. Rev., 52, 1, (1953)

43. B. P. Kryzhanovskii and A. Ya. Kuznetson: Russ. J. Phys. Chem. 35, 38, (1961)

44. J. C. Platteeuw and G. Meyer: Trans. Faraday Soc., 52, 1066, (1956)

45. J. A. Marley and T. C. MacAvoy: U.S.A.F. Report AFCRL - -62-771, (Sep. 1962)

46. Handbook of Chemistry and Physics, 41st. ed. p.975, (1959-60)

47. J. F. Goodman and S. J. Gregg: J. Chem. Soc. 1162, (1960)

48. J. W. Nielsen and E. K. Dearborn: J.Phys.Chem.Solids, 5, 202,(1958)

49. J. P. Remeika: J.Am.Chem.Soc., 76, 940, (1954)

50. H. F. Kunkle and E. E. Kohnke: J. App.Phys., 36, 1489, (1965)

51. L. P. Kus'mina and B. N. Litvin: Sov.Phys.- Crystallography 8, 379, (1965)

52. L. Clark and J. Woods: Brit. J.App.Phys., 17, 319, (1966)

53. G. Mandel: Phys. Chem. Solids, 23, 1177, (1962)

54. K. Ishiguro, T. Sasaki, T. Arai and I. Imai: J. Phys. Soc.Japan, 13, 246, (1958)

55. H. Koch: Physica Status Solidi, 3, 1619, (1963)

56. M. Nagasawa, S. Shionoya and S. Makishima: Jap. J.App. Phys. 4, 195, (1965)

57. D. A. Curtis: Ph.D. Thesis. University of Durham. (1964)

58. J. A. Marley and T. C. MacAvoy: J. App. Phys, 32, 2504, (1961)

59. F. P. Koffyberg: J. App. Phys., 36, 844, (1965)

60. T. B. Reed, J. T. Roddy and A. N. Mariano: J. App.Phys., 33, 1014, (1962)

61. S. F. Reddaway and D. A. Wright: Brit. J. App. Phys., 16, 195, (1965)

62. V. K. Miloslavskii: Optics and Spectroscopy, 7, 154, (1959)

63. L. Vegard: Pil. Mag. Series 6, 32, 65, (1916)

64. M. G. Andresen: Phys. Rev., 120, 1606, (1960)

65. Dana: System of Mineralogy, 7th Ed., p.574, (1944)

66. Bourgeois: Ball. Soc. Min., 11, 58, (1888) mentioned in ref. 65.

67. W. H. Baur: Acta. Cryst., 9, 515, (1956)

68. W. Parrish and B. W. Irwin: Data for X-ray Analysis Vol.1. Philips, Eindhoven, (1963)

69. J. B. Nelson and D. P. Riley: Proc. Phys.Soc.(London),57,160,(1945)

70. H. P. Klug and L. E. Alexander: X-ray Diffraction Procedures, J.Wiley & Sons, p.441, (1954)

71. H. E. Swanson and E. Tatge: NBS Circular 539, 1, 54, (1954)

72. H. Schröke: Neus Jahrb. Mm.,Monatsch 1959, p.57.

73. V. T. Sihvonen and D. R. Boyd: J.App. Phys. 29, 1143, (1958)

74. J. M. Honig, A. A. Cella, T. B. Reed: Solid State Research, Lincoln Lab. Quarterly Report 1961, No. 4, p.17.

75. E. E. Kohnke: J. Phys. Chem. Solids, 23, 1557, (1952)

76. A. E. Middleton and W. W. Scanlon: Phys. Rev., 92, 219, (1953)

77. Reference Tables for Thermocouples: NBS Circular 561, U.S. Dept. of Commerce (1955)

78. T. Arai: J. Phys. Soc. Japan, 15, 5, (1960)

79. R. G. Breckenridge and W. R. Hosler: Phys. Rev., 91, 793, (1953)

80. J. E. Houston and E. E. Kohnke: J. App. Phys., 36, 3931. (1965)

81. R. H. Bube and S. M. Thomsen: J. Chem. Phys., 23, 15, (1958)

82. W. H. From: Phys. Rev., 131, 961, (1963)

83. G. Bauer: Ann. d. Phys., 30, 433, (1937)

84. R. E. Aitcheson: Australian J. Appl. Sci., 5, 10, (1954)

85. R. H. W. Burkett: J. British I.R.E., 21, 4, 301, (1961)

86. L. Holland: Vacuum Deposition of Thin Films, p.493 f. J. Wiley & Sons Ltd.

87. J. M. Mochel: U.S. Patent 2, 522, 531.

88. I. Imai: J. Phys. Soc. Japan. 15, 937, (1960)

89. V. K. Miloslavskii and S. P. Lyashenko: Optics and Spectroscopy 8, 455, (1959)

90. S. P. Lyashenko and V. K. Miloslavskii: Sov.Phys. - Solid State 6, 2042, (1965)

91. H. Koch: Physica Status Solidi, 3, 1059, (1963)

92. H. Koch: Physica Status Solidi, 7, 263, (1965)

93. D. F. Lewis and E. H. Sondheimer: Proc. Roy.Soc., A277, 241,(1959)

94. L. D. Loch: J.Electro Chem.Soc.,110, 1081, (1963)

95. M. Nagasawa, S. Shionoya and S. Makishima: J.Phys. Soc.Japan, 20, 1093, (1965)

96. J. A. Marley and R. C. Dockerty: Phys.Rev.,140, A304, (1965)

97. F. Van der Maesen and C. H. M. Witmer: Physics of Semiconductor, Proc. 7th Int. Conf.Paris, p.1211,(1964)

98. H. J. Van Daal and M. Enz: to be published. Mentioned in ref.97

99. A. F. Ioffe: Semiconductor Thermoelements and Thermoelectric Cooling. Infosearch, London, 1457,p.29

100. S. F. Reddaway: Private communication.

101. S. F. Reddaway and D. A. Wright: Brit. J.App.Phys., 16, 145,(1965)

102. Th.Liebisch and R. Rubens: Sitz-Ber.D.A.dW., 2, 876, (1919)

103. R. Summitt and N. F. Borrelli: J. Appl. Phys., 37, 2200, (1966)

104. J. E. Houston and E. E. Kohnke: J. App. Phys., 36, 3931, (1965)

105. C. B. Satterthwaite and R. W. Ure Jr., Phys. Rev., 108, 1164, (1947)

106. W. Scanlon: Solid State Physics, Vol. 9. Academic Press, N.Y.

107. Handbook of Chemistry and Physics, 41st ed., p.2443,(1959-60)

108. R. Bowers, J. Bauerle and A. Cornish: J. App. Phys., 30, 1050, (1959)

APPENDIX

Paper accepted by the British Journal of Applied Physics published March, 1966.

Reprinted from

British Journal of Applied Physics

The Institute of Physics and The Physical Society

Printed in Great Britain by Adlard & Son, Ltd., Dorking

BRIT. J. APPL. PHYS., 1966, VOL. 17

Electrical properties of single crystals of antimony-doped stannic oxide

D. F. MORGAN and D. A. WRIGHT

Department of Applied Physics, University of Durham

MS. received 1*st November* 1965

Abstract. Single crystals of stannic oxide heavily doped with antimony have been grown from tin vapour and oxygen at 1450°C. Their electrical properties have been studied between 77 and 1100°K. These can be interpreted in terms of optical mode lattice scattering at the higher temperatures, with an impurity scattering contribution below about 300°K. Combining the Hall and Seebeck coefficients leads to an average electron effective mass of 0·13 m_0.

1. Introduction

Stannic oxide is a semiconducting oxide with an energy gap of 3·4 ev (Arai 1960, Kohnke 1962), and is chemically stable up to 1100°C (*Handbook of Chemistry and Physics* 1952). These properties indicated that the material might be useful for thermoelectric applications at high temperatures.

Stannic oxide conducting films have been produced commercially for many years, and it is well known that the electrical conductivity can be controlled by adding antimony as a donor impurity. The conductivity of these doped films is stable up to 800°C (Arai 1960), whereas films without added impurity undergo irreversible changes above 100°C (Imai 1960, Koch 1963a). Koch (1963a) has summarized previous work on thin films of stannic oxide and has concluded that the predominant scattering is by polar longitudinal optical modes, and that the characteristic temperature of the phonons is around 150°K. In a later paper on optical measurements, Koch (1963b) proposes a probable electron effective mass of 0·3 m_0. More recently, Summitt and Borelli (1965) obtained a value of 0·14 m_0 from measurements of the Faraday rotation. Attention should also be drawn to the work of Lyashenko and Miloslavskii (1965) who conclude, from measurements of the optical constants in the infra-red, that the effective mass varies with carrier concentration.

Until recently, electrical measurements on single crystals have been confined to natural crystals (Kohnke 1962), but Nagasawa *et al.* (1965a, b) have measured the conductivity and Hall effect of undoped crystals of high resistivity grown by the controlled reaction of $SnCl_4$ with H_2O at 1300°C.

The purpose of the present work was to grow single crystals of stannic oxide, doped with various concentrations of antimony, and to measure the electrical conductivity, Hall effect and Seebeck effect over a wide range of temperatures to obtain information about the effective mass, scattering and thermoelectric figure of merit of the material.

2. Crystal growth

The crystals were prepared by a high-temperature vapour phase method. The furnace arrangement is shown in figure 1. The starting material was 5N pure tin. The gas supplies were regulated to give a constant flow in the range 100–150 cm^3 min^{-1} for the argon and 20–40 cm^3 min^{-1} for the oxygen. The crystals grew on the mullite oxygen tube in the region of the aperture and on the walls of the outer mullite tube. The most perfect crystals, however, grew on the alumina boat, containing the tin metal, from the small amount of oxygen that diffused back. These crystals grew in about 10–15 days. The amount of antimony introduced into the crystals was controlled by varying the position, and thus the temperature, of the alumina boat containing metallic antimony. By this method crystals up to 1·5 mm × 1·5 mm × 10 mm were grown at a temperature of 1450°C. The chief crystal habits were diamond-shaped twinned plates and rectangular rods. Most

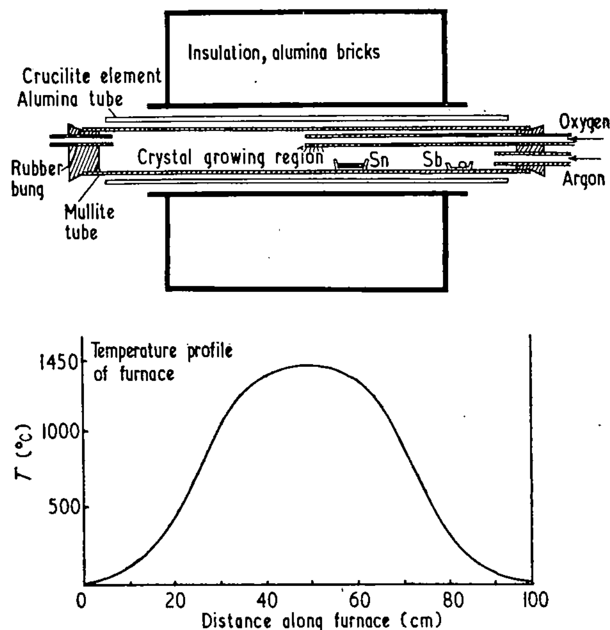

Figure 1. Furnace arrangement for growing stannic oxide crystals.

of the rods grew parallel to the c axis with end and side faces of the form (101) and (110). Some rods, however, grew with the c axis perpendicular to their longest side. These were hexagonal in cross section with faces of the form (011), (010) and (110). The rods which grew parallel to the c axis were used for the electrical measurements.

Attempts to grow p-type material by introducing indium or gallium into the crystal have not been successful. A crude determination of the sign of the Seebeck coefficient has shown that these crystals are p-type, but their resistivity has been very high and well-formed crystals have not been produced.

3. Experimental procedure and results

The electrical conductivity was measured by a four-probe method using a silica specimen holder described by Marley and McAvoy (1963, U.S. Air Force Rep. No. AFCRL–67–771). The current contacts were of platinum paste and the voltage probes were pressure contacts of fine platinum wire held in place by fine silica capillary tubing. An Ohm's law plot was made at temperatures between 77 and 1300°K in air. There was no change in the resistivity of samples kept at 1300°K for several days.

Hall effect measurements were made on the samples at room temperature and liquid nitrogen temperature, using indium contacts. The carrier density of each sample was found to be about the same at each temperature (see table 1). No satisfactory contact has been found for these measurements at very high temperatures, but measurements have been made up to 600°K using contacts of molten indium. These results show that the carrier density remains constant up to this temperature.

It is clear from the magnitude of the Seebeck effect that both samples are at least partially

Table 1. Electrical properties of doped SnO_2

	Specimen 1		Specimen 2	
Temperature (°K)	77	293	77	293
R(cm^3 C^{-1})	$7{\cdot}2.10^{-2}$	$7{\cdot}1.10^{-2}$	0·79	0·80
n (carriers/cm^3)	$8{\cdot}7.10^{19}$	$8{\cdot}8.10^{19}$	$8{\cdot}0.10^{18}$	$8{\cdot}2.10^{18}$
$\sigma(\Omega^{-1}$ cm$^{-1})$	$1{\cdot}33.10^3$	$1{\cdot}22.10^3$	79	87
μ(cm^{2}v^{-1} sec^{-1})	96	87	62	70

degenerate, so in calculating the carrier density n, the factor r in the relationship

$$R = r/ne \tag{1}$$

is taken as unity. Using the relationship

$$\sigma = ne\mu \tag{2}$$

where n in this case is constant, $\log \mu$ was plotted against $\log T$ (see figure 2). The curves approximate closely to $\mu \propto T^{-1/2}$ at the higher temperatures, confirming that the scattering is by optical modes.

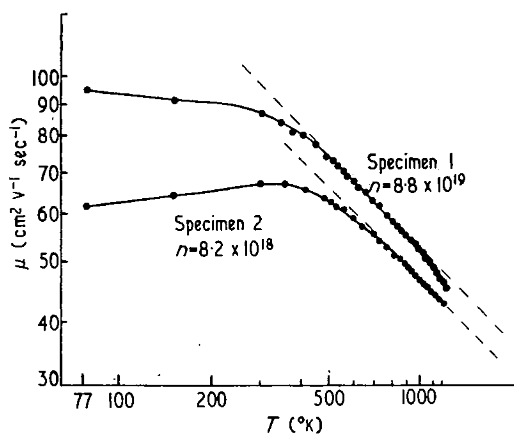

Figure 2. Plot of mobility against temperature. The broken lines represent $\mu \propto T^{-1/2}$.

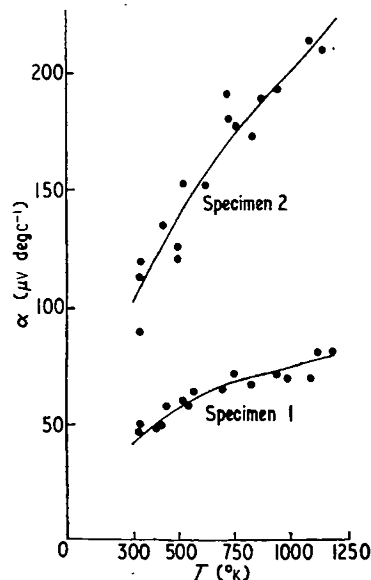

Figure 3. Plot of Seebeck coefficient against temperature.

The Seebeck coefficient of the same specimens was measured in an apparatus based on the design of Middleton and Scanlon (1953) made of silica, using carbon blocks as the heat source and heat sink. In a nitrogen atmosphere this apparatus was used up to 1000°c. The Seebeck voltage was measured with respect to the platinum components of Pt–Pt/13 %Rh thermocouples. A plot of V_S (Seebeck voltage) against ΔT (temperature difference) was made at each temperature. The results are shown in figure 3.

4. Discussion and conclusions

The expression for the Seebeck coefficient α is

$$\alpha = \pm \frac{k}{e}\left\{\frac{(s+\frac{5}{2})\,F_{s+3/2}(\eta)}{(s+\frac{3}{2})\,F_{s+1/2}(\eta)} - \eta\right\}. \tag{3}$$

Since both the present work and that of Koch (1963a, b) indicate optical mode scattering, the value $s = \frac{1}{2}$ should be applicable at the higher temperatures.

The carrier density is given by

$$n = (4\pi/h^3)\,(2m^*kT)^{3/2}\,F_{1/2}(\eta) \tag{4}$$

where η is the reduced Fermi level (E_F/kT), e the electronic charge, m^* the effective mass of the electrons and h is Planck's constant.

At the lower temperatures, at least part of the scattering will be due to impurities. Ionized impurity scattering would mean that $s = \frac{3}{2}$ should be used in equation (3). Using the ($\log \mu$, $\log T$) plot, the values of $\mu \propto T^{-1/2}$ at high temperatures were extrapolated back to the low-temperature region. Assuming that this extrapolation gave values of the component of mobility μ_{opt} due to optical mode scattering, the component μ_i due to

impurities was then derived from

$$\mu_m^{-1} = \mu_I^{-1} + \mu_{opt}^{-1} \quad (5)$$

where μ_m is the measured value as in figure 2. It was found that, at low temperatures, μ_I was approximately proportional to $T^{3/2}$ for both samples, confirming that there is a contribution from ionized impurity scattering.

It should be noted also that the contribution due to impurity scattering is greater in specimen 2 than in specimen 1, in spite of the lower carrier concentration. This, presumably, is due to different concentrations of acceptors, leading to different degrees of compensation. Acceptors may arise from the departure from stoichiometry of the crystal; it is known, however, that these crystals contain appreciable but varying amounts of silicon, iron, aluminium, sodium and potassium.

For specimen 2 ($n \sim 8{\cdot}2 \times 10^{18}$ carriers/cm^3) the (incorrect) assumption of optical mode scattering ($s = \frac{1}{2}$) throughout the temperature range leads to a value of $m^* = 0{\cdot}11\ m_0$ at 300°K, falling to $0{\cdot}10\ m_0$ at 1300°K. Assuming wholly ionized impurity scattering at 300°K ($s = \frac{3}{2}$), $m^* = 0{\cdot}07\ m_0$ is obtained. Since μ_m is 75% of μ_{opt} at 300°K, m^* must be nearly equal to $0{\cdot}10\ m_0$ from 300 to 1300°K.

Correspondingly, for specimen 1 ($n \sim 8{\cdot}8 \times 10^{19}$ carriers/cm^3) optical mode scattering throughout the range would indicate $m^* = 0{\cdot}20\ m_0$ at 300°K, falling to $0{\cdot}10\ m_0$ at 1100°K. With $s = \frac{3}{2}$ at 300°K, $m^* = 0{\cdot}12 m_0$. Here μ_m is 91% of μ_{opt}; m^* is therefore clearly greater than $0{\cdot}12\ m_0$ at 300°K and probably near $0{\cdot}17\ m_0$.

The value of m^* at 100°K for specimen 1 was found to be $0{\cdot}19\ m_0$ assuming $s = \frac{1}{2}$ and $0{\cdot}14\ m_0$ assuming $s = \frac{3}{2}$. Here μ_m is 50% of μ_{opt} and again m^* must therefore be near $0{\cdot}17\ m_0$. There is thus an indication that m^* decreases above room temperature in this sample. It should, however, be noticed that due to the nature of expression (3), for low values of α, small variations in α lead to large variations in the value of η, and hence m^*, obtained. It also appears that at the lower temperatures m^* is higher in this sample than in sample 2. The accuracy is however hardly adequate for firm conclusions to be drawn. The estimated values of m^*/m_0 are shown in table 2 and their mean is 0·13.

Table 2. Thermoelectric properties and effective mass

Temperature (°K)	100		300		1100	
Specimen	1	2	1	2	1	2
α (μV degC^{-1})	13		42	104	72	214
$\alpha^2\sigma$			$2{\cdot}1.10^{-6}$	$9{\cdot}5.10^{-7}$	$3{\cdot}6.10^{-6}$	$2{\cdot}7.10^{-6}$
m^*/m_0	0·17		0·17	0·11	0·10	0·10

As regards thermoelectric applications, the values of $\alpha^2\sigma$ at 300 and 1100°K are shown in table 2, and are not very promising. There are no really good materials for thermoelectric generation at high temperatures; Ge–Si alloys are among the best and have values of $\alpha^2\sigma$ of the order of $2{\cdot}5 \times 10^{-5}$ at 900°K, considerably larger than those in table 2. So far the thermal conductivity has not been measured for SnO_2 in this laboratory, nor have highly conducting samples of p-type material been prepared.

References

Arai, T., 1960, *J. Phys. Soc. Japan*, **15**, 916–26.

Handbook of Chemistry and Physics, 1952, 34th edn (Cleveland, Ohio: Cleveland Rubber Publishing Co.), p. 597.

Imai, I., 1960, *J. Phys. Soc. Japan*, **15**, 937–8.

Koch, H., 1963a, *Phys. Stat. Sol.*, **3**, 1059–71.

—— 1963b, *Phys. Stat. Sol.*, **3**, 1619–28.

Kohnke, E. E., 1962, *J. Phys. Chem. Solids*, **23**, 1557–62.

Lyashenko, S. P., and Miloslavskii, V. K., 1965, *Soviet Physics–Solid State*, **6**, 2042–3.

Middleton, A. E., and Scanlon, W. W., 1953, *Phys. Rev.*, **92**, 219–26.

Nagasawa, M., Shionoya, S., and Makishima, S., 1965a, *J. Phys. Soc. Japan*, **20**, 1093.

—— 1965b, *Jap. J. Appl. Phys.*, **4**, 195–202.

Summitt, R., and Borrelli, N. F., 1965, *J. Phys. Chem. Solids*, **26**, 921–5.